



Late Ediacaran juvenile magmatism in the Variscan Monts-du-Lyonnais metamorphic complex (Massif Central, France)

Simon Couzinié, Oscar Laurent, Pierre Bouilhol, Cyril Chelle-Michou,
Anne-Céline Ganzhorn, Véronique Gardien, Jean-François Moyen

► To cite this version:

Simon Couzinié, Oscar Laurent, Pierre Bouilhol, Cyril Chelle-Michou, Anne-Céline Ganzhorn, et al.. Late Ediacaran juvenile magmatism in the Variscan Monts-du-Lyonnais metamorphic complex (Massif Central, France). *Bulletin de la Société Géologique de France*, In press, 10.1051/bsgf/2024023 . hal-04822267

HAL Id: hal-04822267

<https://uca.hal.science/hal-04822267v1>

Submitted on 6 Dec 2024

HAL is a multi-disciplinary open access archive for the deposit and dissemination of scientific research documents, whether they are published or not. The documents may come from teaching and research institutions in France or abroad, or from public or private research centers.

L'archive ouverte pluridisciplinaire **HAL**, est destinée au dépôt et à la diffusion de documents scientifiques de niveau recherche, publiés ou non, émanant des établissements d'enseignement et de recherche français ou étrangers, des laboratoires publics ou privés.



Distributed under a Creative Commons Attribution 4.0 International License

Late Ediacaran juvenile magmatism in the Variscan Monts-du-Lyonnais

metamorphic complex (Massif Central, France)

Identification d'un magmatisme juvénile fini-édiacarien dans le complexe

métamorphique varisque des Monts-du-Lyonnais (Massif Central, France)

5 Simon Couzinié^{1,2,3*}, Oscar Laurent⁴, Pierre Bouilhol¹, Cyril Chelle-Michou⁵, Anne-

6 Céline Ganzhorn^{3**}, Véronique Gardien³, Jean-François Moyen⁶

⁷ ¹Université de Lorraine, CNRS, CRPG, 54000 Nancy, France

⁸ ²Université Jean Monnet, CNRS, LGL-TPE UMR5276, F-42023 Saint-Etienne, France

⁹ ³LGL-TPE UMR 5276, CNRS, Université Lyon 1, ENS de Lyon, 69622 Villeurbanne, France

10 ⁴CNRS, Géosciences Environnement Toulouse, Observatoire Midi-Pyrénées, 14 avenue Edouard
11 Belin, 31400 Toulouse, France

12 ⁵Institute of Geochemistry and Petrology, ETH Zürich, CH-8092 Zürich, Switzerland

⁶Université Jean-Monnet, Laboratoire Magmas et Volcans, UCA-CNRS-IRD, Aubière, France

14 *Corresponding author. simon.couzinie@univ-lorraine.fr

15 **Present address: Saint-Gobain Recherche, Aubervilliers, France

16

17

18

19

20 Keywords: Northern Gondwana margin, Cadomian orogeny, Variscan orogeny,

21 French Massif Central, zircon U–Pb–Hf isotopes

22 Mots clés: marge nord-gondwanienne, orogenèse cadomienne, orogenèse varisque,

23 Massif Central français, isotopie U-Pb-Hf sur zircon

24 **Abstract**

25 The identification of oceanic sutures is key to understanding the evolution of the
26 Paleozoic Variscan belt and the structure of the West European lithosphere. In the
27 French Massif Central, the suture of the 'Mid-Variscan' ocean would be stamped by
28 distinctive lithological formations known as 'Leptynite–Amphibolite Complexes' (LACs).
29 These formations comprise various Cambrian–Ordovician (meta-)igneous
30 associations, commonly interpreted as representing rifted-margin magmatism, and
31 experienced Devonian (385–360 Ma) high-pressure metamorphism. Our study
32 provides geochronological and geochemical data on mafic–felsic rocks from the
33 Riverie LAC in the Monts-du-Lyonnais metamorphic complex. In the Riverie LAC,
34 metaluminous, amphibole-bearing felsic gneisses represent former tonalites closely
35 associated with mafic rocks (now amphibolites). LA–ICP–MS zircon U–Pb dating
36 reveals a latest Ediacaran (c. 545 Ma) crystallization age for the melt that yielded the
37 tonalites. Whole-rock geochemistry (notably pronounced Nb negative anomalies) and
38 the highly radiogenic zircon Hf isotope compositions, with $\epsilon\text{Hf}_{(545\text{Ma})}$ of c. +11 (within
39 the range expected for the Depleted Mantle reservoir), indicate that the parental melt
40 of the tonalites ultimately originated from a mantle source metasomatized by oceanic
41 slab-derived fluids. The (meta-)mafic rocks share a similar 'arc' signature and were
42 possibly generated from the same mantle source. The mafic–felsic association of the
43 Riverie LAC is unrelated to the opening and closure of the Mid-Variscan ocean and
44 does not represent its suture. Instead, it can be correlated to a juvenile Ediacaran
45 magmatic event identified throughout the Variscan realm, interpreted as reflecting
46 Cadomian arc/back-arc magmatism.

47

48

49 **Résumé**

50 Localiser les sutures océaniques est essentiel pour comprendre l'évolution de la
51 chaîne varisque et la structure de la lithosphère de l'Europe occidentale. Dans le
52 Massif Central français, la suture d'un océan "Médio-varisque" serait marquée par des
53 formations particulières connues sous le nom de "complexes leptyno-amphiboliques"
54 (CLA). Ceux-ci incluent une diversité de roches méta-ignées datées du Cambrien-
55 Ordovicien et interprétées comme les témoins d'un magmatisme associé au rifting. Ils
56 préservent également des reliques d'un métamorphisme de haute pression au
57 Dévonien (385–360 Ma). Notre étude fournit de nouvelles données géochronologiques
58 et géochimiques sur les roches mafiques et felsiques de la « bande de Riverie », un
59 des trois complexes leptyno-amphiboliques des Monts-du-Lyonnais. Les roches
60 felsiques sont des gneiss amphiboliques métalumineux qui correspondent à
61 d'anciennes tonalites intimement associées à des roches mafiques (représentées
62 aujourd'hui par des amphibolites). La datation U–Pb par LA–ICP–MS de grains de
63 zircon magmatique a révélé un âge de cristallisation tardi-édiacarien (autour de 545
64 Ma) pour les (meta)tonalites. La géochimie des roches totales (notamment les
65 anomalies négatives en Nb) et les compositions isotopiques en hafnium très
66 radiogéniques mesurées sur les grains de zircon (avec des $\epsilon_{\text{Hf}}(545\text{Ma})$ d'environ +11)
67 indiquent que les magmas parents des tonalites se sont formés par différentiation d'un
68 liquide issu de la fusion d'un manteau métasomatisé par des fluides dérivés d'une
69 lithosphère océanique. Les amphibolites spatialement associées aux (méta)tonalites
70 présentent elles-aussi une signature de type "arc" et leurs protolithes ont pu être
71 générées à partir de la même source mantellique. L'association bimodale de la
72 « bande de Riverie » n'est pas liée au rifting ayant conduit à l'ouverture de l'océan
73 Médio-varisque et ne peut représenter sa suture. Elle doit être corrélée à un

74 événement magmatique juvénile identifié dans tout le domaine varisque et relié à la
75 dynamique d'arc/arrière-arc de l'orogenèse cadomienne.

76

77 **1. Introduction**

78 Within the framework of plate tectonics theory, sutures, i.e. zones along which oceanic
79 lithospheres were subducted, are key to deciphering the evolution of orogens (Dewey,
80 1987). Their identification remains challenging in the case of old and deeply eroded
81 collisional orogenic systems such as the European Variscan belt, formed through the
82 convergence of Laurussia and Gondwana during the late Paleozoic (Edel et al., 2018;
83 Matte, 1986; Stampfli et al., 2013). Indeed, the diagnostic suture rock associations
84 (high-pressure metamorphic belts and ophiolite sequences) have been largely
85 dismantled by early erosion and intensely reworked by collisional processes, leading
86 to conflicting views on the number of suture zones and their associated oceans (see
87 discussions in Franke et al., 2017; Kroner and Romer, 2013)). Paleomagnetic data and
88 paleobiogeography (Domeier, 2016; Paris and Robardet, 1990; Van der Voo et al.,
89 1980) suggest that the formation of the Variscan belt followed the closure of a single
90 >1000 km-wide Ordovician oceanic domain called the Rheic Ocean. On the other
91 hand, petrological evidence coupled with geophysical data collectively indicate the
92 existence of at least three sutures (Fig. 1a, Schulmann et al., 2022). The subduction
93 of an Ordovician-early Devonian “Mid-Variscan” ocean (Galicia/Southern
94 Brittany/Tepla ocean of Matte, 1986) would have initiated in the mid- to late-Devonian
95 period (390–360 Ma). The narrower Saxothuringian ocean would have closed shortly
96 after in the early Carboniferous (360–340 Ma). Lastly, subduction of the Devonian
97 Lizard–Rhenohercynian Ocean would have occurred at 340–330 Ma (Zeh and Gerdes,
98 2010).

99 Delineating the suture zones along the belt is of marked importance to unravel the
100 architecture of the European continental crust and the evolution of the Variscan
101 orogeny. However, accurately correlating their locations and geometries in the eastern
102 French Massif Central (eFMC, Fig. 1a) has proven challenging due to a lack of
103 comprehensive seismic survey and the absence of ophiolite sequences (Schulmann
104 et al., 2022). In the eFMC, it is commonly inferred (Lardeaux et al., 2014; Matte, 1986;
105 Pin, 1990; Vanderhaeghe et al., 2020) that the Mid-Variscan suture is stamped by
106 distinctive heterogeneous lithological formations referred to as “Leptynite–Amphibolite
107 Complexes” (LACs, see review in Santallier et al., 1988). The latter encompass mafic
108 meta-igneous rocks occurring as metric to kilometric boudins embedded in
109 paragneisses and/or are intimately associated with metarhyolites/metagranites of
110 crustal derivation (Briand et al., 1995, 1991; Chelle-Michou et al., 2017; Pin and Marini,
111 1993). The metabasites often bear relics of Devonian (385–360 Ma) high-pressure
112 metamorphism defining a P–T gradient consistent with subduction (Lardeaux, 2023).
113 Ultramafic bodies representing subducted mantle material are also present (Gardien
114 et al., 1990). Early geochronological studies suggested that both mafic and felsic
115 igneous protoliths were emplaced contemporaneously during the Cambrian–
116 Ordovician period (Pin and Lancelot, 1982). This has led many authors to interpret the
117 wide variety of geochemical signatures displayed by mafic rocks, ranging from MORB-
118 type tholeiites to back-arc basalts and OIB (Briand et al., 1995, 1991; Downes et al.,
119 1989; Giraud et al., 1984; Piboule and Briand, 1985; Pin and Marini, 1993) as reflecting
120 an emplacement in an attenuated continental lithosphere at the incipient stages of
121 oceanization (Lardeaux et al., 2014 and references therein). In this context, the LACs
122 were proposed to represent fragments of the passive margin to ocean–continent
123 transition zone of the Mid-Variscan ocean, which were subsequently buried through

124 oceanic subduction and later exhumed as tectonic mélanges along major thrust zones
125 in the orogenic wedge (Burg and Matte, 1978; Lardeaux et al., 2014, 2001), or possibly
126 extruded through the upper plate (de Hoÿm de Marien et al., 2023; Keppie et al., 2010;
127 Maierová et al., 2021).

128 Following the recognition of the main nappe architecture in the eFMC during the mid-
129 1980s, the various LACs were grouped into a single litho-tectonic unit referred to as
130 “the LAC” (singular) and were assumed to share the same geodynamic significance
131 (Bouchez and Jover, 1986; Lardeaux et al., 2014; Matte, 1986; Vanderhaeghe et al.,
132 2020). This broad correlation was questioned by Santallier et al. (1988), who pointed
133 out the lack of age data on the protoliths and the uncertainty on the respective
134 petrogenesis of individual LACs. This concern is echoed in the adjacent Maures
135 Massif, where three LACs were initially identified, yet only two are currently regarded
136 as delineating a suture zone (Bellot et al., 2010; Briand et al., 2002; Jouffray et al.,
137 2023; Schneider et al., 2014). Therefore, a reexamination of individual (ultra)mafic–
138 felsic rock associations across the eFMC appears necessary to ascertain whether
139 each LAC record the same geodynamic events and collectively represent a single litho-
140 tectonic unit. In this context, the increasing versatility of *in-situ* laser ablation–
141 inductively coupled plasma–mass spectrometry (LA–ICP–MS) zircon U–Pb dating
142 offers new opportunities to unravel the protolith ages of the LAC rocks and clarify their
143 origin (Chelle-Michou et al., 2017; de Hoÿm de Marien et al., 2023; Lotout et al., 2020;
144 Paquette et al., 2017).

145 This contribution focuses on the Riverie LAC from the Monts-du-Lyonnais
146 metamorphic complex in the eFMC. Novel petrological and geochronological data
147 demonstrate that this mafic–felsic association consists of juvenile arc/back-arc-derived
148 magmatic rocks of late Ediacaran age which are unrelated to the opening and closure

149 of the Mid-Variscan ocean. These findings highlight the necessity for a reevaluation of
150 the tectonic history of individual LACs within the eFMC.

151

152 **2. Geological setting**

153 **2.1 The eastern French Massif Central**

154 The eFMC is part of the internal zone of the Variscan belt (Fig. 1), primarily composed
155 of metamorphic nappes intruded by various Carboniferous granitoids (see review in
156 Faure et al., 2009). In the northern part of the eFMC, metamorphic rocks are overlain
157 by Visean sediments and volcanics indicating that the main orogenic phase occurred
158 before 345 Ma. In contrast, compression persisted till the Namurian (corresponding to
159 the Serpukhovian and Bashkirian pro parte, c. 325 Ma) in the foreland basin to the
160 south. Upper Carboniferous (Stephanian, i.e. Kasimovian–Gzhelian pro parte) to
161 Permian sediments were unconformably deposited over the metamorphic-plutonic
162 basement in a late to post-orogenic setting. The nappe pile consists of the high-grade
163 “Upper Gneiss Unit” overlying a crustal package of parautochthonous terrains,
164 sometimes divided into the Lower Gneiss Unit and the (lower-grade) Parautochthonous
165 Unit (Ledru et al., 1989). Southwards-directed thrusting of the Upper Gneiss Unit was
166 coeval to the development of an inverted Barrovian metamorphic sequence (Burg et
167 al., 1984) at 360–345 Ma (Chelle-Michou et al., 2017; Costa, 1989). The LACs are
168 commonly located at the base of the Upper Gneiss Unit and mark the contact between
169 this unit and the underlying parautochthonous terrains. Within most LACs, mafic meta-
170 igneous rocks preserve a record of high-pressure subduction-related metamorphism
171 with pressures exceeding 15 kbar at 385–360 Ma (de Hoÿm de Marien et al., 2023;
172 Joanny et al., 1991; Lardeaux et al., 2001; Lotout et al., 2020, 2018). The

173 parautochthonous terrains were locally affected by a low-pressure high-temperature
174 Buchan-type metamorphic event coeval with crust extension and the formation of the
175 Velay and Montagne Noire gneiss domes (Gardien et al., 2022, 1997; Ledru et al.,
176 2001). The latter hosts mafic eclogites whose origin is disputed: they could either
177 correspond to Upper Gneiss Unit material (and thus be subduction-related, Pitra et al.,
178 2022) or lower crustal rocks exhumed during doming (Whitney et al., 2020). Lastly, the
179 Brévenne unit is a bimodal volcanic sequence of late Devonian age metamorphosed
180 under greenschist- to lower amphibolite-facies conditions and juxtaposed to the Upper
181 Gneiss Unit during the main collisional phase (Feybesse et al., 1995).

182 The protoliths of the Upper Gneiss Unit and parautochthonous terrains consist of
183 Ediacaran to Ordovician detrital (volcano-)sedimentary units, intruded by several
184 generations of plutonic rocks (Couzinié et al., 2022, 2019). No rock older than
185 Neoproterozoic has been described so far. Pre-Variscan magmatic rocks include: (i)
186 latest Ediacaran (c. 545 Ma) and Cambro-Ordovician granites and rhyodacites of
187 crustal origin, found throughout the nappe pile regardless the metamorphic grade
188 (Chelle-Michou et al., 2017; Couzinié et al., 2022, 2017; Couzinié and Laurent, 2021);
189 (ii) mafic (gabbroic and basaltic) rocks, mainly in the LACs of the Upper Gneiss Unit
190 but also in the parautochthonous terrains as lava flows, pyroclastic deposits, and
191 subvolcanic sills (Briand et al., 1995, 1992). Mafic rocks exhibit a large range of
192 geochemical signatures ranging from tholeiitic to alkaline and calc-alkaline (Briand et
193 al., 1992; Pouplet et al., 2017). The crust-derived magmas attest to the reworking of
194 Ediacaran sediments (Couzinié et al., 2022, 2017), while mafic magmas would
195 originate from the lithospheric and asthenospheric mantle, with the subordinate
196 involvement of a garnet-bearing source (Pin and Marini, 1993; Pouplet et al., 2017).
197 The latest Ediacaran crustal melting was possibly a distal manifestation of the

198 Cadomian orogenic events (Couzinié et al., 2017), while Cambro-Ordovician crust-
199 mantle magmatism should be tied to protracted lithosphere extension that prevailed at
200 that time along the northern Gondwana margin (Chelle-Michou et al., 2017; Couzinié
201 et al., 2022; Pin, 1990; Pin and Marini, 1993).

202 2.2 The Monts-du-Lyonnais metamorphic complex

203 The Monts-du-Lyonnais metamorphic complex (Fig. 2) belongs to the Upper Gneiss
204 Unit. Its litho-tectonic pile consists of a set of amphibolite-(granulite-)facies
205 metamorphic rocks including from bottom to top (Feybesse et al., 1995): (i) a lower
206 metasedimentary unit corresponding to cordierite-bearing migmatites and garnet–
207 sillimanite–biotite paragneisses in the northwestern and southeastern part of the
208 complex, respectively, (ii) three (ultra)mafic–felsic rock associations cartographically
209 corresponding to “belts” and assimilated to LACs by Chantraine et al. (2003); (iii) mildly
210 peraluminous, locally anatectic orthogneisses; (iv) an upper metasedimentary unit,
211 also migmatitic, with relics of high-pressure granulite-facies metamorphism. The first,
212 southernmost (ultra)mafic–felsic belt includes 100–3000 m-long amphibolite boudins
213 corresponding to retrogressed eclogites stretched within a paragneiss matrix and
214 associated with garnet-bearing mantle peridotites (Blanc, 1981; Gardien et al., 1990).
215 The second, northernmost Chaussan belt is composed of fine-grained leucogneisses
216 (leptynites) enclosing numerous hecto- to kilometric massifs of meta-igneous mafic
217 and felsic granulites (Dufour, 1985). Finally, the Riverie belt located in-between the
218 previous two features an association of amphibolites and amphibole-bearing gneisses,
219 locally leucocratic (leptynites) (Blanc, 1981).

220 Metasediments experienced peak metamorphic conditions of 750–800°C at 7–9 kbar
221 coeval to the development of the regional foliation S₁₋₂ (Feybesse et al., 1995; Gardien
222 et al., 1990). Anatexis initiated at that stage and persisted during exhumation down to

223 c. 4 kbar. The age of this anatexis is poorly constrained, as the only published data
224 consist of a whole-rock Rb–Sr isochron date of 384 ± 16 Ma, interpreted as the age of
225 partial melting (Duthou et al., 1994). Relictual kyanite in metasediments suggests an
226 early high-pressure evolution at $P > 10$ kbar (Feybesse et al., 1995). Rocks from the
227 LACs record different metamorphic conditions. Eclogites from the southern belt
228 experienced peak conditions of $P > 15$ kbar and $750\text{--}850^\circ\text{C}$ (Dufour et al., 1985; Joanny
229 et al., 1991). One coesite grain retrieved from an eclogite sample would even suggest
230 $P > 28$ kbar (Lardeaux et al., 2001). Meta-igneous granulites from the Chaussan belt
231 record P of 8–10 kbar and T in the range $800\text{--}870^\circ\text{C}$ (Dufour, 1985). Metamorphic
232 conditions for the Riverie belt have not been estimated but Feybesse et al. (1995)
233 stressed that these rocks lack any evidence of a high-pressure evolution.

234 A late event of ductile deformation thought to have occurred at around 500°C
235 (Feybesse et al., 1995; Gardien et al., 1990) juxtaposed the Monts-du-Lyonnais
236 metamorphic complex to the adjacent lower-grade Brévenne Unit (Fig. 2). The last
237 increment of this tectonic phase was marked by the activation of NE-SW trending
238 strike-slip shear zones and the intrusion of several synkinematic granitoids (Feybesse
239 et al., 1995) at $345\text{--}335$ Ma (Ar-Ar dating on micas and amphibole, Costa et al., 1993).
240 Notably, the Riverie LAC is bounded by such shear zones to the other constituents of
241 the metamorphic complex. Late brittle deformation reworked the original thrust contact
242 between the Monts-du-Lyonnais metamorphic complex and the underlying Pilat unit
243 (representing the parautochthonous terrains).

244 Little is known about the age of the Monts-du-Lyonnais metamorphic complex
245 protoliths. There are no chronological constraints available on the depositional age of
246 the detrital metasediments. The age of the orthogneiss protolith is estimated to be
247 around 470 Ma (based on zircon Pb evaporation and whole-rock Rb–Sr ages, Dufour,

248 1982; Feybesse et al., 1995), although Duthou et al. (1984) report a significantly older
249 whole-rock Rb–Sr isochron date of 502 ± 7 Ma. An identical date of 497 ± 8 Ma was
250 obtained for felsic granulites and interpreted as the emplacement age of their igneous
251 protolith (Duthou et al., 1981). Mafic meta-igneous rocks display a variety of
252 geochemical types, ranging from N–MORB to LREE-rich tholeiites and even
253 transitional rocks with alkaline affinities (Briand et al., 1995). They have never been
254 dated, and a Cambro–Ordovician emplacement age has been postulated by analogy
255 with other bimodal meta-igneous associations from the eFMC, notably in the nearby
256 Vivarais area (Chelle-Michou et al., 2017).

257 In the Riverie belt, felsic rocks described as “amphibole-bearing (felsic) gneisses” and
258 closely associated with amphibolites were first reported by Peterlongo (1958) and later
259 studied by Blanc (1981). The relationships between amphibole-bearing felsic gneisses
260 and amphibolites (the constituent rocks of the belt) are well-exposed in the disused
261 “Les Roches” quarry near Riverie (Fig. 2). Amphibole-bearing felsic gneisses known in
262 other eFMC LACs have been variously regarded as former pyroclastic/epiclastic rocks
263 coeval to the amphibolite protoliths (Pin and Lancelot, 1982), metadiorites (Bodinier et
264 al., 1986) or anatetic magmas formed by partial melting of the amphibolites at
265 Variscan times (Benmammar et al., 2020).

266

267 **3. Analytical methods**

268 Eight samples of amphibole-bearing felsic gneisses and four samples of amphibolites
269 collected from the pit#2 of the “Les Roches” quarry (GPS coordinates: 45.5964N,
270 4.5879E) were analyzed for major and trace element compositions by the ALS Global
271 firm (details on the procedures, detection limits and accuracy/reproducibility in

272 Supplementary text, full dataset available as Supplementary Table S1). Recalculation
273 and plotting of the whole-rock geochemical data were performed using the GCDkit
274 plugin for R (Janoušek et al., 2006). Mineral major element compositions were
275 obtained using a Zeiss EVO MA15 Scanning Electron Microscope at the Central
276 Analytical Facility of Stellenbosch University, South Africa. Mineral compositions were
277 determined by EDX (Energy Dispersive X-ray) analysis using an Oxford Instruments®
278 X-Max 20 mm² detector and the Oxford INCA software. Beam conditions were 20 kV
279 accelerating voltage, 1.5 nA probe current, a working distance of 8.5 mm and a
280 specimen beam current of 20 nA. Analyses were quantified using natural mineral
281 standards and representative mineral compositions are reported in the Supplementary
282 Table S2. Biotite and amphibole structural formulas (including ferric iron contents) were
283 calculated using the spreadsheets of Li et al., (2020a, 2020b). Two samples of
284 amphibole-bearing felsic gneisses (RV-1 and RV-2) were selected for zircon U–Pb–Hf
285 determinations to constrain the emplacement age and isotopic signature of their
286 protoliths. Zircon grains were separated from the crushed rock samples at Saint-
287 Etienne University using conventional techniques (sieving, panning, magnetic and
288 heavy liquids separation followed by handpicking). Selected grains were subsequently
289 cast into epoxy mounts and polished down to a subequatorial grain section. BSE and
290 CL-imaging were performed at the Central Analytical Facility of Stellenbosch University
291 using a Zeiss MERLIN Scanning Electron Microscope. In situ U–Pb dating and zircon
292 Lu–Hf isotope measurements were carried out by LA–ICP–MS at the J.W. Goethe
293 University, Frankfurt-am-Main (Germany). Plotting and calculation of Concordia dates
294 were performed using IsoplotR (Vermeesch, 2018). Information on the analytical
295 methods is presented in the Supplementary Text. The full datasets (standards and
296 samples) are reported in Supplementary Tables S3 to S6.

298 **4. Sample petrography and geochemistry**

299 The Riverie belt occurs as a tectonic boudin bounded by dextral shear zones and syn-
300 kinematic (mylonitic) granites (Fig. 2a). In the largest pit (#2) of the disused Les Roches
301 quarry (Fig. 2b), felsic gneisses exhibiting a vertical foliation and wrapping around 1 to
302 3 m-wide amphibolite bodies (Fig. 3a,b) constitute the main petrographic type.
303 Amphibolites are particularly abundant in the SE part of the pit. Both mafic and felsic
304 rocks are cut across by a network of decimeter-scale discordant or concordant granitic
305 and pegmatitic veins.

306 The felsic gneisses are primarily composed of plagioclase, quartz, green amphibole
307 with low amounts of brown biotite either in the matrix or rimming amphibole (Fig.
308 3c,d,e). The foliation is underlined by alternating layers with varying proportions of
309 mafic minerals (Fig. 3c). The felsic rocks show a high-temperature texture with
310 interlobate grain contacts and preservation of high-energy surfaces (Fig. 3d), with
311 amphibole often being interstitial. Inclusions of plagioclase in amphibole and vice versa
312 are locally observed (Fig. 3e). Amphibole is a magnesio-ferri-hornblende with mg# of
313 0.63 and $\text{Fe}^{3+}/\text{Fe}^{\text{tot}}$ ratios in the range 0.29–0.37, slightly higher than the value (0.27)
314 estimated through wet chemistry by Blanc (1981). Biotite is also magnesian, with mg#
315 of 0.65–0.72, and TiO_2 -rich (>3 wt.%). Plagioclase is chemically unzoned and has an
316 oligoclase composition (An_{24-26}). Accessory minerals are magnetite, apatite, zircon,
317 and sulphides (Fig. 3c,d,e). The edenite–richterite thermometer of Holland and Blundy
318 (1994) and the barometer of Molina et al. (2015) for paired plagioclase–amphibole
319 compositions yielded equilibration temperatures of c. 700 °C for upper to mid-crustal
320 pressures of 2–4 kbar.

321 The amphibole-bearing felsic gneisses do not deviate from the igneous trend in the
322 FMW plot of Ohta and Arai (2007) which points to an igneous and not
323 volcanosedimentary origin for their protoliths (Fig. 4a). They show SiO₂ contents
324 ranging from 61 to 69 wt.%, reflecting the varying mineral modes at the scale of the
325 quarry (50 m). They are metaluminous to subaluminous with A/CNK (molar Al₂O₃/[CaO
326 + Na₂O + K₂O]) below 1.05, and markedly poor in K₂O (\leq 1 wt.% and mostly below 0.7
327 wt.%, Table S1). Accordingly, they plot in the field of tonalites in the P–Q diagram of
328 Debon and Le Fort (1983) (Fig. 4b). All samples show similar immobile, incompatible
329 trace elements patterns characterized by overall low concentrations. The amphibole-
330 bearing felsic gneisses are depleted in HREE (by a factor 0.3 to 0.6) and slightly
331 enriched in LREE–Zr (by a factor 2 to 3) and Th (10 times) with respect to N-MORBs
332 (Fig. 4c). Of importance are the pronounced Nb and Ti negative anomalies (with
333 Nb/Nb*: 0.2–0.3; Ti/Ti*: 0.3–0.6), along with a weakly positive Zr anomaly (Zr/Zr*: 1.2–
334 2.1). Th/Nb ratios are high, clustering around 0.6–0.7 (Fig. 4e). The concentrations of
335 LILE such as Ba (100–400 ppm), Sr (200–300 ppm) and Rb (8–20 ppm) are lower than
336 those of the Bulk Continental Crust (Rudnick and Gao, 2003). Chondrite-normalized
337 REE patterns (Boynton, 1984) are moderately fractionated (La_N/Yb_N = 2.9–7.1) and
338 show a slight depletion in mid-HREE (Dy to Tm, Fig. 4d). A weak Eu negative anomaly
339 is observed (Eu/Eu* = 0.71–0.95). Vanadium contents are low (78–151 ppm) with V/Ti
340 ratios close to 20 (Fig. 4f). Most trace element compositions (except Zr) show a rough
341 decrease with the SiO₂ content.

342 The mafic rocks have a nematoblastic texture and are dominantly composed of an
343 equigranular assemblage of euhedral to subhedral amphibole and plagioclase (Fig. 4f)
344 with apatite and titanite as the main accessory minerals. These amphibolites show
345 mildly alkaline basic compositions (SiO₂: 46.6–51.9 wt.%; Na₂O+K₂O: 4.2–5.1 wt.%,

346 Fig. 4b). Three samples show primitive compositions (i.e. close to that of primary
347 mantle-derived melts) as indicated by their elevated Mg# (62–63), MgO (7.5–9.0 wt.%)
348 and Cr (270–320 ppm) contents and the lack of Eu anomaly. They are slightly enriched
349 in Th and LREE with respect to N-MORBs, and three samples display a pronounced
350 negative Nb anomaly (with $\text{Th}/\text{Nb} > 0.2$, Fig. 4c,e). REE patterns are nearly flat ($\text{La}_{\text{N}}/\text{Yb}_{\text{N}}$
351 = 1.5–2.0, Fig. 4d). Vanadium contents are moderately elevated (227–362 ppm) with
352 V/Ti ratios between 25 and 40 (Fig. 4f).

353 Several observations suggest that the igneous protolith of the amphibole-bearing felsic
354 gneisses was plutonic and coeval to or younger than that of the amphibolites: (i) the
355 contacts between the two rock types are often intricate, with preserved evidence for
356 intrusive relationships of the former in the latter (see white triangles, Fig. 3a); (ii) pluri-
357 centimetric amphibole-rich clusters in the felsic rocks resemble assimilated mafic
358 material (black triangle, Fig. 3a); (iii) the foliation of the gneisses fades in strain
359 shadows at the edges of the mafic bodies so that the felsic rock appears isotropic
360 (white triangle, Fig. 3b).

361

362 5. Zircon data

363 5.1 Zircon textures

364 Zircon grains extracted from amphibole-bearing felsic gneisses are euhedral to
365 subhedral, ranging in length between 70 and 200 μm , and often show width-to-length
366 ratios higher than 1:2 with well-developed pyramidal tips (Fig. 5a). A few grains are
367 stubbier with lower aspect ratios down to 1:1. CL-images reveal concentric oscillatory
368 zoning, locally associated with sector zoning (see for instance zircon 1 of sample RV-
369 2, Fig. 5a). The zoning pattern may differ from the inner to outer part of few grains, due

370 to varying relative growth rate of crystal faces upon crystallization (white triangles on
371 Fig. 5a). However, there is no marked textural break such as a change in CL intensity
372 or clear evidence for resorption. Only very thin (<10 µm-large) CL-bright overgrowths
373 truncate the zoning pattern of some grains. Local recrystallization is also evidenced
374 (black triangles on Fig. 5a).

375 5.2 U–Pb results

376 In gneiss sample RV–1, 40 measurements were performed on 32 grains, all within
377 zones displaying clear oscillatory zoning (Fig. 5a). Seven spots showed moderate
378 common Pb contents (up to 3%) and were markedly discordant. These spots will not
379 be discussed further. A total of 16 concordant spots are statistically equivalent, and a
380 Concordia date of 545.9 ± 1.9 Ma (± 6.4 Ma after propagation of systematic
381 uncertainties) can be calculated from them (MSWD of concordance and equivalence
382 = 1.6). Besides, 6 analyses yielded similar $^{206}\text{Pb}/^{238}\text{U}$ dates but were discordant,
383 presumably owing to small amounts of common Pb. Eleven analyses showed younger,
384 slightly discordant to concordant $^{206}\text{Pb}/^{238}\text{U}$ dates ranging between 536 ± 10 and 509
385 ± 9 Ma.

386 In gneiss sample RV–2, 33 analyses were performed on 25 grains. A Concordia date
387 of 543.9 ± 1.5 Ma (± 6.3 after propagation of systematic uncertainties) can be
388 calculated from 19 statistically equivalent concordant analyses (with a MSWD of
389 concordance and equivalence equal to 1.4, Fig. 5b). Spot a58 yielded an identical yet
390 discordant $^{206}\text{Pb}/^{238}\text{U}$ date owing to the presence of common Pb. Nine measurements
391 devoid of common Pb yielded concordant to moderately discordant $^{206}\text{Pb}/^{238}\text{U}$ dates
392 ranging from 536 ± 6 down to 520 ± 6 Ma. Two analyses (a50 and a60) characterized
393 by minor common Pb contents (0.3–0.8%) showed discordant and younger $^{206}\text{Pb}/^{238}\text{U}$
394 dates of 484 ± 5 and 438 ± 7 Ma respectively. Two measurements performed on a

395 single zircon grain yielded a concordant $^{206}\text{Pb}/^{238}\text{U}$ date of 361 ± 4 Ma and a discordant
396 $^{206}\text{Pb}/^{238}\text{U}$ date of 354 ± 4 Ma (estimated common Pb content: 0.4%). Both also
397 featured markedly lower Th/U ratios (0.02 and 0.04, respectively) than grains yielding
398 $^{206}\text{Pb}/^{238}\text{U}$ dates of c. 545 Ma (always >0.15).

399 5.3 Lu–Hf isotopes

400 Twenty-eight measurements were performed on grain domains analogous to those
401 that previously yielded concordant $^{206}\text{Pb}/^{238}\text{U}$ dates (at ca. 545 Ma) and three on
402 undated grains texturally identical to the main zircon population. Initial Hf isotope
403 compositions were calculated using the intrusion age determined for each sample. The
404 $^{176}\text{Hf}/^{177}\text{Hf}(t)$ ratios of RV-1 zircons were all identical within uncertainty, ranging from
405 0.282709 ± 42 to 0.282752 ± 35 (at 2s), corresponding to $\epsilon\text{Hf}(t)$ of +9.5 to +11.0 with
406 an average value of $+10.5 \pm 0.9$ (2 S.D. – standard deviation; n = 14; Fig. 6). Zircons
407 from sample RV-2 showed a similar range of $^{176}\text{Hf}/^{177}\text{Hf}(t)$ ratios, from 0.282717 ± 33
408 to 0.282787 ± 44 (2 S.E.) corresponding to $\epsilon\text{Hf}(t)$ of +9.7 to +12.2 and yielding an
409 identical average $\epsilon\text{Hf}(t)$ at 10.6 ± 1.2 (2 S.D.; n = 18).

410

411 **6. Discussion**

412 **6.1 Interpretation of U–Pb data**

413 Field relationships, petrographic, and geochemical data indicate that the amphibole-
414 bearing felsic gneisses represent former tonalites (see section 4). Zircon grains show
415 euhedral shapes and oscillatory zoning, as typically observed in zircon grown from
416 melts (Corfu et al., 2003). Hence, the Concordia dates of 545.9 ± 1.9 (6.4) and 543.9
417 ± 1.5 (6.3) Ma are interpreted as late Ediacaran crystallization ages of the
418 (meta)tonalites RV-1 and RV-2, respectively. The other, discordant, zircon U-Pb data

419 for both samples can be explained by a combination of initial Pb incorporation and/or
420 Pb loss from zircons that originally belonged to the dominant population of concordant,
421 c. 545 Ma-old grains. This interpretation is consistent with the fact that all zircons show
422 identical $^{176}\text{Hf}/^{177}\text{Hf}$ ratios within uncertainties regardless the apparent $^{206}\text{Pb}/^{238}\text{U}$ date,
423 as disturbance of the U–Pb system does not affect Hf isotopes (Gerdes and Zeh,
424 2009).

425 Analyses a65 and a66 were both performed close to the rims of the same zircon grain
426 and showed younger $^{238}\text{U}/^{206}\text{Pb}$ dates of c. 360 Ma, concordant for a65. CL images do
427 not provide clear evidence for the existence of textural discontinuities associated with
428 new zircon growth or extensive zircon recrystallization. Yet, both analyses show very
429 low Th/U ratios, different from the main c. 545 Ma population. This suggests that upon
430 laser ablation both analyses may have (partly or wholly) sampled narrow CL-bright
431 overgrowths or recrystallized domains visible on a few grains (Fig. 5a). Therefore, it is
432 unclear whether the c. 360 Ma dates correspond to the age of a Variscan metamorphic
433 overprint, which would be in agreement with what is observed in the Upper Gneiss Unit
434 of the eFMC (Chelle-Michou et al., 2017), or represent geologically meaningless,
435 mixed ages.

436 **6.2 Typology of the mafic–felsic association**

437 At the scale of the quarry outcrop (approximately 50 m), the (meta)tonalites exhibit a
438 range of major element compositions yet very similar mineral assemblages. Since they
439 derive from a plutonic protolith, these characteristics may reflect different proportions
440 between igneous minerals, resulting from variable extents of crystal accumulation
441 versus crystal/melt separation during solidification of a mush at the emplacement site
442 (e.g. Barnes et al., 2016; Cornet et al., 2022; Laurent et al., 2020; Lee and Morton,
443 2015). By considering a crystallizing low-K dacitic melt with a chemical composition

similar to the average of the (meta)tonalites, the samples can be modeled as a combination of (Fig. 7): (i) residual melts resulting from the separation of 5–20 wt.% plagioclase An₂₅ + hornblende ± magnetite from the initial melt (for samples LY25, RV-1, RV-2); (ii) cumulates, corresponding to the initial melt plus 5–25 wt.% accumulated plagioclase An₂₅ ± hornblende ± magnetite (for samples LY23, -24, 26, -27, -28). Trace element data are consistent with this interpretation given the relatively gradual decrease in most trace elements with SiO₂ contents.

In general, low-K dacitic melts are known to derive from mantle melting followed by fractionation of a primary H₂O-rich basaltic melt or from dehydration melting of amphibolites (Beard, 1995; Stern et al., 1996). Zircon Hf isotope data indicate that the dacitic melt from which the Riverie felsic rocks originated had a composition overlapping with that of the Depleted Mantle (DM) reservoir at c. 545 Ma, ruling out an origin by melting of an old mafic (amphibolitic) crust (Fig. 6). Therefore, we favor the formation of the dacitic melt through crystal fractionation from a primary mantle-derived melt, consistent with its weak depletion in mid-HREE (Dy to Tm) and the Eu negative anomaly, which are indicative of amphibole and plagioclase fractionation (Bédard, 2006; Nandedkar et al., 2016). The pronounced Nb–Ti negative anomaly (Fig. 4c) and the radiogenic Hf isotope composition ($\epsilon_{\text{Hf}}(545\text{Ma})$ of c. +11) of the low-K dacitic melt collectively indicate that its depleted mantle source had been metasomatized by fluids derived from an oceanic slab (Fig. 4e; Pearce and Peate, 1995). The presence of magnetite, the elevated amphibole Fe³⁺/Fe_{tot} as well as the low bulk-rock V/Ti ratios displayed by the (meta)tonalites are consistent with a parental melt having formed under relatively oxidizing conditions (Fig. 4f), which aligns with a metasomatized mantle source.

468 The country-rocks of the tonalitic intrusion corresponded to gabbros or basalts (now
469 amphibolites). Those have near-primary mantle melt compositions which entails that
470 their negative Nb anomalies can be regarded as pristine and not related to crustal
471 contamination (Fig. 4e). Therefore, the igneous protolith of the amphibolites originated
472 from a mantle having incorporated a slab-derived component, as for the parental melt
473 of the (meta)tonalites, meaning that both mafic and felsic rocks were possibly
474 generated from the same metasomatized mantle source.

475 **6.3 Geodynamic setting of the Riverie magmatism**

476

477 As demonstrated in the previous section, the felsic rocks from the Riverie belt can be
478 traced back to a mantle metasomatized by slab-derived fluids shortly prior to melting,
479 namely in the Ediacaran period. At that time, the terrains currently exposed in the
480 eFMC were situated along the northern Gondwana margin, which was significantly
481 influenced by the Avalonian–Cadomian accretionary orogeny (Andonaegui et al., 2016;
482 Collett et al., 2020; Garfunkel, 2015; Linnemann et al., 2014, 2008; Soejono et al.,
483 2017). Therefore, it is likely that the Riverie magmatism tapped into a mantle imprinted
484 by Cadomian subduction. In fact, the Riverie rocks share isotopic similarities with the
485 late Cryogenian–early Ediacaran juvenile arc rocks of the Cadomian type-area in
486 northern France (Samson et al., 2003; Fig. 6).

487 According to full-plate tectonic models, the southwards subduction of the
488 Iapetus/Mirovoi oceans was still ongoing at the late Ediacaran/early Cambrian
489 transition (Fig. 8a, Merdith et al., 2021). Consistently, evidence for the existence of
490 0.55 Ga juvenile arcs along the northern Gondwana margin is provided by the detrital
491 zircon record of the parautochthonous terrains in the eFMC (Couzinié et al., 2019), the
492 Corsica basement (Avigad et al., 2018), the Upper Allochthon of the Iberian Massif

493 (Albert et al., 2015), and the Polish Góry Sowie Massif (Tabaud et al., 2021).
494 Additionally, in the Ossa-Morena Zone of the Iberian Massif, juvenile arc-derived
495 magmatism is represented by andesites–dacites interbedded within the late
496 Ediacaran/early Cambrian Malcycinado/San Jerónimo formations and diorites–
497 tonalites from the c. 555 Ma-old Mérida–Montoro igneous complex (Bandres et al.,
498 2002; Pin et al., 2002). Both suites exhibit positive ϵ Nd(t) values along with trace
499 element characteristics that resemble the Riverie (meta)tonalites.

500 In the Maures massif, the Bormes orthogneiss was recently regarded as a remnant of
501 an Ediacaran (590–556 Ma) arc by Tabaud et al. (2023). However, the presence in
502 their samples of 505–460 Ma-old zircon rims together with the major and trace element
503 signature of the peraluminous high-K host rocks rather suggest that they represent
504 Cambrian–Ordovician crust-derived granitoids related to the rifting event that led to the
505 opening of the Variscan oceans (e.g. Couzinié et al., 2022). Arc magmatism in the
506 Maures massif is more likely represented by the Arcs–Gassin *leptynites*, which have
507 ϵ Nd(t) values ranging from +1 to +2 and yielded a protolith emplacement age of 548
508 +15/-7 Ma (U–Pb on zircon; Innocent et al., 2003). As this age was obtained by isotope-
509 dilution thermal ionization mass spectrometry on multi-grain fractions, it deserves to
510 be confirmed using in situ techniques (Paquette et al., 2017).

511 The Riverie rocks represent modest volumes and their V/Ti systematics suggest a
512 distal position with respect to the Cadomian arc (Fig. 4f). Therefore, we infer that this
513 juvenile magmatism would have occurred within the back-arc domain of the Cadomian
514 orogen and resulted from the convective thinning of the lithospheric mantle (Fig. 8b).

515 **6.4 Implications for the architecture of the eFMC**
516

517 The Riverie mafic–felsic association represents the first unambiguous record of late
518 Ediacaran magmatism in the Upper Gneiss Unit of the eFMC and is distinctly different
519 from coeval magmatic rocks in the parautochthonous terrains (Fig. 4). In the latter, the
520 c. 550–530 Ma period is marked by voluminous peraluminous felsic magmatism, which
521 corresponds today to the Velay Orthogneiss Formation (Couzinié et al., 2017), the
522 Montredon-Labessonnié orthogneiss (Couzinié and Laurent, 2021), the Plaisance–
523 Cammazes orthogneiss (Guérangé-Lozes et al., 2013) and the Rivernous and Sériès
524 dacites–rhyolites in the Montagne Noire area (Lescuyer and Cocherie, 1992; Padel et
525 al., 2017). Collectively, the geochemical (major/trace element and isotopic) signatures
526 (Fig. 4) and zircon inheritance patterns exhibited by these rocks indicate significant
527 crust reworking through the melting of Neoproterozoic sedimentary sequences (Chelle-
528 Michou et al., 2017; Couzinié et al., 2017). The absence of evidence for late Ediacaran
529 compressional deformation (Álvaro et al., 2014) suggests that this crustal melting event
530 took place in an extensional environment, presumably in the back-arc of the Cadomian
531 orogen (Couzinié and Laurent, 2021). The very contrasted typology of late Ediacaran
532 magmatism between the Upper Gneiss Unit and the parautochthonous terrains
533 indicates that they represent two distinct crust segments which had different
534 paleogeographic positions within the late Ediacaran Cadomian back-arc.

535 The age of magmatism observed in the Riverie belt is unusual compared to other
536 eFMC LACs. The compilation of LA-ICP-MS zircon U-Pb dates obtained from LACs'
537 meta-igneous rocks (Fig. 9) indicates that magmatism mostly occurred between 492
538 and 472 Ma i.e., the Furongian–Lower Ordovician epochs (Chelle-Michou et al., 2017;
539 de Hoÿm de Marien et al., 2023; Lotout et al., 2020, 2018; Paquette et al., 2017;
540 Whitney et al., 2020). However, the rocks from the Riverie belt are at least 50 million
541 years older, dating back to the late Ediacaran period. Furthermore, the meta-igneous

542 felsic rocks of the LACs are generally potassic and display time-integrated
543 unradiogenic Nd-Hf isotope compositions ($\epsilon_{\text{Nd(t)}} < -3$; $\epsilon_{\text{Hf(t)}} < -1$), which is interpreted
544 as reflecting an origin through melting of the local continental crust (Chelle-Michou et
545 al., 2017; Pin and Marini, 1993). In contrast, the felsic rocks in the Riverie belt are
546 sodic, have radiogenic Hf isotope compositions, and ultimately originated from a
547 juvenile source. The pressure and temperature of mineral equilibration estimated for
548 the Riverie felsic rocks are close to the tonalite solidus (Schmidt and Thompson, 1996)
549 at relatively low pressures (2–4 kbar), possibly reflecting the crystallization conditions
550 of the parental low-K dacitic melt. These rocks do not record evidence for a high-
551 pressure metamorphic evolution, and no eclogite has ever been recovered from the
552 Riverie belt (Blanc, 1981; Feybesse et al., 1995). Collectively, petrographic,
553 geochemical (including isotopic) and geochronological data obtained on the Riverie
554 belt show that the igneous protoliths of this LAC did not form during the rifting of the
555 northern Gondwana margin that resulted in the opening of the Mid-Variscan ocean and
556 were presumably not subducted during the Devonian. These results highlight that all
557 LACs from the Monts-du-Lyonnais, and more generally from the eFMC, are not
558 identical in terms of age, petrogenesis and metamorphic evolution, arguing against
559 their grouping as a single litho-tectonic unit.

560

561 **6 Conclusion**

562 The amphibole-bearing felsic gneisses from the Riverie LAC in the Monts-du-Lyonnais
563 metamorphic complex represent a former tonalitic intrusion of late Ediacaran age (c.
564 545 Ma). The parental melt underwent variable amounts (5–25 wt.%) of crystal
565 accumulation versus crystal/melt separation at the emplacement site and formed
566 through fractionation of a mafic melt that originated from a mantle source

567 metasomatized by slab-derived fluids. The (meta)tonalites are intimately associated
568 with mafic (meta-)igneous rocks, which were likely derived from the same source. The
569 Riverie mafic–felsic association is unrelated to the Furongian (late Cambrian)–Lower
570 Ordovician rifting that resulted in the opening of the Mid-Variscan ocean and instead
571 represents a newly identified remnant of Cadomian arc/back-arc magmatism along the
572 northern Gondwana margin. Overall, our results challenge the assumption that all
573 mafic–felsic associations (LACs) from the high-grade domains of the eFMC can be
574 grouped together as a single litho-tectonic unit (“the” LAC). A detailed reexamination
575 of undated LACs in the eFMC (e.g. the Artense, Sioule, Truyère, Marvejols massifs)
576 using modern techniques is essential for clarifying the diversity of these associations
577 and refining their correlations.

578

579 **Acknowledgements**

580 C. Guilbaud made the thin sections. G. Stevens and A. Gerdes granted access to the
581 Stellenbosch CAF and Frankfurt LA–ICP–MS laboratory, respectively. A. Laurie, M. R.
582 Franzenburg and L. Marko assisted during the SEM and LA–ICP–MS sessions. O.
583 Vanderhaeghe provided a template for Fig. 1. L.-S. Doucet drew Fig. 9a. H. Bertrand
584 introduced the quarry to SC in 2011. Thorough reviews were provided by F. Roger and
585 an anonymous reviewer. The manuscript was handled by V. Bosse and L. Jolivet. We
586 extend our gratitude to all of them.

587 This work is dedicated to the memory of J.-L. Paquette, our collaborator for a decade,
588 for all his input on topics related to the eFMC, geochronology and granitoids.

589 **Figure captions**

590 Figure 1. (a) Sketch map depicting the exposed Variscan domains of western Europe
591 and the location of the inferred suture zones, based on Schulmann et al. (2022). SXT:
592 Saxo-Thuringian suture. (b) Geological map of the eastern French Massif Central
593 showing the main nappe architecture. Are also depicted the locations/names of
594 "Leptynite-Amphibolite Complex" occurrences (in black), adapted from Chantraine et
595 al. (2003).

596 *Figure 1. (a) Carte simplifiée montrant les zones où affleurent les terrains varisques et*
597 *les sutures supposées. (b) Carte géologique de l'Est du Massif Central français oriental*
598 *localisant les zones où affleure les "complexes leptyno-amphiboliques".*

599 Figure 2. (a) Simplified geological map of the Monts-du-Lyonnais metamorphic
600 complex, adapted from Feybesse et al. (1995). (b) Aerial photograph of the Riverie
601 disused quarry, illustrating the location of the studied pit.

602 *Figure 2. (a) Carte géologique simplifiée du complexe métamorphique des Monts-du-*
603 *Lyonnais. (b) vue aérienne des anciennes carrières de Riverie.*

604 Figure 3: Field observations and petrography of the Riverie felsic gneisses and
605 amphibolites. (a) Amphibole-rich clusters embedded within the felsic gneisses (black
606 triangles) recalling assimilated mafic material. Veins of felsic rocks cutting across the
607 amphibolite (white triangles). (b) Felsic gneisses with plagioclase–quartz leucocratic
608 bands rimmed by coarse amphibole underlining the vertical foliation (black triangles)
609 and isotropic zones between the amphibolite boudins (white triangles). (c) Polarized-
610 light thin section scan showing the variation in amphibole mode typically observed in
611 the felsic gneisses. (d,e) Polarized-light photomicrographs of felsic gneisses illustrating
612 the main plagioclase–quartz–amphibole assemblage with biotite rimming amphibole.

613 (f) Polarized-light photomicrograph of a mafic rock showing the equigranular
614 plagioclase–amphibole assemblage.

615 *Figure 3. Observations de terrain et pétrographie des gneiss et amphibolites de*
616 *Riverie. (a) Amas riches en amphibole dans les gneiss (triangles noirs) pouvant*
617 *correspondre à du matériel mafique assimilé et veines de roches felsiques dans les*
618 *amphibolites (triangles blancs). (b) Gneiss felsiques avec des bandes leucocratiques*
619 *de plagioclase-quartz bordées par de l'amphibole soulignant la foliation verticale*
620 *(triangles noirs) et des zones isotropes entre les boudins d'amphibolite (triangles*
621 *blancs). (c) Variation de la proportion d'amphibole dans les gneiss.. (d, e) Assemblage*
622 *des gneiss à plagioclase-quartz-amphibole-biotite. (f) Assemblage équigranulaire*
623 *plagioclase-amphibole des amphibolites.*

624 Figure 4: Whole-rock geochemical data of the Riverie felsic gneisses and amphibolites.
625 (a) FMW diagram of Ohta and Arai (2007) demonstrating the igneous origin of felsic
626 gneisses. The M and F values characterize mafic and felsic rock sources, respectively.
627 The W value quantifies the degree of weathering. The references of data for
628 (presumably) meta-igneous from “Leptynite-Amphibolite Complexes” are available in
629 the Supplementary Text. (b) P–Q classification diagram of Debon and Le Fort (1983).
630 The dotted lines represent the contour encompassing 75% of the data (n=75) for the
631 Velay orthogneiss formation, a coeval (meta)igneous suite from the parautochthonous
632 terrains (Couzinié et al., 2017). (c) Incompatible, immobile element patterns of the
633 Riverie meta-igneous rocks normalized to the composition of NMORBs (Sun and
634 McDonough, 1989). (d) Chondrite-normalized (Boynton, 1984) Rare Earth Elements
635 patterns. (e) Th/Yb vs. Nb/Yb diagram of Pearce (2008). Oceanic rocks plot within the
636 MORB–OIB array. Magmas contaminated by the continental crust during ascent or
637 which mantle source incorporated a slab-derived (SZ) component plot in the volcanic

638 arc array. (f) V–Ti diagram of Shervais (1982). This diagram highlights the effects of
639 the change in vanadium redox state when the mantle is metasomatized by slab-derived
640 fluids. Vanadium becomes more incompatible and resulting magmas exhibit high V/Ti
641 ratios. The magnetite + amphibole fractionation trend is from Shervais (1982). Data for
642 the Bulk Continental Crust are from Rudnick and Gao (2003).

643 *Figure 4. Données géochimiques des roches totales des gneiss et amphibolites de*
644 *Riverie. (a) Diagramme FMW démontrant l'origine ignée des gneiss. (b) Diagramme*
645 *de classification P-Q de Debon et Le Fort (1983). (c) Profils d'éléments incompatibles*
646 *normalisés à la composition des N-MORB. (d) Profils de terres rares normalisés aux*
647 *chondrites. (e) Diagramme Th/Yb vs. Nb/Yb de Pearce (2008). Les roches océaniques*
648 *se situent dans le domaine MORB-OIB. Les magmas contaminés par la croûte*
649 *continentale lors de leur mise en place ou dont la source mantellique a incorporé un*
650 *composant dérivé de la plaque subduite se situent dans le domaine des arcs*
651 *volcaniques. (f) Diagramme V-Ti de Shervais (1982).*

652 Figure 5: Zircon textural and U–Pb–Hf data for the Riverie amphibole gneisses. (a)
653 Representative cathodoluminescence images with the locations of laser spots (white
654 and yellow circles for U–Pb and Lu–Hf analyses respectively) indicated along with the
655 spot name (aXX or YYa/b). The corresponding $^{206}\text{Pb}/^{238}\text{U}$ dates are quoted with 2σ
656 uncertainty, in Ma. All displayed analyses are concordant (except those in italic). Hf
657 isotope data are reported using the ϵHf calculated at the $^{206}\text{Pb}/^{238}\text{U}$ date obtained on
658 the same zircon domain, quoted with 2σ uncertainty. The white and black triangles
659 highlight changes in the zoning pattern and local grain recrystallization, respectively.
660 Laser spot sizes are 30 μm for U–Pb and 40 μm for Lu–Hf. (b) Tera-Wasserburg
661 diagrams ($^{238}\text{U}/^{206}\text{Pb}$ vs. $^{207}\text{Pb}/^{206}\text{Pb}$). Error ellipses and ages are displayed at 95%

662 level of uncertainty. Green ellipses are those considered for Concordia age
663 calculations. The reported MSWDs are those of concordance plus equivalence.

664 *Figure 5. Données texturales et U-Pb-Hf des zircons extraits des gneiss de Riverie. (a)*
665 *Images en cathodoluminescence montrant la zonation magmatique des grains et la*
666 *localisation de quelques points d'analyse. (b) Diagrammes Tera-Wasserburg. Les*
667 *ellipses vertes sont celles considérées pour les calculs d'âge Concordia.*

668 Figure 6: Measured $\epsilon\text{Hf}(t)$ on magmatic zircon grains, recalculated and plotted using
669 the $^{206}\text{Pb}/^{238}\text{U}$ date. When such value was not available, the crystallization age
670 determined for the sample was used. The range for the Depleted Mantle reservoir is
671 bracketed by the models of Naeraa et al. (2012) and Griffin et al. (2002). The
672 background red shading mimics the contours of the distribution of 223 zircon analyses
673 from crust-derived felsic (meta-)igneous rock from the French Massif Central (Chelle-
674 Michou et al., 2017; Couzinié et al., 2017; Moyen et al., 2017). These data are taken
675 as representative of the Hf isotopic composition of the local continental crust. Data for
676 the Armorican Massif Cadomian juvenile arc magmatism are from Samson et al.
677 (2003). An $\epsilon\text{Hf}(t)$ -time crust evolution array calculated with an average $^{176}\text{Lu}/^{177}\text{Hf}$ ratio
678 of 0.015 (Griffin et al., 2002) is also depicted.

679 *Figure 6. Valeurs de ϵHf des grains de zircon recalculées à l'âge de mise en place.*
680 *L'arrière-plan rouge représente la composition isotopique en Hf de la croûte*
681 *continentale de l'Est du Massif Central.*

682 Figure 7: Results of mass balance calculations performed by least-square regression
683 considering the average composition of felsic gneisses as representative of the
684 intrusive low-K dacitic melt. Samples LY25-, RV-1 and RV-2 are modelled as residual

685 melts, while the remaining samples are considered cumulates. Σr^2 represents the sum
686 of squared residuals.

687 *Figure 7. Résultats des calculs de bilan de masse réalisés par régression des moindres*
688 *carrés en considérant la composition moyenne des gneiss comme représentative du*
689 *liquide dacitique initial. Les échantillons LY25-, RV-1 et RV-2 sont modélisés comme*
690 *des liquides résiduels alors que les autres sont considérés comme des cumulats.*

691 Figure 8: (a) Paleogeography at 545 Ma based on the full-plate model of Merdith et al.
692 (2021), drawn using Python 3 with opensource packages pyGMT and pyGplates. The
693 yellow star depicts the putative location of the terrains today exposed in Upper Gneiss
694 Unit (UGU) of the eFMC. (b) Geodynamic sketch of the northern Gondwana margin at
695 545 Ma highlighting the context and mechanism through which the Riverie rocks
696 formed, inspired from Erdős et al. (2022).

697 *Figure 8. (a) Paléogéographie à 545 Ma basée sur le modèle de plaque de Merdith et*
698 *al. (2021). L'étoile indique l'emplacement supposé des terrains correspondant*
699 *aujourd'hui à l'Unité Supérieure des Gneiss. (b) Schéma géodynamique de la marge*
700 *nord du Gondwana à 545 Ma, soulignant le contexte et le mécanisme par lesquels les*
701 *roches de Riverie se sont formées.*

702 Figure 9: Available LA–ICP–MS zircon U–Pb data on meta-igneous rocks from the
703 “Leptynite–Amphibolite Complexes” in the eastern French Massif Central (represented
704 as Kernel Density Estimates of concordant $^{206}\text{Pb}/^{238}\text{U}$ dates (calculated with IsoplotR
705 using an adaptative bandwith). Zircon data are from Whitney et al. (2020) for the
706 Montagne Noire, de Hoÿm de Marien et al. (2023) for the Haut-Allier, Paquette et al.
707 (2017) for the Lot, Lotout et al. (2020, 2018) for the Rouergue, Chelle-Michou et al.
708 (2017) for the Vivarais, and this study for the Monts-du-Lyonnais.

709 *Figure 9. Données U-Pb sur zircons obtenues pour les roches métro-igneuses des*
710 *"complexes leptyno-amphiboliques" de l'Est du Massif Central français.*

711 **References**

- 712 Albert, R., Arenas, R., Gerdes, A., Sánchez Martínez, S., Fernández-Suárez, J., Fuenlabrada, J.M., 2015.
713 Provenance of the Variscan Upper Allochthon (Cabo Ortegal Complex, NW Iberian Massif).
714 Gondwana Research 28, 1434–1448. <https://doi.org/10.1016/j.gr.2014.10.016>
- 715 Álvaro, J.J., Bauluz, B., Clausen, S., Devaere, L., Gil Imaz, A., Monceret, É., Vizcaíno, D., 2014.
716 Stratigraphic review of the Cambrian-Lower Ordovician volcanosedimentary complexes from
717 the northern Montagne Noire, France. Stratigraphy 11, 83–96.
- 718 Andonaegui, P., Arenas, R., Albert, R., Sánchez Martínez, S., Díez Fernández, R., Gerdes, A., 2016. The
719 last stages of the Avalonian–Cadomian arc in NW Iberian Massif: isotopic and igneous record
720 for a long-lived peri-Gondwanan magmatic arc. Tectonophysics, Tectonic evolution of the
721 Iberian margin of Gondwana and of correlative regions: A celebration of the career of Cecilio
722 Quesada 681, 6–14. <https://doi.org/10.1016/j.tecto.2016.02.032>
- 723 Avigad, D., Rossi, Ph., Gerdes, A., Abbo, A., 2018. Cadomian metasediments and Ordovician
724 sandstone from Corsica: detrital zircon U–Pb–Hf constrains on their provenance and
725 paleogeography. Int J Earth Sci (Geol Rundsch) 107, 2803–2818.
726 <https://doi.org/10.1007/s00531-018-1629-3>
- 727 Bandres, A., Eguíluz, L., Gil Ibarguchi, J.I., Palacios, T., 2002. Geodynamic evolution of a Cadomian arc
728 region: the northern Ossa-Morena zone, Iberian massif. Tectonophysics, Massifs and
729 Correlations Across the Cadomo-Avalonian Orogens 352, 105–120.
730 [https://doi.org/10.1016/S0040-1951\(02\)00191-9](https://doi.org/10.1016/S0040-1951(02)00191-9)
- 731 Barnes, C.G., Coint, N., Yoshinobu, A., 2016. Crystal accumulation in a tilted arc batholith. American
732 Mineralogist 101, 1719–1734. <https://doi.org/10.2138/am-2016-5404>
- 733 Beard, J.S., 1995. Experimental, geological, and geochemical constraints on the origins of low-K silicic
734 magmas in oceanic arcs. Journal of Geophysical Research: Solid Earth 100, 15593–15600.
735 <https://doi.org/10.1029/95JB00861>
- 736 Bédard, J.H., 2006. Trace element partitioning in plagioclase feldspar. Geochimica et Cosmochimica
737 Acta 70, 3717–3742. <https://doi.org/10.1016/j.gca.2006.05.003>
- 738 Bellot, J.-P., Laverne, C., Bronner, G., 2010. An early Palaeozoic supra-subduction lithosphere in the
739 Variscides: new evidence from the Maures massif. Int J Earth Sci (Geol Rundsch) 99, 473–504.
740 <https://doi.org/10.1007/s00531-009-0416-6>
- 741 Benmammar, A., Berger, J., Triantafyllou, A., Duchene, S., Bendaoud, A., Baele, J.-M., Bruguier, O.,
742 Diot, H., 2020. Pressure-temperature conditions and significance of Upper Devonian eclogite
743 and amphibolite facies metamorphisms in southern French Massif central. Bulletin de la
744 Société Géologique de France 191, 28. <https://doi.org/10.1051/bsgf/2020033>
- 745 Blanc, D., 1981. Les roches basiques et ultrabasiques des Monts du Lyonnais. Etude pétrographique,
746 minéralogique et géochimique (PhD thesis).
- 747 Bodinier, J.L., Giraud, A., Dupuy, C., Leyreloup, A., Dostal, J., 1986. Caractérisation géochimique des
748 métabasites associées à la suture méridionale hercynienne : Massif Central français et
749 Chamrousse (Alpes). Bulletin de la Société Géologique de France 8, 115–123.
- 750 Bouchez, J.L., Jover, O., 1986. Le Massif Central : un chevauchement de type himalayen vers l'Ouest-
751 Nord-Ouest. Comptes Rendus de l'Académie des Sciences, Paris 302, 675–680.
- 752 Boynton, W.V., 1984. Cosmochemistry of the rare earth elements: meteorite studies, in: Henderson,
753 P. (Ed.), Rare Earth Element Geochemistry. Elsevier, Amsterdam, pp. 63–114.
- 754 Briand, B., Bouchardon, J.-L., Capiez, P., Piboule, M., 2002. Felsic (A-type)-basic (plume-induced)
755 Early Palaeozoic bimodal magmatism in the Maures Massif (southeastern France). Geological
756 Magazine 139. <https://doi.org/10.1017/s0016756802006477>

- 757 Briand, B., Bouchardon, J.-L., Ouali, H., Piboule, M., Capiez, P., 1995. Geochemistry of bimodal
758 amphibolite-felsic gneiss complexes from eastern Massif Central, France. *Geological*
759 *Magazine* 132, 321–337.
- 760 Briand, B., Bouchardon, J.-L., Santallier, D., Piboule, M., Ouali, H., Capiez, P., 1992. Alkaline affinity of
761 the metabasites in the gneissic series surrounding the Velay migmatitic domain. *Géologie de*
762 *la France* 2, 9–15.
- 763 Briand, B., Piboule, M., Santallier, D., Bouchardon, J.-L., 1991. Geochemistry and tectonic implications
764 of two Ordovician bimodal igneous complexes, southern French Massif Central. *Journal of*
765 *the Geological Society, London* 148, 959–971.
- 766 Burg, J.-P., Leyreloup, A.F., Marchand, J., Matte, P., 1984. Inverted metamorphic zonation and large
767 scale thrusting in the Variscan belt: An example in the French Massif central. *Journal of the*
768 *Geological Society, London* 14, 47–61.
- 769 Burg, J.-P., Matte, P., 1978. A cross section through the French Massif Central and the scope of its
770 Variscan geodynamic evolution. *Z. dt. geol. Ges.* 129, 429–460.
- 771 Chantraine, J., Autran, A., Cavelier, C., Bureau de recherches g??ologiques et mini??res (France),
772 2003. *Carte géologique de la France à l'échelle du millionième*, 6ème édition révisée, BRGM.
773 ed. Orléans.
- 774 Chelle-Michou, C., Laurent, O., Moyen, J.-F., Block, S., Paquette, J.-L., Couzinié, S., Gardien, V.,
775 Vanderhaeghe, O., Villaros, A., Zeh, A., 2017. Pre-Cadomian to late-Variscan odyssey of the
776 eastern Massif Central, France: Formation of the West European crust in a nutshell.
777 *Gondwana Research* 46, 170–190. <https://doi.org/10.1016/j.gr.2017.02.010>
- 778 Collett, S., Schulmann, K., Štípská, P., Míková, J., 2020. Chronological and geochemical constraints on
779 the pre-variscan tectonic history of the Erzgebirge, Saxothuringian Zone. *Gondwana Research*
780 79, 27–48. <https://doi.org/10.1016/j.gr.2019.09.009>
- 781 Corfu, F., Hanchar, J.M., Hoskin, P.W.O., Kinny, P.D., 2003. Atlas of Zircon Textures. *Reviews in*
782 *Mineralogy and Geochemistry* 53, 469–500.
- 783 Cornet, J., Bachmann, O., Ganne, J., Fiedrich, A., Huber, C., Deering, C.D., Feng, X., 2022. Assessing
784 the effect of melt extraction from mushy reservoirs on compositions of granitoids: From a
785 global database to a single batholith. *Geosphere* 18, 985–999.
786 <https://doi.org/10.1130/GES02333.1>
- 787 Costa, S., 1989. Age radiométrique ^{39}Ar - ^{40}Ar dating of the Barrovian metamorphism of the Lot
788 Valley series associated with the Marvejols nappe emplacement. *Comptes Rendus de*
789 *l'Académie des Sciences, Paris* 309, 561–567.
- 790 Costa, S., Maluski, H., Lardeaux, J.M., 1993. ^{40}Ar - ^{39}Ar chronology of Variscan tectono-metamorphic
791 events in an exhumed crustal nappe: the Monts du Lyonnais complex (Massif Central,
792 France). *Chemical Geology* 105, 339–359.
- 793 Couzinié, S., Bouilhol, P., Laurent, O., Grocolas, T., Montel, J.-M., 2022. Cambro-Ordovician
794 ferrosilicic magmatism along the northern Gondwana margin: constraints from the
795 Cézarenque-Joyeuse gneiss complex (French Massif Central). *BSGF - Earth Sciences Bulletin*
796 193.
- 797 Couzinié, S., Laurent, O., 2021. Zircon U-Pb dating of the Montredon-Labessonnié orthogneiss by LA-
798 ICP-MS: new evidence for late Ediacaran crustal melting in the French Massif Central.
799 *Géologie de la France* 1, 24–31.
- 800 Couzinié, S., Laurent, O., Chelle-Michou, C., Bouilhol, P., Paquette, J.-L., Gannoun, A.-M., Moyen, J.-F.,
801 2019. Detrital zircon U-Pb-Hf systematics of Ediacaran metasediments from the French
802 Massif Central: Consequences for the crustal evolution of the north Gondwana margin.
803 *Precambrian Research* 324, 269–284. <https://doi.org/10.1016/j.precamres.2019.01.016>
- 804 Couzinié, S., Laurent, O., Poujol, M., Mintrone, M., Chelle-Michou, C., Moyen, J.-F., Bouilhol, P.,
805 Vezinet, A., Marko, L., 2017. Cadomian S-type granites as basement rocks of the Variscan belt
806 (Massif Central, France): Implications for the crustal evolution of the north Gondwana
807 margin. *Lithos* 286–287, 16–34. <https://doi.org/10.1016/j.lithos.2017.06.001>

- 808 de Hoÿm de Marien, L., Pitra, P., Poujol, M., Cogné, N., Cagnard, F., Le Bayon, B., 2023. Complex
809 geochronological record of an emblematic Variscan eclogite (Haut-Allier, French Massif
810 Central). *Journal of Metamorphic Geology* 41, 967–995.
- 811 Debon, F., Le Fort, P., 1983. A chemical-mineralogical classification of common plutonic rocks and
812 associations. *Transactions of the Royal Society of Edinburgh* 73, 135–149.
- 813 Dewey, J.F., 1987. Suture, in: *Structural Geology and Tectonics, Encyclopedia of Earth Science*.
814 Springer, Berlin, Heidelberg, pp. 775–784. https://doi.org/10.1007/3-540-31080-0_115
- 815 Domeier, M., 2016. A plate tectonic scenario for the Iapetus and Rheic oceans. *Gondwana Research*
816 36, 275–295. <https://doi.org/10.1016/j.gr.2015.08.003>
- 817 Downes, H., Bodinier, J.L., Dupuy, C., Leyreloup, A.F., Dostal, J., 1989. Isotope and trace-element
818 heterogeneities in high-grade basic metamorphic rocks of Marvejols: Tectonic implications
819 for the Hercynian suture zone of the French Massif Central. *Lithos* 24, 37–54.
- 820 Dufour, E., 1985. Granulite facies metamorphism and retrogressive evolution of the Monts du
821 Lyonnais metabasites (Massif Central, France). *Lithos* 18, 97–113.
- 822 Dufour, E., 1982. Pétrologie et géochimie des formations orthométamorphiques acides des Monts du
823 Lyonnais (Massif central, France) (PhD thesis).
- 824 Dufour, E., Lardeaux, J.M., Coffrant, D., 1985. Eclogites et granulites dans les Monts du Lyonnais : une
825 évolution métamorphique plurifaciale éohercynienne. *Comptes Rendus de l'Académie des
826 Sciences, Paris* 300, 141–144.
- 827 Duthou, J.-L., Cantagrel, J.-M., Didier, J., Viallette, Y., 1984. Palaeozoic granitoids from the French
828 Massif Central: age and origin studied by ^{87}Sr - ^{87}Rb system. *Physics of the Earth and
829 Planetary Interiors* 35, 131–144.
- 830 Duthou, J.-L., Chenevroy, M., Gay, M., 1994. Rb-Sr middle Devonian age of cordierite bearing
831 migmatites from Lyonnais area (French Massif Central). *Comptes Rendus de l'Académie des
832 Sciences, Paris* 319, 791–796.
- 833 Duthou, J.-L., Piboule, M., Gay, M., Dufour, E., 1981. Datations radiométriques Rb-Sr sur les
834 orthogranulites des Monts du Lyonnais (Massif Central français). *Comptes Rendus de
835 l'Académie des Sciences, Paris* 292, 749–752.
- 836 Edel, J.B., Schulmann, K., Lexa, O., Lardeaux, J.M., 2018. Late Palaeozoic palaeomagnetic and tectonic
837 constraints for amalgamation of Pangea supercontinent in the European Variscan belt. *Earth-
838 Science Reviews* 177, 589–612. <https://doi.org/10.1016/j.earscirev.2017.12.007>
- 839 Erdős, Z., Huismans, R.S., Faccenna, C., 2022. Wide Versus Narrow Back-Arc Rifting: Control of
840 Subduction Velocity and Convective Back-Arc Thinning. *Tectonics* 41, e2021TC007086.
841 <https://doi.org/10.1029/2021TC007086>
- 842 Faure, M., Lardeaux, J.-M., Ledru, P., 2009. A review of the pre-Permian geology of the Variscan
843 French Massif Central. *Comptes Rendus Geoscience* 341, 202–213.
844 <https://doi.org/10.1016/j.crte.2008.12.001>
- 845 Feybesse, J.-L., Lardeaux, J.M., Tegyey, M., Peterlongo, J.-M., Kerrien, Y., Lemière, B., Maurin, G.,
846 Mercier, F., Thiéblemont, D., 1995. Notice explicative, Carte géol. France (1/50 000), feuille
847 Saint-Symphorien-sur-Coise (721). BRGM, Orléans.
- 848 Franke, W., Cocks, L.R.M., Torsvik, T.H., 2017. The Palaeozoic Variscan oceans revisited. *Gondwana
849 Research* 48, 257–284. <https://doi.org/10.1016/j.gr.2017.03.005>
- 850 Gardien, V., Lardeaux, J.M., Ledru, P., Allemand, P., Guillot, S., 1997. Metamorphism during late
851 orogenic extension : insights from the French Variscan belt. *Bulletin de la Société Géologique
852 de France* 168, 271–286.
- 853 Gardien, V., Martelat, J.-E., Leloup, P.-H., Mahéo, G., Bevillard, B., Allemand, P., Monié, P., Paquette,
854 J.-L., Grosjean, A.-S., Faure, M., Chelle-Michou, C., Fellah, C., 2022. Fast exhumation rate
855 during late orogenic extension: The new timing of the Pilat detachment fault (French Massif
856 Central, Variscan belt). *Gondwana Research* 103, 260–275.
857 <https://doi.org/10.1016/j.gr.2021.10.007>

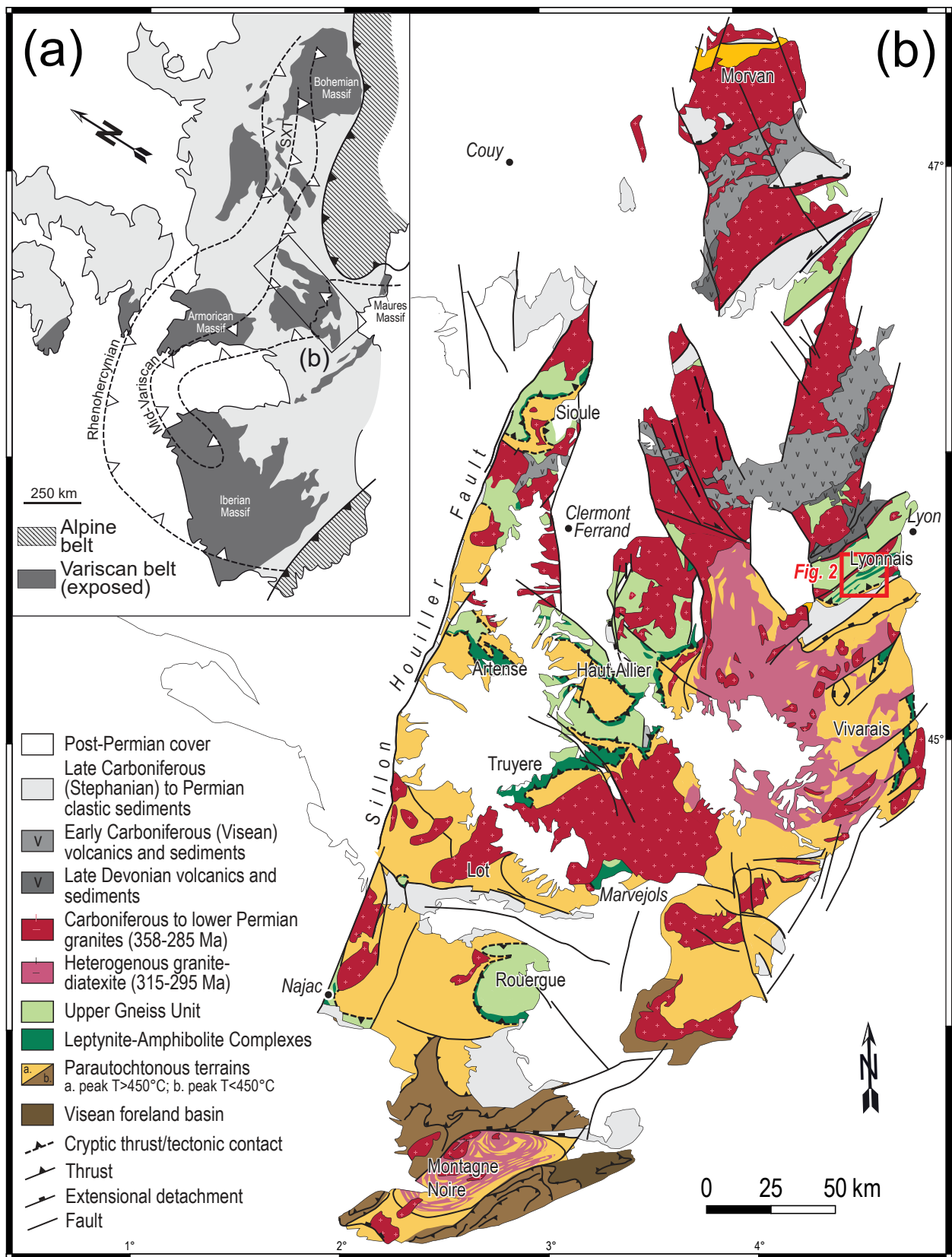
- 858 Gardien, V., Teygery, M., Lardeaux, J.M., Misseri, M., Dufour, E., 1990. Crust-mantle relationships in
859 the French Variscan chain: the example of the Southern Monts du Lyonnais unit (eastern
860 French Massif Central). *Journal of Metamorphic Geology* 8, 477–492.
- 861 Garfunkel, Z., 2015. The relations between Gondwana and the adjacent peripheral Cadomian
862 domain—constraints on the origin, history, and paleogeography of the peripheral domain.
863 *Gondwana Research* 28, 1257–1281. <https://doi.org/10.1016/j.gr.2015.05.011>
- 864 Gerdes, A., Zeh, A., 2009. Zircon formation versus zircon alteration — New insights from combined
865 U-Pb and Lu-Hf in-situ LA-ICP-MS analyses, and consequences for the interpretation of
866 Archean zircon from the Central Zone of the Limpopo Belt. *Chemical Geology* 261, 230–243.
867 <https://doi.org/10.1016/j.chemgeo.2008.03.005>
- 868 Giraud, A., Marchand, J., Dupuy, C., Dostal, J., 1984. Geochemistry of leptyno-amphibolite complex
869 from Haut Allier (French Massif Central). *Lithos* 17, 203–214.
- 870 Griffin, W.L., Wang, X., Jackson, S.E., Pearson, N.J., O'Reilly, S.Y., Xu, X.-S., Zhou, X., 2002. Zircon
871 chemistry and magma mixing, SE China: In-situ analysis of Hf isotopes, Tonglu and Pingtan
872 igneous complexes. *Lithos* 61, 237–269.
- 873 Guérangé-Lozes, J., Demange, M., Mouline, M., 2013. Notice explicative, Carte géol. France (1/50
874 000), feuille Castres (986). BRGM, Orléans.
- 875 Holland, T., Blundy, J., 1994. Non-ideal interactions in calcic amphiboles and their bearing on
876 amphibole-plagioclase thermometry. *Contributions to Mineralogy and Petrology*.
- 877 Innocent, C., Michard, A., Guerrot, C., Hamelin, B., 2003. Datation U-Pb sur zircons à 548 Ma de
878 leptynites des Maures centrales. Signification géodynamique des complexes leptyno-
879 amphibolitiques de l'Europe varisque. *Bulletin de la Société Géologique de France* 174, 585–
880 594.
- 881 Janoušek, V., Farrow, C.M., Erban, V., 2006. Interpretation of Whole-rock Geochemical Data in
882 Igneous Geochemistry: Introducing Geochemical Data Toolkit (GCDkit). *Journal of Petrology*
883 47, 1255–1259. <https://doi.org/10.1093/petrology/egl013>
- 884 Joanny, V., van Roermund, H., Lardeaux, J.M., 1991. The clinopyroxene/plagioclase symplectite in
885 retrograde eclogites: A potential geothermobarometer. *Geol Rundsch* 80, 303–320.
886 <https://doi.org/10.1007/BF01829368>
- 887 Jouffray, F., Lardeaux, J.-M., Tabaud, A.-S., Corsini, M., Schneider, J., 2023. Deciphering the nature
888 and age of the protoliths and peak P-T conditions in retrogressed mafic eclogites from the
889 Maures-Tannneron Massif (SE France) and implications for the southern European Variscides.
890 BSGF - Earth Sci. Bull. 194, 10. <https://doi.org/10.1051/bsgf/2023006>
- 891 Keppie, J.D., Nance, R.D., Murphy, J.B., Dostal, J., Braid, J.A., 2010. The high-pressure Iberian–Czech
892 belt in the Variscan orogen: Extrusion into the upper (Gondwanan) plate? *Gondwana*
893 Research 17, 306–316. <https://doi.org/10.1016/j.gr.2009.08.007>
- 894 Kröner, U., Romer, R.L., 2013. Two plates — Many subduction zones: The Variscan orogeny
895 reconsidered. *Gondwana Research* 24, 298–329. <https://doi.org/10.1016/j.gr.2013.03.001>
- 896 Lardeaux, J.-M., 2023. Metamorphism and linked deformation in understanding tectonic processes at
897 varied scales. *Comptes Rendus. Géoscience* 356, 1–25. <https://doi.org/10.5802/crgeos.204>
- 898 Lardeaux, J.M., Ledru, P., Daniel, I., Duchene, S., 2001. The Variscan French Massif Central – a new
899 addition of the ultra-high pressure metamorphic “club”: exhumation processes and
900 geodynamic consequences. *Tectonophysics* 332, 143–167.
- 901 Lardeaux, J.M., Schulmann, K., Faure, M., Janousek, V., Lexa, O., Skrzypek, E., Edel, J.B., Stipska, P.,
902 2014. The Moldanubian Zone in the French Massif Central, Vosges/Schwarzwald and
903 Bohemian Massif revisited: differences and similarities. *Geological Society, London, Special*
904 *Publications* 405, 7–44. <https://doi.org/10.1144/sp405.14>
- 905 Laurent, O., Björnsen, J., Wotzlaw, J.-F., Bretscher, S., Pimenta Silva, M., Moyen, J.-F., Ulmer, P.,
906 Bachmann, O., 2020. Earth's earliest granitoids are crystal-rich magma reservoirs tapped by
907 silicic eruptions. *Nat. Geosci.* 13, 163–169. <https://doi.org/10.1038/s41561-019-0520-6>

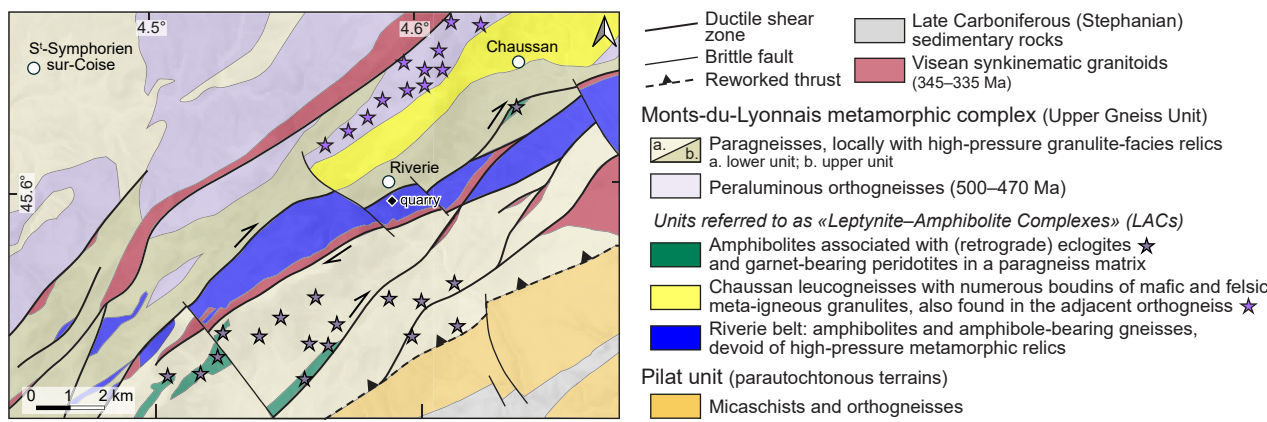
- 908 Ledru, P., Courrioux, G., Dallain, C., Lardeaux, J.M., Montel, J.M., Vanderhaeghe, O., Vitel, G., 2001.
909 The Velay dome (French Massif Central): melt generation and granite emplacement during
910 orogenic evolution. *Tectonophysics* 342, 207–237.
911 Ledru, P., Lardeaux, J.M., Santallier, D., Autran, A., Quenardel, J.-M., Floc'h, J.-P., Lerouge, G., Mallet,
912 N., Marchand, J., Ploquin, A., 1989. Where are the nappes in the French Massif central?
913 *Bulletin de la Société Géologique de France* 8, 605–618.
914 Lee, C.-T.A., Morton, D.M., 2015. High silica granites: Terminal porosity and crystal settling in shallow
915 magma chambers. *Earth and Planetary Science Letters* 409, 23–31.
916 <https://doi.org/10.1016/j.epsl.2014.10.040>
917 Lescuyer, J.-L., Cocherie, A., 1992. Single-zircon dating of the Sériès meta-dacites: evidence for a Late
918 Proterozoic age of the “X Schists” from Montagne Noire (Southern French Massif Central).
919 *Comptes Rendus de l'Académie des Sciences, Paris* 314, 1071–1077.
920 Li, X., Zhang, C., Behrens, H., Holtz, F., 2020a. Calculating amphibole formula from electron
921 microprobe analysis data using a machine learning method based on principal components
922 regression. *Lithos* 362–363, 105469. <https://doi.org/10.1016/j.lithos.2020.105469>
923 Li, X., Zhang, C., Behrens, H., Holtz, F., 2020b. Calculating biotite formula from electron microprobe
924 analysis data using a machine learning method based on principal components regression.
925 *Lithos* 356–357, 105371. <https://doi.org/10.1016/j.lithos.2020.105371>
926 Linnemann, U., Gerdes, A., Hofmann, M., Marko, L., 2014. The Cadomian Orogen: Neoproterozoic to
927 Early Cambrian crustal growth and orogenic zoning along the periphery of the West African
928 Craton—Constraints from U–Pb zircon ages and Hf isotopes (Schwarzburg Antiform,
929 Germany). *Precambrian Research* 244, 236–278.
930 <https://doi.org/10.1016/j.precamres.2013.08.007>
931 Linnemann, U., Pereira, F., Jeffries, T.E., Drost, K., Gerdes, A., 2008. The Cadomian Orogeny and the
932 opening of the Rheic Ocean: The diachrony of geotectonic processes constrained by LA-ICP-MS
933 U–Pb zircon dating (Ossa-Morena and Saxo-Thuringian Zones, Iberian and Bohemian
934 Massifs). *Tectonophysics* 461, 21–43. <https://doi.org/10.1016/j.tecto.2008.05.002>
935 Lotout, C., Pitra, P., Poujol, M., Anczkiewicz, R., Van Den Driessche, J., 2018. Timing and duration of
936 Variscan high-pressure metamorphism in the French Massif Central: A multimethod
937 geochronological study from the Najac Massif. *Lithos* 308–309, 381–394.
938 <https://doi.org/10.1016/j.lithos.2018.03.022>
939 Lotout, C., Poujol, M., Pitra, P., Anczkiewicz, R., Van Den Driessche, J., 2020. From Burial to
940 Exhumation: Emplacement and Metamorphism of Mafic Eclogitic Terranes Constrained
941 Through Multimethod Petrochronology, Case Study from the Lévezou Massif (French Massif
942 Central, Variscan Belt). *J Petrology* 61. <https://doi.org/10.1093/petrology/egaa046>
943 Maierová, P., Štípká, P., Gerya, T., Lexa, O., 2021. Trans-lithospheric diapirism explains the presence
944 of ultra-high pressure rocks in the European Variscides. *Communications Earth &*
945 *Environment* 2. <https://doi.org/10.1038/s43247-021-00122-w>
946 Matte, P., 1986. Tectonics and plate tectonics model for the Variscan belt of Europe. *Tectonophysics*
947 126, 329–374.
948 Merdith, A.S., Williams, S.E., Collins, A.S., Tetley, M.G., Mulder, J.A., Blades, M.L., Young, A.,
949 Armistead, S.E., Cannon, J., Zahirovic, S., Müller, R.D., 2021. Extending full-plate tectonic
950 models into deep time: Linking the Neoproterozoic and the Phanerozoic. *Earth-Science*
951 *Reviews* 214, 103477. <https://doi.org/10.1016/j.earscirev.2020.103477>
952 Molina, J.F., Moreno, J.A., Castro, A., Rodríguez, C., Fershtater, G.B., 2015. Calcic amphibole
953 thermobarometry in metamorphic and igneous rocks: New calibrations based on
954 plagioclase/amphibole Al-Si partitioning and amphibole/liquid Mg partitioning. *Lithos* 232,
955 286–305. <https://doi.org/10.1016/j.lithos.2015.06.027>
956 Moyen, J.F., Laurent, O., Chelle-Michou, C., Couzinié, S., Vanderhaeghe, O., Zeh, A., Villaros, A.,
957 Gardien, V., 2017. Collision vs. subduction-related magmatism: Two contrasting ways of
958 granite formation and implications for crustal growth. *Lithos* 277, 154–177.
959 <https://doi.org/10.1016/j.lithos.2016.09.018>

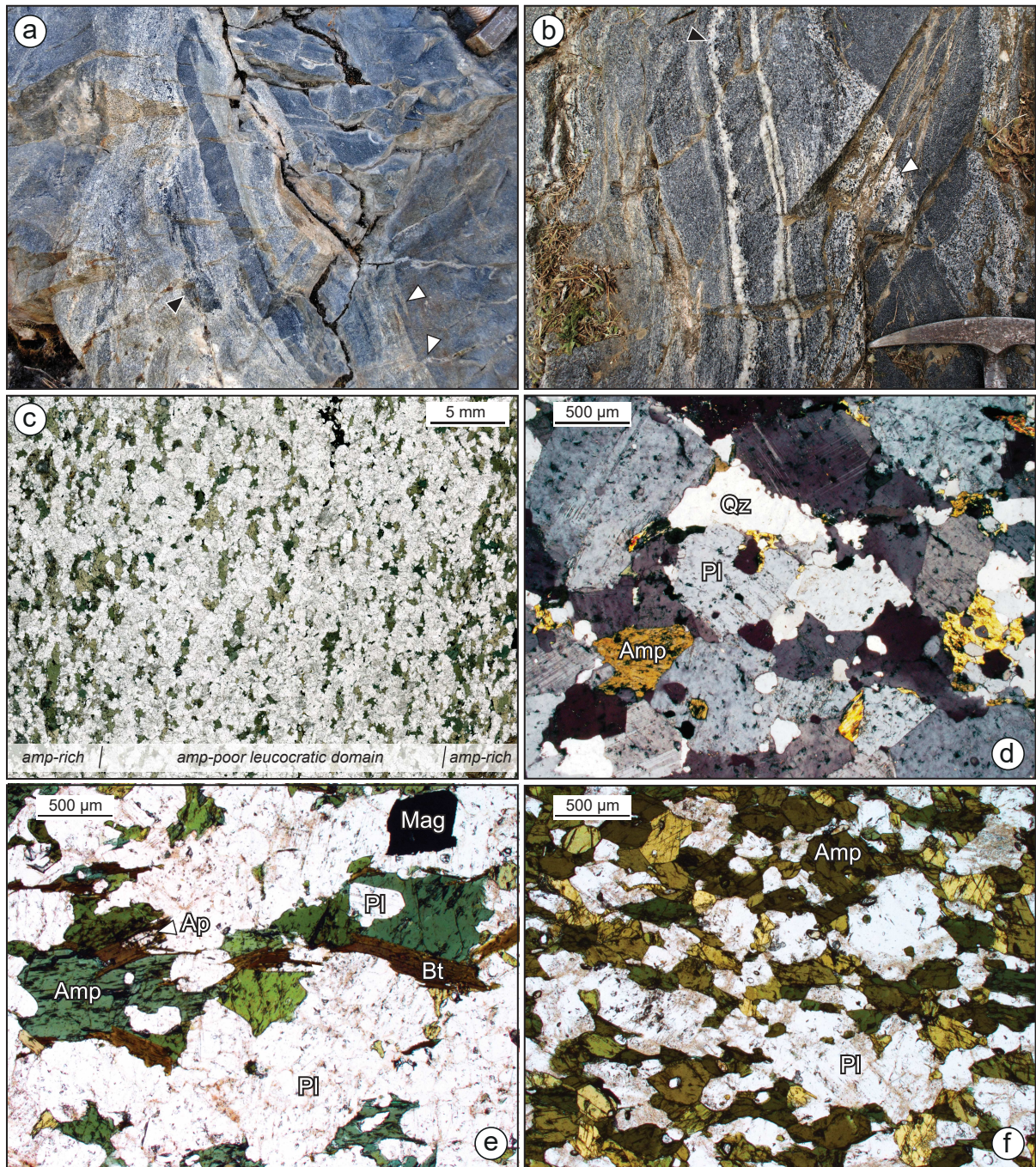
- 960 Naeraa, T., Schersten, A., Rosing, M.T., Kemp, A.I., Hoffmann, J.E., Kokfelt, T.F., Whitehouse, M.J.,
961 2012. Hafnium isotope evidence for a transition in the dynamics of continental growth 3.2
962 Gyr ago. *Nature* 485, 627–30. <https://doi.org/10.1038/nature11140>
- 963 Nandedkar, R.H., Hürlimann, N., Ulmer, P., Müntener, O., 2016. Amphibole–melt trace element
964 partitioning of fractionating calc-alkaline magmas in the lower crust: an experimental study.
965 *Contrib Mineral Petrol* 171, 71. <https://doi.org/10.1007/s00410-016-1278-0>
- 966 Ohta, T., Arai, H., 2007. Statistical empirical index of chemical weathering in igneous rocks: A new
967 tool for evaluating the degree of weathering. *Chemical Geology* 240, 280–297.
968 <https://doi.org/10.1016/j.chemgeo.2007.02.017>
- 969 Padel, M., Álvaro, J.J., Clausen, S., Guillot, F., Poujol, M., Chichorro, M., Monceret, É., Pereira, M.F.,
970 Vizcaíno, D., 2017. U–Pb laser ablation ICP-MS zircon dating across the Ediacaran–Cambrian
971 transition of the Montagne Noire, southern France. *Comptes Rendus Geoscience*.
972 <https://doi.org/10.1016/j.crte.2016.11.002>
- 973 Paquette, J.-L., Ballèvre, M., Peucat, J.-J., Cornen, G., 2017. From opening to subduction of an oceanic
974 domain constrained by LA-ICP-MS U-Pb zircon dating (Variscan belt, Southern Armorican
975 Massif, France). *Lithos* 294–295, 418–437. <https://doi.org/10.1016/j.lithos.2017.10.005>
- 976 Paris, F., Robardet, M., 1990. Early Palaeozoic palaeobiogeography of the Variscan regions.
977 *Tectonophysics* 177, 193–213.
- 978 Pearce, J.A., 2008. Geochemical fingerprinting of oceanic basalts with applications to ophiolite
979 classification and the search for Archean oceanic crust. *Lithos* 100, 14–48.
980 <https://doi.org/10.1016/j.lithos.2007.06.016>
- 981 Pearce, J.A., Peate, D.W., 1995. Tectonic implications of the composition of volcanic arc magmas.
982 *Annual Review of Earth and Planetary Sciences* 23, 251–285.
- 983 Peterlongo, J.-M., 1958. Les terrains cristallins des Monts du Lyonnais (Massif central français),
984 Annales de la Faculté des Sciences de Clermont.
- 985 Piboule, M., Briand, B., 1985. Geochemistry of eclogites and associated rocks of the southeastern
986 area of the French Massif Central: origin of the protoliths. *Chemical Geology* 50, 189–199.
- 987 Pin, C., 1990. Variscan oceans: Ages, origins and geodynamic implications inferred from geochemical
988 and radiometric data. *Tectonophysics* 177, 215–227.
- 989 Pin, C., Lancelot, J., 1982. U-Pb Dating of an Early Paleozoic Bimodal Magmatism in the French Massif
990 Central and of Its Further Metamorphic Evolution. *Contributions to Mineralogy and Petrology*
991 79, 1–12.
- 992 Pin, C., Liñán, E., Pascual, E., Donaire, T., Valenzuela, A., 2002. Late Neoproterozoic crustal growth in
993 the European Variscides: Nd isotope and geochemical evidence from the Sierra de Córdoba
994 Andesites (Ossa-Morena Zone, Southern Spain). *Tectonophysics, Massifs and Correlations*
995 Across the Cadomo-Avalonian Orogens
- 996 352, 133–151. [https://doi.org/10.1016/S0040-1951\(02\)00193-2](https://doi.org/10.1016/S0040-1951(02)00193-2)
- 997 Pin, C., Marini, F., 1993. Early Ordovician continental break-up in Variscan Europe: Nd-Sr isotope and
998 trace element evidence from bimodal igneous associations of the Southern Massif Central,
999 France. *Lithos* 29, 177–196.
- 1000 Pitra, P., Poujol, M., Van Den Driessche, J., Bretagne, E., Lotout, C., Cogné, N., 2022. Late Variscan
1001 (315 Ma) subduction or deceptive zircon REE patterns and U–Pb dates from migmatite-
1002 hosted eclogites? (Montagne Noire, France). *Journal of Metamorphic Geology* 40, 39–65.
1003 <https://doi.org/10.1111/jmg.12609>
- 1004 Pouclet, A., Álvaro, J.J., Bardintzeff, J.-M., Imaz, A.G., Monceret, E., Vizcaíno, D., 2017. Cambrian–
1005 early Ordovician volcanism across the South Armorican and Occitan domains of the Variscan
1006 Belt in France: Continental break-up and rifting of the northern Gondwana margin.
1007 *Geoscience Frontiers* 8, 25–64. <https://doi.org/10.1016/j.gsf.2016.03.002>
- 1008 Rudnick, R.L., Gao, S., 2003. Composition of the continental crust, in: Rudnick, R.L. (Ed.), *The Crust,*
1009 *Treatise on Geochemistry*. Elsevier-Pergamon, Oxford, pp. 1–64.
- 1010 Samson, S.D., D'Lemos, R.S., Blachert-Toft, J., Vervoort, J., 2003. U–Pb geochronology and Hf–Nd
1011 isotope compositions of the oldest Neoproterozoic crust within the Cadomian orogen: new

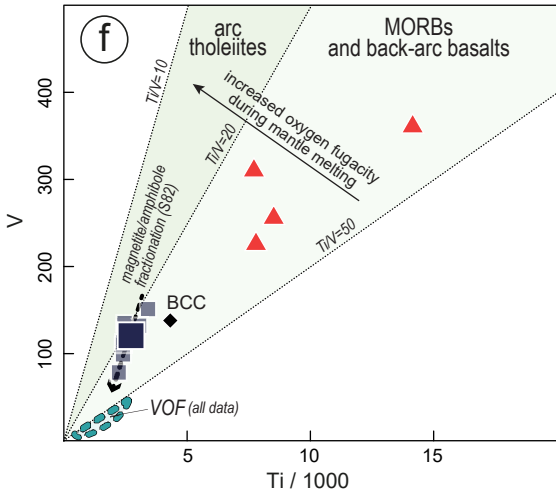
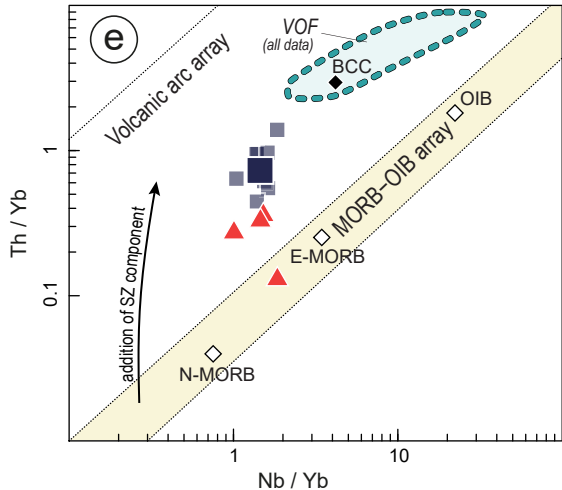
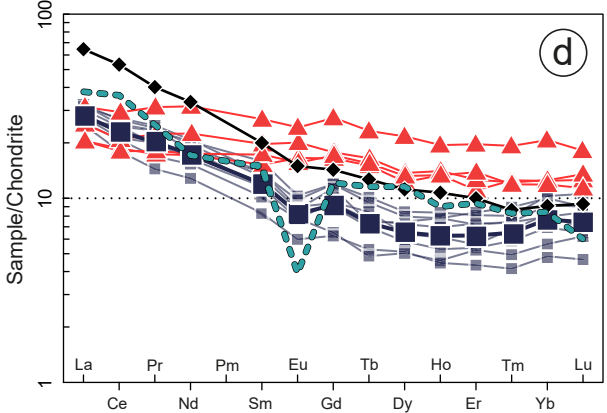
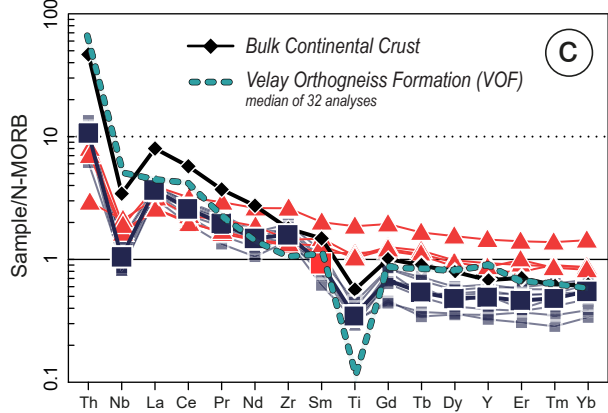
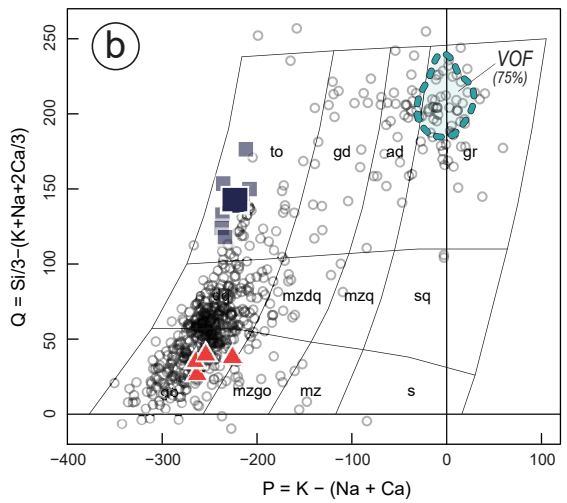
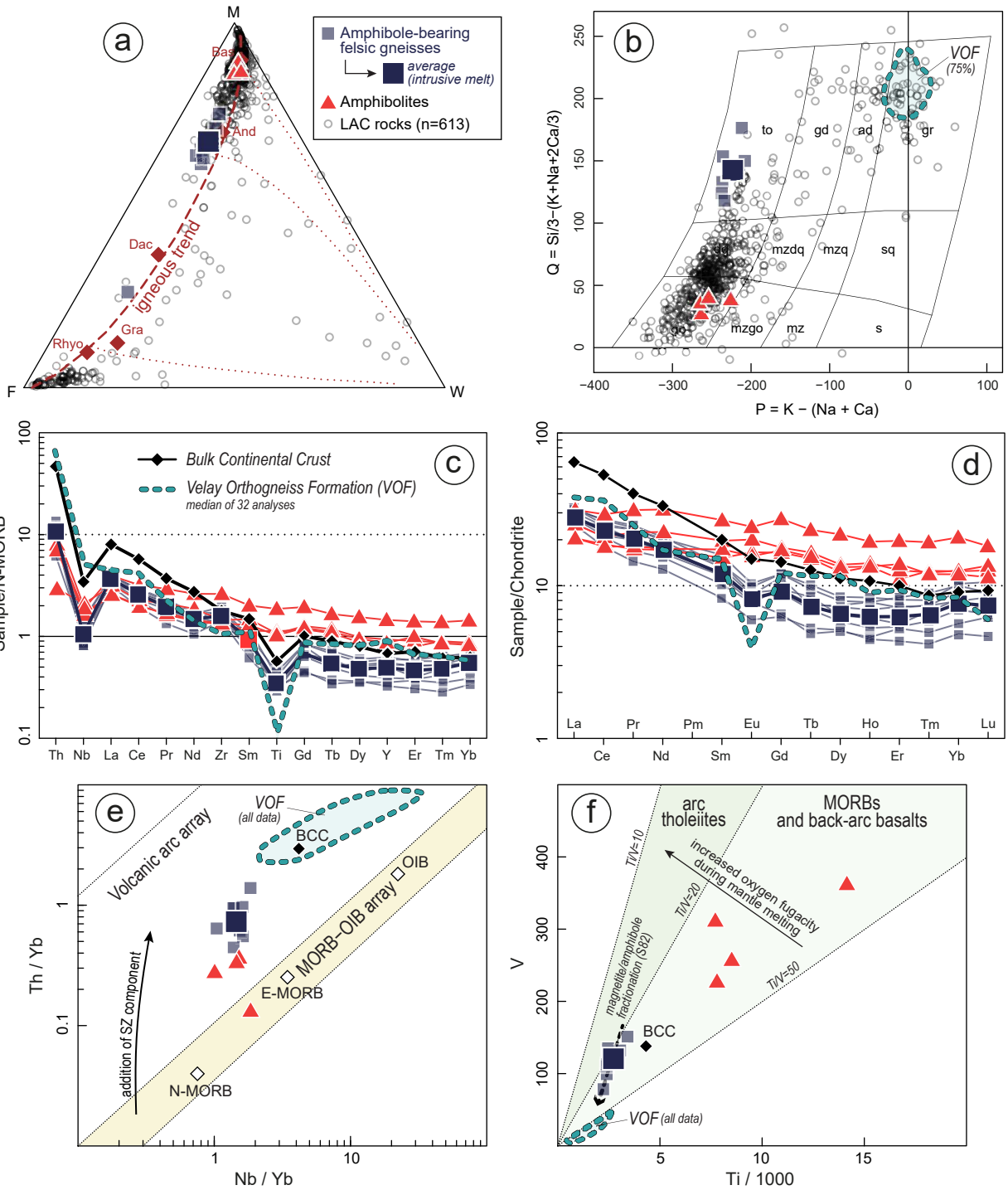
- 1012 evidence for a unique juvenile terrane. *Earth and Planetary Science Letters* 208, 165–180.
1013 [https://doi.org/10.1016/s0012-821x\(03\)00045-1](https://doi.org/10.1016/s0012-821x(03)00045-1)
- 1014 Santallier, D., Briand, B., Ménot, R.P., Piboule, M., 1988. Les complexes leptyno-amphioliques
1015 (C.L.A.) : revue critique et suggestions pour un meilleur emploi de ce terme. *Bulletin de la
1016 Société Géologique de France* 8, 3–12.
- 1017 Schmidt, M.W., Thompson, A.B., 1996. Epidote in calcalkaline magmas; an experimental study of
1018 stability, phase relationships, and the role of epidote in magmatic evolution. *American
1019 Mineralogist* 81, 462–474. <https://doi.org/10.2138/am-1996-3-420>
- 1020 Schneider, J., Corsini, M., Reverso-Peila, A., Lardeaux, J.M., 2014. Thermal and mechanical evolution
1021 of an orogenic wedge during Variscan collision: an example in the Maures-Tanneron Massif
1022 (SE France). *Geological Society, London, Special Publications* 405, 313–331.
1023 <https://doi.org/10.1144/sp405.4>
- 1024 Schulmann, K., Edel, J.-B., Martínez Catalán, J.R., Mazur, S., Guy, A., Lardeaux, J.-M., Ayarza, P.,
1025 Palomeras, I., 2022. Tectonic evolution and global crustal architecture of the European
1026 Variscan belt constrained by geophysical data. *Earth-Science Reviews* 234, 104195.
1027 <https://doi.org/10.1016/j.earscirev.2022.104195>
- 1028 Shervais, J.W., 1982. Ti–V plots and the petrogenesis of modern and ophiolitic lavas. *Earth and
1029 Planetary Science Letters* 59, 101–118.
- 1030 Soejono, I., Janoušek, V., Žáčková, E., Sláma, J., Konopásek, J., Machek, M., Hanzl, P., 2017. Long-
1031 lasting Cadomian magmatic activity along an active northern Gondwana margin: U–Pb zircon
1032 and Sr–Nd isotopic evidence from the Brunovistulian Domain, eastern Bohemian Massif. *Int J
1033 Earth Sci (Geol Rundsch)* 106, 2109–2129. <https://doi.org/10.1007/s00531-016-1416-y>
- 1034 Stampfli, G.M., Hochard, C., Vérard, C., Wilhem, C., vonRaumer, J., 2013. The formation of Pangea.
1035 *Tectonophysics* 593, 1–19. <https://doi.org/10.1016/j.tecto.2013.02.037>
- 1036 Stern, R.J., Bloomer, S.H., Martinez, F., Yamazaki, T., Harrison, T.M., 1996. The composition of back-
1037 arc basin lower crust and upper mantle in the Mariana Trough: A first report. *Island Arc* 5,
1038 354–372. <https://doi.org/10.1111/j.1440-1738.1996.tb00036.x>
- 1039 Sun, S. s, McDonough, W.F., 1989. Chemical and isotopic systematics of oceanic basalts: implications
1040 for mantle composition and processes. *Geological Society, London, Special Publications* 42,
1041 313–345. <https://doi.org/10.1144/gsl.sp.1989.042.01.19>
- 1042 Tabaud, A.S., Lardeaux, J.M., Corsini, M., 2023. A vestige of an Ediacaran magmatic arc in southeast
1043 France and its significance for the northern Gondwana margin. *Int J Earth Sci (Geol Rundsch)*
1044 112, 925–950. <https://doi.org/10.1007/s00531-022-02277-z>
- 1045 Tabaud, A.S., Štípká, P., Mazur, S., Schulmann, K., Míková, J., Wong, J., Sun, M., 2021. Evolution of a
1046 Cambro-Ordovician active margin in northern Gondwana: Geochemical and zircon
1047 geochronological evidence from the Góry Sowie metasedimentary rocks, Poland. *Gondwana
1048 Research* 90, 1–26. <https://doi.org/10.1016/j.gr.2020.10.011>
- 1049 Van der Voo, R., Briden, J.C., Duff, A., 1980. Late Precambrian and Palaeozoic palaeomagnetism of
1050 the Atlantic-bordering continents, in: *Géologie de l’Europe, Mémoires Du BRGM*. pp. 203–
1051 212.
- 1052 Vanderhaeghe, O., Laurent, O., Gardien, V., Moyen, J.-F., Gébelin, A., Chelle-Michou, C., Couzinié, S.,
1053 Villaros, A., Bellanger, M., 2020. Flow of partially molten crust controlling construction,
1054 growth and collapse of the Variscan orogenic belt: the geologic record of the French Massif
1055 Central. *BSGF*. <https://doi.org/10.1051/bsgf/2020013>
- 1056 Vermeesch, P., 2018. IsoplotR: A free and open toolbox for geochronology. *Geoscience Frontiers* 9,
1057 1479–1493. <https://doi.org/10.1016/j.gsf.2018.04.001>
- 1058 Whitney, D.L., Hamelin, C., Teyssier, C., Raia, N.H., Korchinski, M.S., Seaton, N.C.A., Bagley, B.C., von
1059 der Handt, A., Roger, F., Rey, P.F., 2020. Deep crustal source of gneiss dome revealed by
1060 eclogite in migmatite (Montagne Noire, French Massif Central). *Journal of Metamorphic
1061 Geology* 38, 297–327. <https://doi.org/10.1111/jmg.12523>

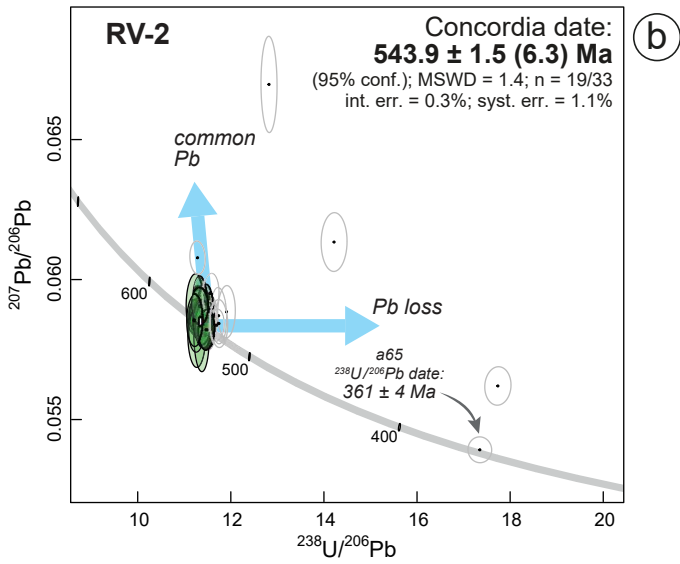
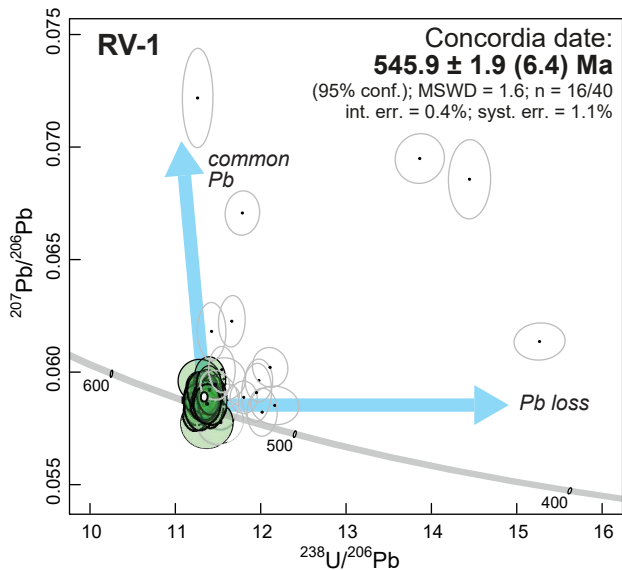
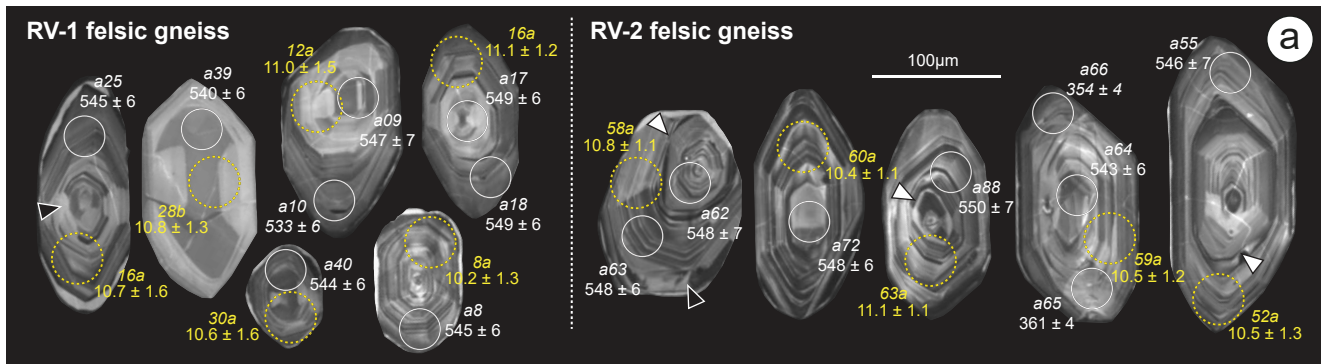
1062 Zeh, A., Gerdes, A., 2010. Baltica- and Gondwana-derived sediments in the Mid-German Crystalline
1063 Rise (Central Europe): Implications for the closure of the Rheic ocean. *Gondwana Research*
1064 17, 254–263. <https://doi.org/10.1016/j.gr.2009.08.004>
1065
1066

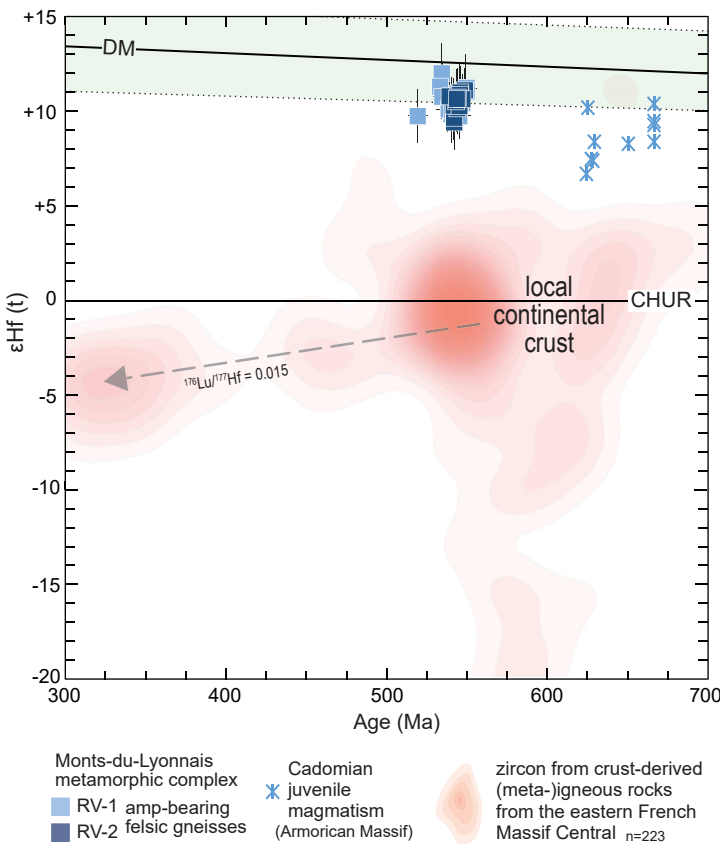


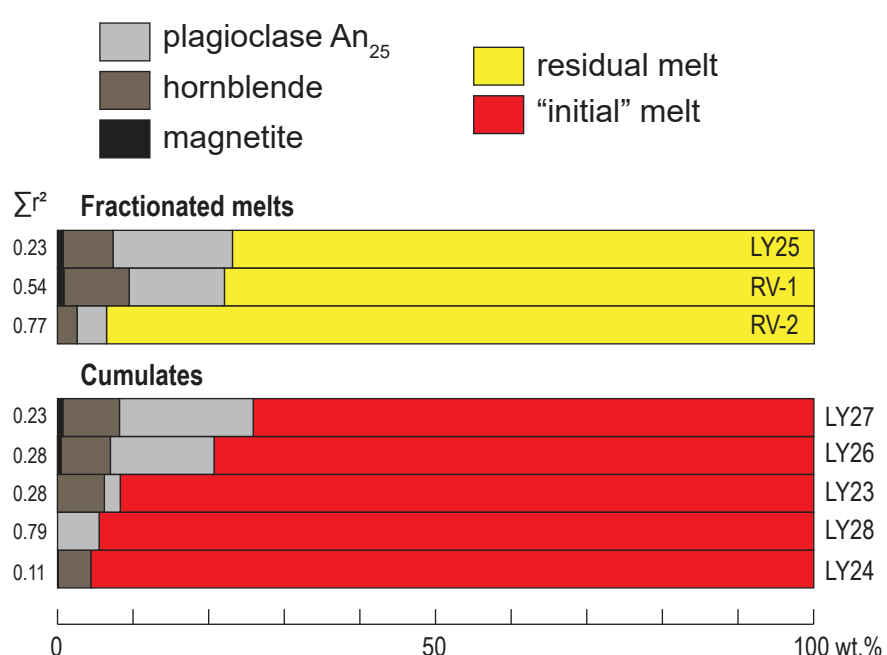


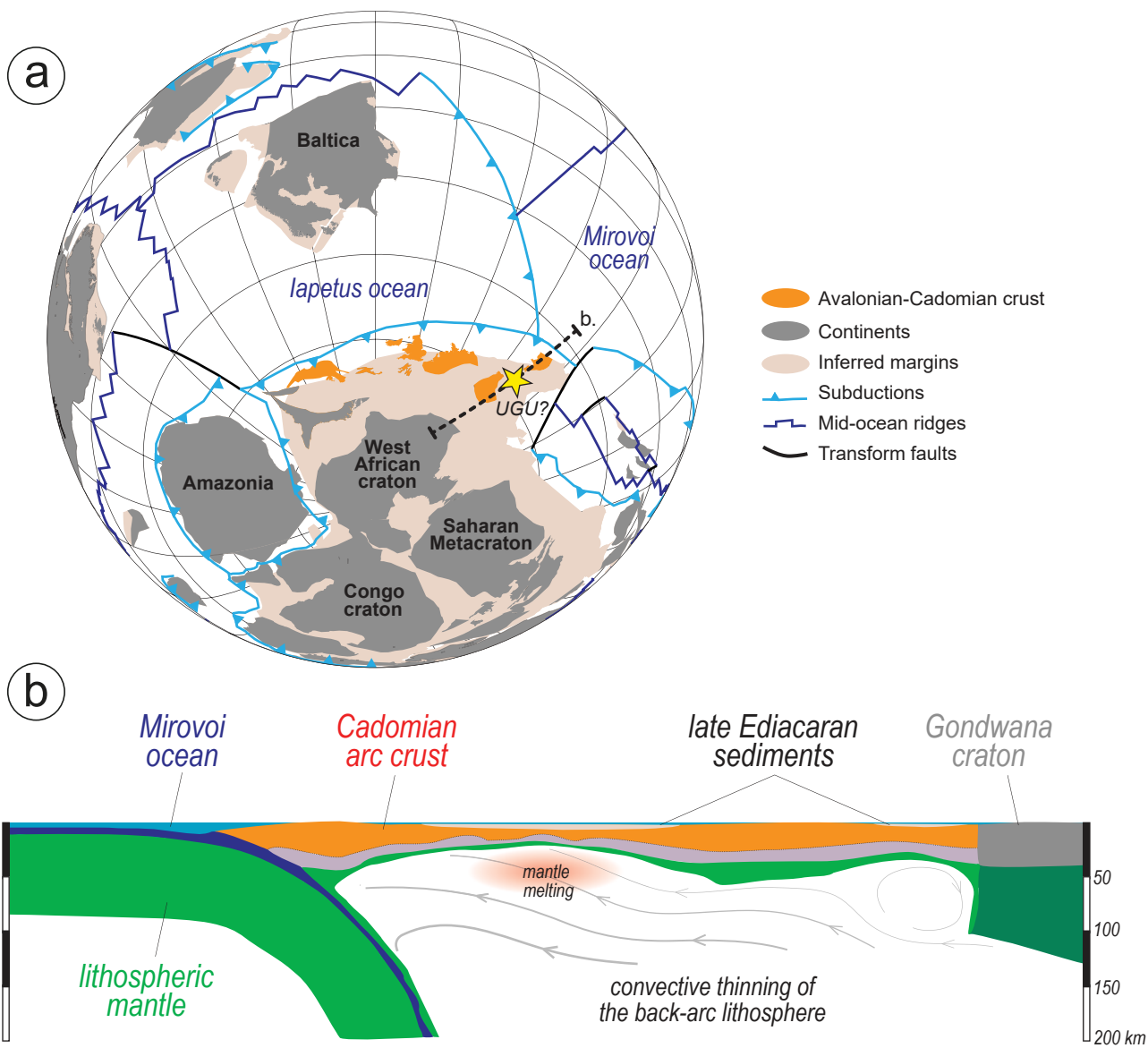


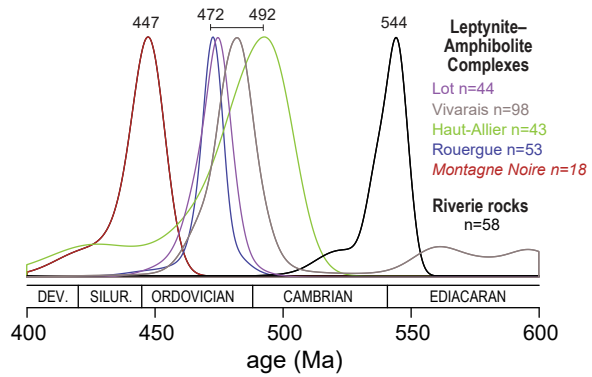












Supplementary text of the manuscript:

Late Ediacaran juvenile magmatism in the Variscan Monts-du-Lyonnais

metamorphic complex (Massif Central, France)

Identification d'un magmatisme juvénile fini-édiacarien dans le complexe métamorphique varisque des Monts-du-Lyonnais (Massif Central, France)

Simon Couzinié^{1,2,3*}, Oscar Laurent⁴, Pierre Bouilhol¹, Cyril Chelle-Michou⁵, Anne-Céline Ganzhorn^{3**}, Véronique Gardien³, Jean-François Moyen⁶

¹Université de Lorraine, CNRS, CRPG, 54000 Nancy, France

²Université Jean Monnet, CNRS, LGL-TPE UMR5276, F-42023 Saint-Etienne, France

³LGL-TPE UMR 5276, CNRS, Université Lyon 1, ENS de Lyon, 69622 Villeurbanne, France

⁴CNRS, Géosciences Environnement Toulouse, Observatoire Midi-Pyrénées, 14 avenue Edouard Belin, 31400 Toulouse, France

⁵Institute of Geochemistry and Petrology, ETH Zürich, CH-8092 Zürich, Switzerland

⁶Université Jean-Monnet, Laboratoire Magmas et Volcans, UCA-CNRS-IRD, Aubière, France

*Corresponding author. simon.couzinie@univ-lorraine.fr

**Present address: Saint-Gobain Recherche, Aubervilliers, France

1. Analytical procedures

A. Whole-rock major and trace element compositions

Samples were sawed at Saint-Etienne University and a c. 500 g fragment of each sample was sent to ALS Global for whole-rock chemical composition measurements. We chose the "Complete Characterization Package" which combines ICP–AES and ICP–MS analyses for major and trace elements, respectively. More information about analytical routines used by this company can be found at <http://www.alsglobal.com/>. Repeated analyses of standards SY-4, GRE-3, OREAS-121 and AMIS0304 were realized during the analytical session. Analyses of the standards were reproducible to <1.7% for most major elements except K₂O (2.4%), MgO (6.4%) and P₂O₅ (4.6%); <7.9% for trace elements except Cr (25%), V (12.5%) and Ba (10.9%); and consistent within uncertainty with the expected values. Duplicate measurements of four samples show external reproducibility better than 1.1% (RSD) for major elements (except P₂O₅ at 4.6%) and generally better than 5.4% (RSD) for trace elements except for Ti, Tm, Lu, Hf and V. Fifteen blanks display measured values typically under detection limits for all major and trace elements.

B. Zircon U–Pb dating

Zircon U–Pb isotopic analyses were carried out at Goethe Universität Frankfrut (GUF) by laser ablation using a Resolution M-50 (Resonetics) 193 nm ArF excimer laser system attached to ThermoFinnigan Element 2 sector field ICP–MS. We applied the same methods as in Zeh and Gerdes (2012). We used a repetition rate of 5.5 Hz, and a laser spot-size of 30 µm for measurements of unknowns and zircon reference materials GJ-1, Plešovice and BB-16. The on-sample fluence was ~2.5 to 3 J.cm⁻². Sample surface was cleaned directly before each analysis by three pre-ablation pulses. Ablation was performed in a two-volume ablation cell (Laurin Technic, Australia) characterized by a very quick response time (<1 s until maximum signal strength is reached) and wash-out delay (<3 s to get <1% of maximum signal intensity). It was fluxed during ablation with carrier gas consisting of a ~0.6 L.min⁻¹ He stream, mixed directly after the ablation cell with make-up gas consisting of ~0.07 L.min⁻¹ N₂ and 0.68 L.min⁻¹ Ar prior introduction into the plasma of the sector field ICP–MS. All gases had a purity of 99.999% and no homogenizer was used while mixing the gases, to prevent smoothing of the signal and thus to be able to detect significant variations of the ²⁰⁷Pb/²⁰⁶Pb and ²³⁸U/²⁰⁶Pb ratios during measurements, possibly revealing the sequential sampling of different age domains within single zircon grains. Signal was tuned for maximum sensitivity for Pb and U while keeping low the production of oxides (²⁵⁴UO/²³⁸U ≤ 0.5%). The obtained sensitivity on zircon standard GJ-1 for ²³⁸U and a 30 µm spot size is close to 10000 cps.ppm⁻¹ at 5.5 Hz and 3 J.cm⁻². Data were acquired using time resolved-peak jumping, the detector being set to analogue mode for ²³²Th and ²³⁸U and counting mode for ²⁰⁴(Hg+Pb), ²⁰⁶Pb, ²⁰⁷Pb and ²⁰⁸Pb. A total of 356 mass scans were acquired over ~41 s measurement (20 s of background measurement followed by 21 s of sample ablation) and integrated to 89 ratios (4 mass scans per

integration, time resolution = 0.46 s). Those ratios were subsequently corrected offline for background signal, common Pb, instrumental mass discrimination and Pb/U fractionation (both laser-induced during individual measurements, and over the day) using an in-house MS Excel® spreadsheet. No common Pb correction was performed. The inter-elemental fractionation $^{206}\text{Pb}/^{238}\text{U}$ during the 21 s of sample ablation was corrected for each analysis by applying a linear regression through all measured ratios, excluding the outliers ($\pm 2\sigma$), and considering that the intercept with the y-axis represents the "true" ratio. Elemental fractionation over the analytical session, as well as instrumental mass discrimination, were corrected by normalization to the $^{206}\text{Pb}/^{238}\text{U}$ (0.0982) and $^{207}\text{Pb}/^{206}\text{Pb}$ (0.061) ratios of reference zircon GJ-1 (Jackson et al., 2004) using standard bracketing. Elemental concentrations in U and Pb were calculated using raw signal (in cps) of ^{238}U and ^{206}Pb for each spot, corrected from the analytical drift over the session (monitored using GJ-1) and normalized to the recommended values of the GJ-1 zircon standard (U = 280.1 ppm; Pb = 25.5 ppm). Th/U ratio was determined for each spot using the mass fractionation-corrected $^{232}\text{Th}/^{238}\text{U}$ ratio, normalized to the recommended value of the GJ-1 zircon standard (Th/U = 0.0296).

The quoted uncertainties for each individual analysis are (i) for the $^{206}\text{Pb}/^{238}\text{U}$ ratio, the quadratic addition of the within-run precision (2σ) with the external reproducibility of standard zircon GJ-1 during the corresponding analytical session (0.5 to 1.5%, 2σ); and (ii) for the $^{207}\text{Pb}/^{206}\text{Pb}$ ratio, a ^{207}Pb signal-dependent uncertainty propagation, as described by Gerdes and Zeh (2009). The $^{207}\text{Pb}/^{235}\text{U}$ ratio was calculated using the $^{206}\text{Pb}/^{238}\text{U}$ and $^{207}\text{Pb}/^{206}\text{Pb}$ ratios and assuming a natural $^{238}\text{U}/^{235}\text{U}$ of 137.818, and its uncertainty was obtained by quadratic addition of propagated errors on both ratios. Age calculations and data plotting were performed using IsoplotR (Vermeesch, 2018).

Data from secondary standards were processed as unknowns to check the accuracy of the corrections (Fig. S1) and the results reported Supplementary Table S3. Calculated pooled dates are within error of the recommended TIMS values for Plešovice and BB-16, i.e. 337.13 ± 0.37 Ma and 560 ± 0.8 Ma, respectively (Santos et al., 2017; Sláma et al., 2008). The dataset for the Riverie samples is presented in Supplementary Table S4.

Additional systematic errors were propagated to every U–Pb Concordia date calculated out of several individual analyses following the scheme of Horstwood et al., (2016). Those include the uncertainties on: (i) the decay constants for ^{238}U and ^{235}U , set at 0.107% and 0.136% for ^{238}U and ^{235}U , respectively (Jaffey et al., 1971); (ii) the isotope ratios of the primary standard (GJ-1), set at 0.5%; (iii) the overall reproducibility of the method, estimated based on the long-term excess scatter of secondary zircon reference materials, i.e. 1% relative. Error propagation involved the quadratic addition of the "internal" error calculated by IsoplotR and the other systematic errors listed above.

A summary of analytical operating conditions is provided in Supplementary Table ST0 (see below).

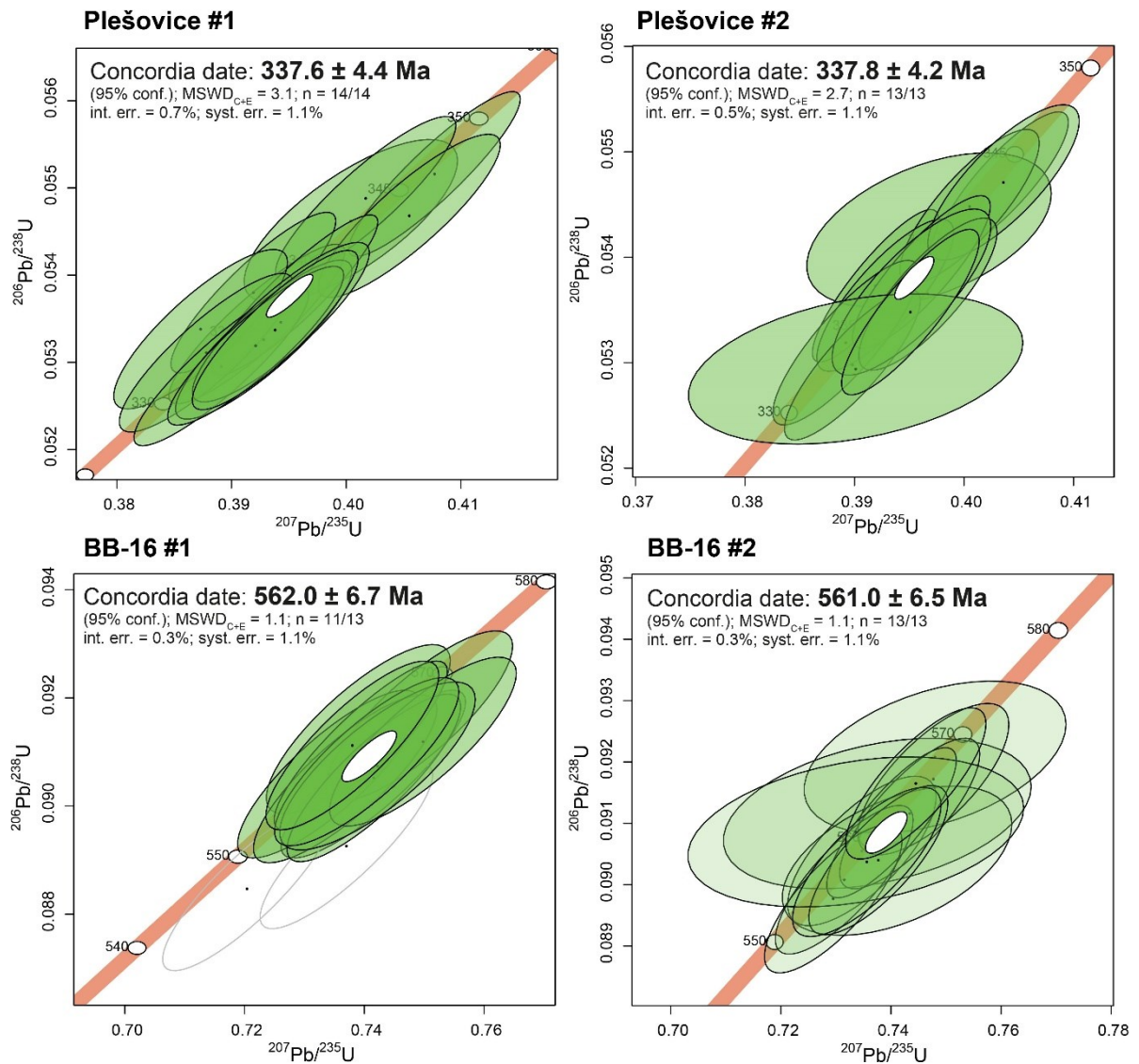


Figure S1: Wetherill diagrams ($^{206}\text{Pb}/^{238}\text{U}$ vs. $^{207}\text{Pb}/^{235}\text{U}$) for secondary zircon standards Plešovice and BB-16 analysed during the two analytical sessions at GUF. Error ellipses are displayed at 2σ level of uncertainty. Green ellipses are those considered for pooled date calculations.

Sample Preparation	
Laboratory name	University of Saint-Etienne (FR) and University of Stellenbosch (RSA)
Sample type/mineral	Zircon
Sample preparation	Conventional techniques (sieving, panning, magnetic and heavy liquids separation followed by handpicking). Grains cast into epoxy mounts.
Imaging	BSE and CL-imaging performed at the Central Analytical Facility of Stellenbosch University using a Zeiss MERLIN Scanning Electron Microscope
Laser ablation system	
Laboratory name	Goethe Universität Frankfurt, Germany
Make, Model & type	RESolution M-50 (Resonetics) ArF-excimer
Ablation cell	Two-volume ablation cell (Laurin Technic, Australia)
Laser wavelength	193 nm
Pulse width	~ 25 ns
Fluence	2.5 – 3 J/cm ²
Repetition rate	5.5 Hz
Spot diameter	30 µm
Ablation duration	21 seconds
Sampling mode	Static single spot
Carrier gas	100% He mixed directly after the ablation cell with make-up gas consisting of
Carrier gas flow (He)	0.6 L/min
ICP-MS Instrument	
Make, Model & type	ThermoFinnigan Element 2 sector field ICP-MS
Sample introduction	Ablation aerosol
Make-up gas flow	~0.07 L·min ⁻¹ N ₂ and 0.68 L·min ⁻¹ Ar
Detection system	Secondary Electron Multiplier with dual detector mode (pulse counting and analog, cross calibrated daily with ²³⁸ U measured on analog mode only)
Masses measured	²⁰⁴ (Hg + Pb), ²⁰⁶ Pb, ²⁰⁷ Pb, ²⁰⁸ Pb, ²³² Th, ²³⁸ U
Integration time per peak	10 ms except at amu 206 and 207 (20 ms)
Total integration time per output data point (s)	108 ms
Sensitivity/Efficiency	10000 cps.ppm ⁻¹ for ²³⁸ U on GJ-1
Data processing	
Gas blank	20 seconds on-peak
Calibration strategy	GJ-1 zircon standard used as primary reference material, Plešovice and BB-16 used as secondary reference material (quality control)
Common-Pb correction, composition and uncertainty	No common-Pb correction
Reference Material info	GJ1 (Jackson et al., 2004), Plešovice (Sláma et al., 2008), BB-16 (Santos et al., 2017)
Data processing package	in-house MS Excel® spreadsheet
Uncertainty level and propagation	Ages are quoted at 95% conf. level; propagation of systematic uncertainties by quadratic addition according to Horstwood et al. (2016)
Quality control/validation	Plešovice: Concordia age: 337.6 ± 4.4 Ma (n = 14/14 MSWD = 3.1) and 337.8 ± 4.2 Ma (n = 13/13 MSWD = 2.7); accepted value: 337.1 ± 0.4 Ma (Sláma et al., 2008) BB-16: Concordia age: 562.0 ± 6.7 Ma (n = 11/13 MSWD = 1.1) and 361.0 ± 6.5 Ma (n = 13/13 MSWD = 1.1); accepted value: 560.0 ± 0.8 Ma (Santos et al., 2017)

Supplementary Table ST0: Summary of operating conditions for zircon LA-ICP-MS dating.

C. Zircon Lu–Hf isotope measurements

Measurements were performed at GUF using a Thermo-Finnigan Neptune multicollector ICP-MS attached to a Resolution M-50193 nm Ar-F excimer laser ablation system, equipped with a two-volume Laurin Technic ablation cell. Laser spots with diameters of 40 or 60 µm were drilled “on top” of the existing spots already analyzed for U–Pb dating or in the same domain as identified based on CL images, with repetition rates of 4 Hz and an energy density of 5 to 6 J·cm⁻². He was used as a carrier gas (~0.6 L·min⁻¹) and make-up gas consisting of high-purity Ar (~0.75 L·min⁻¹)

and N₂ ($\sim 0.07 \text{ L}\cdot\text{min}^{-1}$) was admixed to the carrier gas to improve sensitivity. Post-ablation homogenization is performed by fluxing the gases through a Resolution Instruments Squid® tubing. Data were acquired using multi-collector static mode, during 58 s of measurement characterized by 1.052 s integration time (55 baseline-corrected ratios). ¹⁷²Yb, ¹⁷³Yb and ¹⁷⁵Lu masses were monitored to allow the correction of isobaric interferences (¹⁷⁶Yb and ¹⁷⁶Lu on ¹⁷⁶Hf). Instrumental mass bias for Yb isotopes (calculation of β^{Yb}) was monitored for each measurement using an exponential law and corrected to the natural ratio $^{172}\text{Yb}/^{173}\text{Yb}=1.35351$. Mass fractionation of Lu isotopes was assumed identical to that of Yb isotopes ($\beta_{\text{Lu}}=\beta_{\text{Yb}}$). The isobaric interferences were subsequently corrected to mass bias-corrected $^{176}\text{Yb}/^{173}\text{Yb} = 0.79502$ and $^{176}\text{Lu}/^{175}\text{Lu} = 0.02656$ (see Gerdes and Zeh, 2006). Mass bias for Hf isotopes (β_{Hf}) was determined using an exponential law and normalized to $^{179}\text{Hf}/^{177}\text{Hf}=0.7325$. Accuracy and external reproducibility of the method were controlled by repeated analyses of reference zircon standards GJ-1 (Jackson et al., 2004; Morel et al., 2008), Plešovice (Sláma et al., 2008), and Temora (Woodhead et al., 2004). Results for standards are presented in the Supplementary Table S5 and for samples in the Supplementary Table S6.

The quoted uncertainties on $^{176}\text{Hf}/^{177}\text{Hf}$ ratios and $\epsilon_{\text{Hf}}(t)$ are quadratic additions of within-run precision of each measurement with the external reproducibility (2 S.D.) of the reference zircon standard GJ-1 (~ 70 ppm). Data reduction was carried out using an in-house MS Excel© spreadsheet (Gerdes and Zeh, 2009, 2006).

Calculation of initial $^{176}\text{Hf}/^{177}\text{Hf}$ ratios was performed using the individual $^{176}\text{Lu}/^{177}\text{Hf}$ ratio of each measurement, a decay constant of $\lambda_{176\text{Lu}} = 1.867 \times 10^{-11}$ (Scherer et al., 2001; Söderlund et al., 2004) and the emplacement age obtained by U–Pb zircon dating. For the calculation of the $\epsilon_{\text{Hf}}(t)$, parameters of the chondritic uniform reservoir (CHUR) recommended by Bouvier et al. (2008) were used ($^{176}\text{Lu}/^{177}\text{Hf} = 0.0336$; $^{176}\text{Hf}/^{177}\text{Hf} = 0.282785$).

2. Data compilation

The data used in Figure 4 were compiled from Blanc, 1981; Bodinier, 1983; Briand et al., 1991, 1988; Brousse et al., 1990; Brousse and Varet, 1972; Cabanis et al., 1983; Chelle-Michou et al., 2017; Chenevoy et al., 1998; Coffrant and Piboule, 1971; Collomb, 1970; Davoine, 1969; Demange, 1985; Downes et al., 1989; Downes and Duthou, 1988; Dufour, 1982; Forestier, 1961; Giraud et al., 1984; Lasnier, 1977; Ouali, 1993; Paquette et al., 1995; Piboule, 1977; Piboule and Briand, 1985; Pin and Marini, 1993; Ravier and Chenevoy, 1979; Thiéblemont, 1990; Whitney et al., 2020.

References

- Blanc, D., 1981. Les roches basiques et ultrabasiques des Monts du Lyonnais. Etude pétrographique, minéralogique et géochimique (PhD thesis).
- Bodinier, J.L., 1983. Etude géochimique du massif basique et ultrabasique de Najac (Aveyron). Conséquences géotectoniques. Bulletin de la Société Géologique de France 25, 185–193.
- Bouvier, A., Vervoort, J.D., Patchett, P.J., 2008. The Lu–Hf and Sm–Nd isotopic composition of CHUR: Constraints from unequilibrated chondrites and implications for the bulk composition of terrestrial planets. Earth and Planetary Science Letters 273, 48–57. <https://doi.org/10.1016/j.epsl.2008.06.010>
- Briand, B., Piboule, M., Bouchardon, J.-L., 1988. Diversité géochimique des métabasites des groupes leptyno-amphiboliques du Rouergue et de Marvejols (Massif central). Origine et implications. Bulletin de la Société Géologique de France 4, 489–498.
- Briand, B., Piboule, M., Santallier, D., Bouchardon, J.-L., 1991. Geochemistry and tectonic implications of two Ordovician bimodal igneous complexes, southern French Massif Central. Journal of the Geological Society, London 148, 959–971.
- Brousse, P., Rançon, J.P., Le Garrec, M.J., Tempier, P., Suire, J., BVeyret-Mekdjian, Y., D'Arcy, D., Périchaud, J.J., 1990. Notice explicative, Carte géol. France (1/50 000), feuille La Tour-d'Auvergne (740). BRGM, Orléans, p. 68.
- Brousse, R., Varet, J., 1972. Notice explicative, Carte géol. France (1/50 000), feuille Riom-ès-Montagnes (764). BRGM, Orléans, p. 42.
- Cabanis, B., Guillot, P.-L., Santallier, D., Jaffrezic, H., Meyer, G., Treuil, M., 1983. Trace-elements in the basic rocks within the metamorphic series of the South-Limousin (French Central Massif, France). Bulletin de la Société Géologique de France 25, 563–574.
- Chelle-Michou, C., Laurent, O., Moyen, J.-F., Block, S., Paquette, J.-L., Couzinié, S., Gardien, V., Vanderhaeghe, O., Villaros, A., Zeh, A., 2017. Pre-Cadomian to late-Variscan odyssey of the eastern Massif Central, France: Formation of the West European crust in a nutshell. Gondwana Research 46, 170–190. <https://doi.org/10.1016/j.gr.2017.02.010>
- Chenevoy, M., Ledru, P., Feybesse, J.-L., Jauffret, D., Etlicher, B., 1998. Notice explicative, Carte géol. France (1/50 000), feuille Annonay (769). BRGM, Orléans, p. 83.
- Coffrant, D., Piboule, M., 1971. Les éclogites et roches associées des massifs basiques de Saint-Joseph (monts du Lyonnais, Massif central français). Bulletin de la Société Géologique de France 13, 283–291.
- Collomb, P., 1970. Etude géologique du Rouergue cristallin.
- Davoine, P., 1969. La distinction géochimique ortho-para des leptynites. Bulletin de la Société Française de Minéralogie et de Cristallographie 92, 59–75.
- Demange, M., 1985. The eclogite-facies rocks of the Montagne Noire, France. Chemical Geology 50, 173–188.
- Downes, H., Bodinier, J.L., Dupuy, C., Leyreloup, A.F., Dostal, J., 1989. Isotope and trace-element heterogeneities in high-grade basic metamorphic rocks of Marvejols: Tectonic implications for the Hercynian suture zone of the French Massif Central. Lithos 24, 37–54.
- Downes, H., Duthou, J.-L., 1988. Isotopic and trace-element arguments for the lower-crustal origin of hercynian granitoids and pre-hercynian orthogneisses, Massif Central (France). Chemical Geology 68, 291–308.
- Dufour, E., 1982. Pétrologie et géochimie des formations orthométamorphiques acides des Monts du Lyonnais (Massif central, France) (PhD thesis).
- Forestier, F.-H., 1961. Métamorphisme hercynien et antéhercynien dans le bassin du haut-Allier (Massif Central français). Bulletin du service de la carte géologique de France 271.
- Gerdes, A., Zeh, A., 2009. Zircon formation versus zircon alteration — New insights from combined U–Pb and Lu–Hf in-situ LA-ICP-MS analyses, and consequences for the

- interpretation of Archean zircon from the Central Zone of the Limpopo Belt. *Chemical Geology* 261, 230–243. <https://doi.org/10.1016/j.chemgeo.2008.03.005>
- Gerdes, A., Zeh, A., 2006. Combined U–Pb and Hf isotope LA-(MC-)ICP-MS analyses of detrital zircons: Comparison with SHRIMP and new constraints for the provenance and age of an Armorican metasediment in Central Germany. *Earth and Planetary Science Letters* 249, 47–61. <https://doi.org/10.1016/j.epsl.2006.06.039>
- Giraud, A., Marchand, J., Dupuy, C., Dostal, J., 1984. Geochemistry of leptyno-amphibolite complex from Haut Allier (French Massif Central). *Lithos* 17, 203–214.
- Horstwood, M.S.A., Košler, J., Gehrels, G., Jackson, S.E., McLean, N.M., Paton, C., Pearson, N.J., Sircombe, K., Sylvester, P., Vermeesch, P., Bowring, J.F., Condon, D.J., Schoene, B., 2016. Community-Derived Standards for LA-ICP-MS U-(Th-)Pb Geochronology - Uncertainty Propagation, Age Interpretation and Data Reporting. *Geostandards and Geoanalytical Research* 40, 311–332. <https://doi.org/10.1111/j.1751-908X.2016.00379.x>
- Jackson, S.E., Pearson, N.J., Griffin, W.L., Belousova, E.A., 2004. The application of laser ablation-inductively coupled plasma-mass spectrometry to in situ U–Pb zircon geochronology. *Chemical Geology* 211, 47–69. <https://doi.org/10.1016/j.chemgeo.2004.06.017>
- Jaffey, A.H., Flynn, K.F., Glendenin, L.E., Bentley, W.C., Essling, A.M., 1971. Precision measurement of half-lives and specific activities of ^{235}U and ^{238}U . *Phys. Rev. C* 4, 1889–1906. <https://doi.org/10.1103/PhysRevC.4.1889>
- Lasnier, B., 1977. Persistance d'une série granulitique au coeur du Massif Central français, Haut-Allier : les termes basiques, ultrabasiques et carbonatés (Thesis).
- Morel, M.L.A., Nebel, O., Nebel-Jacobsen, Y.J., Miller, J.S., Vroon, P.Z., 2008. Hafnium isotope characterization of the GJ-1 zircon reference material by solution and laser-ablation MC-ICPMS. *Chemical Geology* 255, 231–235. <https://doi.org/10.1016/j.chemgeo.2008.06.040>
- Ouali, H., 1993. Caractérisation géochimique des paléomagmatites de quelques unités lithotectoniques du Massif Central français : Implications géodynamiques (PhD thesis).
- Paquette, J.L., Monchoux, P., Couturier, M., 1995. Geochemical and isotopic study of a norite-eclogite transition in the European Variscan belt: Implications for U-Pb zircon systematics in metabasic rocks. *Geochimica et Cosmochimica Acta* 59, 1611–1622.
- Piboule, M., 1977. Utilisation de l'analyse factorielle discriminante pour la reconnaissance de la nature des magmas parents des amphibolites. Application à quelques métabasites du Rouergue et du Limousin (Massif Central français). *Bulletin de la Société Géologique de France* 19, 1133–1143.
- Piboule, M., Briand, B., 1985. Geochemistry of eclogites and associated rocks of the southeastern area of the French Massif Central: origin of the protoliths. *Chemical Geology* 50, 189–199.
- Pin, C., Marini, F., 1993. Early Ordovician continental break-up in Variscan Europe: Nd-Sr isotope and trace element evidence from bimodal igneous associations of the Southern Massif Central, France. *Lithos* 29, 177–196.
- Ravier, J., Chenevoy, M., 1979. Présence de formations granulitiques jalonnant un linéament crustal dans la série cristallophylienne de la Sioule (Massif Central français). *Comptes Rendus de l'Académie des Sciences, Paris* 288, 1703–1706.
- Santos, M., Lana, C., Scholz, R., Buick, I., Schmitz, M., Kamo, S., Gerdes, A., Corfu, F., Tapster, S., Lancaster, P., Storey, C., Basei, M., Tohver, E., Alkmim, A., Nalini Jr, H., Krambrock, K., Fantini, C., Wiedenbeck, M., 2017. A New Appraisal of Sri Lankan BB Zircon as a Reference Material for LA-ICP-MS U-Pb Geochronology and Lu-Hf Isotope Tracing. *Geostandards and Geoanalytical Research* 41, 335. <https://doi.org/10.1111/ggr.12167>
- Scherer, E.E., Münker, C., Mezger, K., 2001. Calibration of the Lutetium-Hafnium Clock. *Science* 293, 683–687.

- Sláma, J., Košler, J., Condon, D.J., Crowley, J.L., Gerdes, A., Hanchar, J.M., Horstwood, M.S.A., Morris, G.A., Nasdala, L., Norberg, N., Schaltegger, U., Schoene, B., Tubrett, M.N., Whitehouse, M.J., 2008. Plešovice zircon — A new natural reference material for U–Pb and Hf isotopic microanalysis. *Chemical Geology* 249, 1–35.
<https://doi.org/10.1016/j.chemgeo.2007.11.005>
- Söderlund, U., Patchett, P.J., Vervoort, J.D., Isachsen, C.E., 2004. The ^{176}Lu decay constant determined by Lu–Hf and U–Pb isotope systematics of Precambrian mafic intrusions. *Earth and Planetary Science Letters* 219, 311–324.
[https://doi.org/10.1016/s0012-821x\(04\)00012-3](https://doi.org/10.1016/s0012-821x(04)00012-3)
- Thiéblemont, D., 1990. Géochimie des formations paléomagmatiques du segment lyonnais de la chaîne Varisque (socle et série de la Brévenne) (Report).
- Vermeesch, P., 2018. IsoplotR: A free and open toolbox for geochronology. *Geoscience Frontiers* 9, 1479–1493. <https://doi.org/10.1016/j.gsf.2018.04.001>
- Whitney, D.L., Hamelin, C., Teyssier, C., Raia, N.H., Korchinski, M.S., Seaton, N.C.A., Bagley, B.C., von der Handt, A., Roger, F., Rey, P.F., 2020. Deep crustal source of gneiss dome revealed by eclogite in migmatite (Montagne Noire, French Massif Central). *Journal of Metamorphic Geology* 38, 297–327.
<https://doi.org/10.1111/jmg.12523>
- Woodhead, J., Hergt, J., Shelley, M., Eggins, S., Kemp, R., 2004. Zircon Hf-isotope analysis with an excimer laser, depth profiling, ablation of complex geometries, and concomitant age estimation. *Chemical Geology* 209, 121–135.
<https://doi.org/10.1016/j.chemgeo.2004.04.026>
- Zeh, A., Gerdes, A., 2012. U–Pb and Hf isotope record of detrital zircons from gold-bearing sediments of the Pietersburg Greenstone Belt (South Africa)—Is there a common provenance with the Witwatersrand Basin? *Precambrian Research* 204–205, 46–56.
<https://doi.org/10.1016/j.precamres.2012.02.013>

Table S1: Whole-rock major and trace element compositions of samples from the Riverie belt

Analyses performed by ALS Global

Sample	RV-1	RV-2	LY23	LY24	LY25	LY26	LY27	LY28	LY21	LY22	MG05	MG06
Type	felsic gneiss	amphibolite	amphibolite	amphibolite	amphibolite							

Major elements (wt.%), measured by ICP-AES

SiO ₂	68.40	65.50	64.00	64.00	67.70	63.00	62.60	64.80	48.00	46.60	51.90	51.40
Al ₂ O ₃	15.20	15.55	15.45	15.10	14.40	16.05	16.40	16.15	15.95	17.05	15.65	14.95
Fe ₂ O ₃	4.33	5.47	6.15	5.77	4.62	5.71	5.82	5.01	10.60	10.60	8.86	12.20
CaO	4.50	3.77	5.51	4.88	4.47	5.41	5.31	3.93	9.42	8.01	8.64	7.39
MgO	2.13	2.84	3.36	2.98	2.01	2.66	2.83	2.65	8.61	9.04	7.50	4.97
Na ₂ O	5.08	4.96	4.57	4.41	4.31	4.68	4.73	4.66	3.46	3.22	4.04	4.32
K ₂ O	0.40	0.57	0.46	0.49	0.33	0.51	0.67	0.59	0.70	0.96	0.87	0.81
Cr ₂ O ₃	0.01	<0.01	-	-	-	-	-	-	-	-	0.04	<0.01
TiO ₂	0.37	0.40	0.57	0.51	0.40	0.41	0.41	0.40	1.42	1.35	1.30	2.36
MnO	0.08	0.07	0.10	0.09	0.06	0.09	0.10	0.07	0.20	0.17	0.17	0.21
P ₂ O ₅	0.04	0.06	0.08	0.10	0.07	0.07	0.08	0.08	0.14	0.19	0.13	0.28
S	0.11	<0.01	0.11	0.02	0.25	0.01	0.01	0.03	0.01	0.01	<0.01	0.07
LOI	0.51	2.25	0.61	0.61	0.79	0.37	0.53	2.07	1.24	2.82	1.01	1.23
Total	101.09	101.50	100.86	98.94	99.16	98.96	99.48	100.41	99.74	100.01	100.11	100.12
Mg#	49	51	52	51	46	48	49	51	62	63	63	45
A/CNK	0.90	0.99	0.86	0.91	0.92	0.89	0.90	1.05	0.68	0.82	0.67	0.70

Trace elements (ppm), measured by ICP-MS

Ba	222	244	217	260	203	284	398	371	235	214	323	198
Ce	19.9	16.8	22.0	19.8	14.6	20.4	21.6	17.2	15.2	17.0	14.7	23.9
Cr	20	10	40	60	30	20	20	10	320	300	270	30
Cs	0.26	1.18	0.35	0.54	0.40	0.39	0.49	1.06	0.93	1.90	0.76	1.12
Dy	2.33	1.62	2.56	2.72	1.65	2.06	2.40	1.88	3.99	4.47	4.30	7.04
Er	1.53	1.10	1.76	1.70	0.91	1.18	1.51	1.13	2.35	2.68	2.94	4.17
Eu	0.66	0.57	0.72	0.76	0.44	0.57	0.64	0.62	1.23	1.49	1.16	1.80
Ga	14.5	15.9	15.9	16.5	15.0	17.6	17.6	15.9	16.9	22.2	17.1	23.6
Gd	2.44	1.69	3.09	3.09	1.62	2.46	2.93	2.33	4.31	4.64	4.47	7.14
Hf	3.5	3.5	3.3	4.0	3.2	2.9	3.0	3.1	2.9	2.7	2.6	4.0
Ho	0.50	0.33	0.56	0.60	0.32	0.44	0.56	0.38	0.97	1.02	0.97	1.41
La	8.3	8.0	9.7	9.4	7.8	10.0	10.0	8.6	6.4	7.9	6.4	9.8
Lu	0.27	0.20	0.29	0.34	0.14	0.22	0.29	0.21	0.41	0.44	0.37	0.59
Nb	2.3	1.9	3.4	3.3	1.9	2.4	2.0	2.0	4.0	4.9	3.8	4.4
Nd	10.8	9.2	12.5	12.2	7.7	11.0	11.7	9.8	10.4	13.6	10.6	19.1
Pr	2.41	2.06	3.03	2.85	1.76	2.86	2.94	2.44	2.14	2.76	2.23	3.85
Rb	7.9	13.9	7.0	10.8	5.3	8.9	14.1	14.2	12.0	28.8	16.4	17.6
Sm	2.71	1.99	2.67	3.10	1.62	2.25	2.56	2.26	3.00	3.88	3.40	5.28
Sr	250.0	287.0	298.0	292.0	288.0	308.0	319.0	331.0	167.5	267.0	192.0	249.0
Ta	0.3	0.4	0.4	0.6	0.1	-	-	-	0.2	0.6	0.2	0.1
Tb	0.36	0.23	0.45	0.48	0.25	0.40	0.35	0.33	0.72	0.79	0.74	1.11
Th	0.74	1.14	1.15	1.32	1.43	1.62	1.23	1.37	0.96	0.35	0.84	1.21
Tm	0.24	0.16	0.29	0.26	0.13	0.22	0.24	0.19	0.41	0.40	0.39	0.63
U	0.38	0.55	0.69	0.53	0.78	0.97	0.41	0.38	1.22	0.76	0.56	0.65
V	78	113	151	132	99	130	135	110	257	316	227	362
Y	14.9	9.9	16.6	17.5	9.1	14.2	15.5	11	22.4	26.1	24.2	40.6
Yb	1.66	1.18	2.09	2.15	1.03	1.71	1.92	1.45	2.63	2.65	2.51	4.37
Zr	134	107	126	143	105	98	97	110	96	107	99	193
Ni	13	10	18	19	18	11	12	10	55	97	53	5
Pb	2	<2	-	3	-	5	3	3	2	2	<2	<2
Sc	10	14	16	15	10	14	14	13	33	21	35	31
Zn	33	46	52	50	38	48	50	52	90	86	81	73
Nb/Nb* ¹	0.3	0.2	0.3	0.3	0.2	0.2	0.2	0.2	0.5	1.0	0.6	0.4
Zr/Zr* ²	1.7	1.7	1.5	1.6	2.1	1.4	1.2	1.6	1.2	1.0	1.1	1.3
Ti/Ti* ³	0.3	0.5	0.5	0.4	0.6	0.4	0.4	0.4	0.9	0.8	0.8	0.9
Eu/Eu* ⁴	0.78	0.95	0.77	0.75	0.83	0.74	0.71	0.83	1.05	1.07	0.91	0.90

¹ Nb* defined as NbN/sqrt(ThN*LaN) where N stands for normalized to N-MORB values² Zr* defined as ZrN/sqrt(SmN*NdN) where N stands for normalized to N-MORB values³ Ti* defined as TiN/sqrt(SmN*GdN) where N stands for normalized to N-MORB values⁴ Eu* defined as EuN/sqrt(SmN*GdN') where N' stands for normalized to chondrite values

Table S2: Representative mineral analyses of the amphibole-bearing felsic gneisses RV-1 & RV-2

	biotite ($A_1M_3T_4O_{10}W_2$)		
	RV1-b13	RV1-b14	RV1-b18
SiO ₂	36.91	37.06	37.21
TiO ₂	3.27	3.42	3.41
Al ₂ O ₃	14.52	14.18	14.74
FeOt	17.50	17.96	17.51
MnO	0.15	0.20	0.23
MgO	12.84	12.99	12.94
CaO	0.00	0.00	0.00
Na ₂ O	0.24	0.27	0.29
K ₂ O	9.30	9.16	8.99
Total	94.74	95.25	95.32
T. Si	2.83	2.83	2.83
T.Al	1.03	1.01	1.04
T.Fe ³⁺	0.15	0.16	0.13
M.Al	0.28	0.26	0.28
M.Mg	1.46	1.47	1.45
M.Fe ²⁺	0.87	0.86	0.84
M.Fe ³⁺	0.10	0.13	0.14
M.Ti	0.19	0.20	0.19
M.Mn	0.0	0.0	0.0
sum oct	2.91	2.93	2.92
A.K	0.91	0.89	0.88
A.Na	0.04	0.04	0.04
sum inter	0.95	0.93	0.92
W.OH	1.55	1.52	1.51
W.O ²⁻	0.45	0.48	0.49
Fe ³⁺ /Fe _{tot}	0.22	0.25	0.25
mg#	0.63	0.63	0.63

	amphibole ($A_{0.1}B_2C_5T_8O_{22}W_2$)						
	RV1-a1	RV1-a2	RV1-a11	RV1-a6	RV1-a7	RV2-a14	RV2-a2
SiO ₂	46.43	46.12	47.48	46.62	46.41	46.62	46.04
TiO ₂	0.86	0.94	0.97	0.85	0.86	0.90	0.76
Al ₂ O ₃	8.51	8.67	7.58	8.79	8.39	8.23	9.49
FeOt	15.15	14.76	13.85	14.71	14.81	15.31	16.35
MnO	0.55	0.58	0.53	0.53	0.58	0.56	0.50
MgO	13.33	13.44	13.71	13.09	13.32	13.77	12.04
CaO	10.80	11.30	11.55	10.94	11.22	10.35	11.39
Na ₂ O	1.58	1.39	1.24	1.58	1.46	1.35	1.34
K ₂ O	0.38	0.28	0.34	0.31	0.33	0.37	0.38
Total	97.59	97.50	97.24	97.41	97.37	97.44	98.29
T.Si	6.78	6.74	6.92	6.80	6.79	6.80	6.73
T.Al	1.24	1.29	1.10	1.22	1.24	1.22	1.30
T.sum	8.02	8.03	8.02	8.02	8.03	8.03	8.02
C.Al	0.22	0.20	0.20	0.29	0.20	0.19	0.34
C.Ti	0.12	0.14	0.13	0.12	0.13	0.14	0.11
C.Fe ³⁺	0.64	0.62	0.51	0.57	0.61	0.70	0.57
C.Mn ²⁺	0.04	0.05	0.04	0.04	0.05	0.04	0.04
C.Mg	2.83	2.86	2.94	2.79	2.84	2.89	2.57
C.Fe ²⁺	1.11	1.09	1.14	1.15	1.13	1.01	1.35
C.sum	4.96	4.96	4.96	4.97	4.96	4.96	4.98
B.Mn ²⁺	0.02	0.02	0.02	0.02	0.02	0.03	0.02
B.Fe ²⁺	0.10	0.09	0.03	0.07	0.07	0.16	0.08
B.Mg	0.08	0.07	0.04	0.06	0.06	0.11	0.05
B.Ca	1.70	1.78	1.81	1.72	1.77	1.63	1.79
B.Na	0.08	0.02	0.08	0.11	0.06	0.04	0.04
B.sum	1.98	1.98	1.99	1.98	1.98	1.97	1.98
A.Na	0.37	0.37	0.27	0.34	0.35	0.34	0.34
A.K	0.07	0.06	0.06	0.06	0.07	0.07	0.07
A.sum	0.44	0.43	0.33	0.40	0.42	0.41	0.41
W.OH	1.80	1.80	1.88	1.84	1.84	1.73	1.82
W.O ²⁻	0.20	0.20	0.12	0.16	0.16	0.27	0.18
Fe ³⁺ /Fe _{tot}	0.34	0.35	0.30	0.32	0.34	0.37	0.29
mg#	0.70	0.71	0.72	0.70	0.71	0.72	0.65

	plagioclase						
	RV1-p2	RV1-p6	RV1-p8	RV1-p13	RV2-p1	RV2-p3	RV2-p8
SiO ₂	62.43	62.18	62.12	62.24	62.12	62.02	62.12
Al ₂ O ₃	23.75	23.54	23.71	23.78	23.23	23.60	23.63
FeOt	0.00	0.00	0.14	0.00	0.00	0.17	0.00
CaO	5.38	5.07	5.18	5.57	5.28	5.78	5.54
Na ₂ O	8.44	8.64	8.78	8.40	8.80	8.60	8.78
K ₂ O	0.23	0.22	0.19	0.22	0.15	0.24	0.11
Total	100.23	99.65	100.13	100.22	99.58	100.42	100.17
Si	2.76	2.76	2.75	2.75	2.77	2.75	2.75
Al	1.24	1.23	1.24	1.24	1.22	1.23	1.23
Fe ²⁺	0.00	0.00	0.01	0.00	0.00	0.01	0.00
Ca	0.25	0.24	0.25	0.26	0.25	0.27	0.26
Na	0.72	0.75	0.75	0.72	0.76	0.74	0.75
K	0.01	0.01	0.01	0.01	0.01	0.01	0.01
Sum	4.99	5.00	5.01	4.99	5.01	5.01	5.01
An	25.7	24.2	24.3	26.5	24.7	26.7	25.7
Ab	73.0	74.6	74.6	72.3	74.5	71.9	73.7
Or	1.3	1.2	1.1	1.3	0.8	1.3	0.6

Table S3: Results of LA-ICP-MS U-Pb analyses of zircon standards performed during the sessions at GUF

grain	$^{207}\text{Pb}^{\text{a}}$ (cps)	U ^b (ppm)	Pb ^b (ppm)	Th ^b U	$^{206}\text{Pb}_{\text{bc}}^{\text{c}}$ (%)	$\frac{^{206}\text{Pb}^{\text{d}}}{^{238}\text{U}}$ (%)	$\pm 2\sigma$	$\frac{^{207}\text{Pb}^{\text{d}}}{^{235}\text{U}}$ (%)	$\pm 2\sigma$	$\frac{^{207}\text{Pb}^{\text{d}}}{^{206}\text{Pb}}$ (%)	$\pm 2\sigma$	rho ^e	$\frac{^{206}\text{Pb}^{\text{d}}}{^{238}\text{U}}$ (Ma)	$\pm 2\sigma$	$\frac{^{207}\text{Pb}^{\text{d}}}{^{235}\text{U}}$ (Ma)	$\pm 2\sigma$	$\frac{^{207}\text{Pb}^{\text{d}}}{^{206}\text{Pb}}$ (Ma)	$\pm 2\sigma$	conc. ^f (%)	
<i>Seq. 1</i>																				
Pleso-01	35868	16433	854	0.18	0.07	0.05462	1.4	0.4004	1.9	0.05317	1.3	0.74	343	5	342	6	336	30	102	
Pleso-02	36752	17580	922	0.18	0.01	0.05516	1.4	0.4077	1.5	0.05360	0.6	0.91	346	5	347	5	354	15	98	
Pleso-03	32918	16568	864	0.18	0.00	0.05488	1.4	0.4017	1.6	0.05309	0.7	0.89	344	5	343	5	333	16	104	
Pleso-04	32844	17053	867	0.18	b.d.	0.05344	1.4	0.3922	1.6	0.05323	0.7	0.90	336	5	336	5	339	16	99	
Pleso-05	32105	17287	884	0.18	b.d.	0.05380	1.4	0.3919	1.5	0.05284	0.7	0.89	338	4	336	4	322	16	105	
Pleso-06	29247	15678	818	0.19	b.d.	0.05468	1.4	0.4055	1.6	0.05378	0.8	0.87	343	5	346	5	362	18	95	
Pleso-07	28914	16278	834	0.19	0.00	0.05377	1.4	0.3955	1.5	0.05335	0.6	0.91	338	5	338	4	344	15	98	
Pleso-08	27534	16446	835	0.18	0.00	0.05338	1.4	0.3873	1.6	0.05263	0.9	0.84	335	4	332	5	313	20	107	
Pleso-09	27940	16927	856	0.18	0.00	0.05311	1.4	0.3878	1.6	0.05295	0.8	0.87	334	5	333	5	327	18	102	
Pleso-10	28760	17792	897	0.18	b.d.	0.05295	1.4	0.3891	1.6	0.05330	0.7	0.90	333	5	334	4	342	15	97	
Pleso-11	27316	17250	875	0.18	0.00	0.05326	1.4	0.3928	1.6	0.05350	0.8	0.87	334	5	336	5	350	18	96	
Pleso-12	27316	17248	878	0.18	0.00	0.05346	1.4	0.3943	1.6	0.05350	0.8	0.87	336	5	338	5	350	18	96	
Pleso-13	24378	15912	806	0.18	b.d.	0.05319	1.4	0.3921	1.6	0.05347	0.7	0.89	334	5	336	5	349	16	96	
Pleso-14	27660	17529	891	0.18	0.00	0.05337	1.4	0.3938	1.5	0.05352	0.7	0.88	335	4	337	4	351	16	96	
BB16-1	21488	5433	486	0.31	b.d.	0.09059	1.4	0.7415	1.7	0.05937	0.8	0.86	559	8	563	7	581	18	96	
BB16-2	18605	5106	450	0.32	0.02	0.08926	1.4	0.7370	1.6	0.05988	0.8	0.86	551	7	561	7	599	18	92	
BB16-3	15540	5166	464	0.31	0.00	0.09142	1.4	0.7390	1.7	0.05863	1.0	0.81	564	7	562	7	553	21	102	
BB16-4	14731	5471	491	0.28	0.01	0.09167	1.4	0.7492	1.7	0.05927	0.9	0.82	565	7	568	7	577	21	98	
BB16-5	19335	5004	447	0.32	0.10	0.09059	1.4	0.7341	1.7	0.05877	0.9	0.83	559	7	559	7	559	20	100	
BB16-6	19147	5239	457	0.31	0.02	0.08847	1.4	0.7204	1.6	0.05905	0.8	0.86	546	7	551	7	569	18	96	
BB16-7	17506	5087	454	0.32	0.02	0.09050	1.4	0.7368	1.7	0.05905	0.9	0.83	558	8	561	7	569	20	98	
BB16-8	18202	5608	502	0.30	0.11	0.09112	1.4	0.7394	1.6	0.05885	0.8	0.88	562	8	562	7	562	17	100	
BB16-9	17249	5210	465	0.32	0.00	0.09052	1.4	0.7416	1.6	0.05942	0.9	0.85	559	7	563	7	583	19	96	
BB16-10	16662	5166	465	0.32	0.00	0.09119	1.4	0.7498	1.7	0.05963	1.0	0.81	563	8	568	7	590	22	95	
BB16-11	15400	5189	464	0.31	0.00	0.09074	1.4	0.7422	1.8	0.05932	1.1	0.79	560	7	564	8	579	23	97	
BB16-12	15617	5202	466	0.32	b.d.	0.09082	1.4	0.7404	1.7	0.05913	0.9	0.83	560	7	563	7	572	20	98	
BB16-13	12574	4289	385	0.31	b.d.	0.09112	1.4	0.7380	1.6	0.05874	0.9	0.83	562	7	561	7	557	20	101	
<i>Seq. 2</i>																				
Pleso-01	41966	21077	1096	0.18	0.14	0.05471	1.0	0.4036	1.2	0.05351	0.6	0.85	343	3	344	4	350	15	98	
Pleso-02	40803	18094	947	0.20	0.71	0.05426	1.1	0.3968	2.3	0.05304	2.0	0.47	341	4	339	7	330	46	103	
Pleso-03	36733	19273	985	0.19	0.10	0.05373	1.1	0.3919	1.2	0.05290	0.6	0.88	337	4	336	3	325	13	104	
Pleso-04	37351	19504	1010	0.20	0.14	0.05448	1.1	0.4005	1.3	0.05332	0.8	0.82	342	4	342	4	342	17	100	
Pleso-05	35210	18668	954	0.20	b.d.	0.05364	1.1	0.3928	1.3	0.05311	0.8	0.82	337	4	336	4	333	17	101	
Pleso-06	34759	18762	977	0.20	0.19	0.05471	1.1	0.4036	1.4	0.05351	0.8	0.79	343	4	344	4	350	19	98	
Pleso-07	34602	19160	982	0.20	b.d.	0.05386	1.1	0.3961	1.3	0.05334	0.6	0.86	338	4	339	4	343	15	99	
Pleso-08	32719	18352	930	0.20	b.d.	0.05319	1.2	0.3892	1.4	0.05307	0.7	0.85	334	4	334	4	332	17	101	
Pleso-09	33495	18896	953	0.20	b.d.	0.05298	1.1	0.3898	1.3	0.05336	0.7	0.85	333	4	334	4	344	15	97	
Pleso-10	30845	17070	874	0.21	b.d.	0.05365	1.1	0.3967	1.3	0.05363	0.8	0.81	337	3	339	4	356	17	95	
Pleso-11	27316	17055	801	0.20	0.00	0.04931	1.1	0.3640	1.4	0.05354	0.8	0.82	310	3	315	4	352	18	88	
Pleso-12	29334	16937	867	0.21	0.26	0.05367	1.2	0.3952	1.5	0.05340	0.9	0.79	337	4	338	4	346	21	97	
Pleso-13	35935	17731	911	0.20	1.65	0.05294	1.1	0.3901	3.2	0.05345	3.0	0.35	333	4	334	9	348	67	96	
Pleso-14	33275	19651	1001	0.20	b.d.	0.05348	1.2	0.3951	1.3	0.05358	0.7	0.86	336	4	338	4	353	15	95	
BB16-1	22924	5769	524	0.34	0.07	0.09208	1.1	0.7480	2.6	0.05892	2.3	0.43	568	6	567	11	564	50	101	
BB16-2	19468	5318	478	0.35	0.29	0.09116	1.1	0.7375	3.1	0.05868	2.9	0.36	562	6	561	13	555	63	101	
BB16-3	17271	5089	455	0.35	0.18	0.09055	1.1	0.7347	1.5	0.05884	1.1	0.72	559	6	559	7	561	23	100	
BB16-4	18041	5421	492	0.45	b.d.	0.09039	1.1	0.7411	2.3	0.05947	2.0	0.49	558	6	563	10	584	43	95	

Table S3 (cont.): Results of LA-ICP-MS U-Pb analyses of zircon standards performed during the sessions at GUF

grain	$^{207}\text{Pb}^{\text{a}}$ (cps)	U ^b (ppm)	Pb ^b (ppm)	Th ^b U	$^{206}\text{Pb}_{\text{bc}}^{\text{c}}$ ^{238}U	$^{206}\text{Pb}^{\text{d}}$ ^{238}U	$\pm 2\sigma$ (%)	$^{207}\text{Pb}^{\text{d}}$ ^{235}U	$\pm 2\sigma$ (%)	$^{207}\text{Pb}^{\text{d}}$ ^{206}Pb	$\pm 2\sigma$ (%)	ρho^{e}	$^{206}\text{Pb}^{\text{d}}$ ^{238}U	$\pm 2\sigma$ (Ma)	$^{206}\text{Pb}^{\text{d}}$ ^{235}U	$\pm 2\sigma$ (Ma)	$^{207}\text{Pb}^{\text{d}}$ ^{206}Pb	$\pm 2\sigma$ (Ma)	conc. ^f (%)
BB16-5	20108	5355	485	0.35	b.d.	0.09172	1.1	0.7477	1.5	0.05912	1.1	0.72	566	6	567	7	572	23	99
BB16-6	20313	5574	501	0.34	b.d.	0.09116	1.1	0.7434	1.4	0.05914	0.8	0.79	562	6	564	6	572	18	98
BB16-7	20668	5886	523	0.35	0.15	0.09008	1.1	0.7315	1.4	0.05890	0.8	0.80	556	6	557	6	563	18	99
BB16-8	19610	5637	506	0.35	0.01	0.09101	1.1	0.7401	1.3	0.05898	0.8	0.83	561	6	562	6	566	16	99
BB16-9	19025	5573	494	0.35	0.18	0.08977	1.1	0.7295	1.4	0.05894	0.9	0.78	554	6	556	6	565	19	98
BB16-10	19577	5695	510	0.36	0.40	0.09086	1.1	0.7336	3.4	0.05856	3.2	0.32	561	6	559	15	551	70	102
BB16-11	18476	5593	498	0.35	b.d.	0.09040	1.1	0.7377	1.4	0.05918	0.9	0.77	558	6	561	6	574	20	97
BB16-12	18840	5670	506	0.36	0.16	0.09037	1.1	0.7356	1.5	0.05903	0.9	0.76	558	6	560	6	568	21	98
BB16-13	18033	5700	515	0.35	b.d.	0.09165	1.1	0.7445	1.4	0.05891	0.9	0.79	565	6	565	6	564	19	100

Spot size = 30µm; depth of crater ~20µm. $^{206}\text{Pb}/^{238}\text{U}$ error is the quadratic addition of the within run precision (2 SE) and the external reproducibility (2 SD) of the reference zircon.

$^{207}\text{Pb}/^{206}\text{Pb}$ error propagation (^{207}Pb signal dependent) following Gerdes & Zeh (2009). $^{207}\text{Pb}/^{235}\text{U}$ error is the quadratic addition of the $^{207}\text{Pb}/^{206}\text{Pb}$ and $^{206}\text{Pb}/^{238}\text{U}$ uncertainty.

^aWithin run background-corrected mean ^{207}Pb signal in cps (counts per second).

^b U and Pb content and Th/U ratio were calculated relative to GJ-1 reference zircon.

^c percentage of the common Pb on the ^{206}Pb . b.d. = below detection limit.

^d corrected for background, within-run Pb/U fractionation (in case of $^{206}\text{Pb}/^{238}\text{U}$) and subsequently normalised to GJ-1 (ID-TIMS value/measured value);

^e $^{207}\text{Pb}/^{235}\text{U}$ calculated using $^{207}\text{Pb}/^{206}\text{Pb}/(^{238}\text{U}/^{206}\text{Pb} * 1/137.88)$

^f rho is the $^{206}\text{Pb}/^{238}\text{U}$ / $^{207}\text{Pb}/^{235}\text{U}$ error correlation coefficient.

^f degree of concordance = $^{206}\text{Pb}/^{238}\text{U}$ age / $^{207}\text{Pb}/^{206}\text{Pb}$ age x 100

Table S4: Results of LA-ICP-MS zircon U-Pb analyses performed during the sessions at GUF

grain	$^{207}\text{Pb}^{\text{a}}$ (cps)	U ^b (ppm)	Pb ^b (ppm)	Th ^b U	$^{206}\text{Pbc}^{\text{c}}$ (%)	$\frac{^{206}\text{Pb}^{\text{d}}}{^{238}\text{U}}$ (%)	$\pm 2\text{s}$	$\frac{^{207}\text{Pb}^{\text{d}}}{^{235}\text{U}}$ (%)	$\pm 2\text{s}$	$\frac{^{207}\text{Pb}^{\text{d}}}{^{206}\text{Pb}}$ (%)	$\pm 2\text{s}$	rho ^e (%)	$\frac{^{206}\text{Pb}}{^{238}\text{U}}$ (Ma)	$\pm 2\text{s}$	$\frac{^{207}\text{Pb}}{^{235}\text{U}}$ (Ma)	$\pm 2\text{s}$	$\frac{^{207}\text{Pb}}{^{206}\text{Pb}}$ (Ma)	$\pm 2\text{s}$	conc. ^f (%)
Seq.1																			
RV-1 Riverie tonalite																			
a585	8430	2826	204	0.19	0.51	0.07213	1.7	0.6911	2.1	0.06949	1.3	0.80	449	7	533	9	913	26	49
a586	10989	3594	309	0.33	0.52	0.08485	1.4	0.7847	1.8	0.06707	1.2	0.78	525	7	588	8	840	24	63
a587	5431	1877	158	0.24	0.80	0.08644	1.8	0.7115	2.2	0.05969	1.3	0.80	534	9	546	9	593	29	90
a588	5922	2264	182	0.27	0.42	0.08220	1.9	0.6633	2.3	0.05852	1.2	0.85	509	9	517	9	549	26	93
a589	9900	4484	281	0.11	0.83	0.06550	1.6	0.5542	1.9	0.06136	1.1	0.83	409	6	448	7	652	23	63
a590	6832	2423	201	0.17	0.25	0.08686	1.6	0.7028	2.4	0.05869	1.7	0.68	537	8	540	10	556	38	97
a595	6912	1986	171	0.26	b.d.	0.08865	1.8	0.7287	2.2	0.05962	1.3	0.80	548	9	556	9	590	29	93
a596	4811	1127	95	0.18	b.d.	0.08795	2.2	0.7001	2.7	0.05774	1.6	0.81	543	11	539	11	520	35	105
a598	9600	3426	288	0.17	0.31	0.08827	1.5	0.7162	1.9	0.05885	1.2	0.78	545	8	548	8	562	26	97
Seq.2																			
RV-1 Riverie tonalite																			
a06	9688	2655	222	0.18	b.d.	0.08766	1.1	0.7075	1.8	0.05854	1.4	0.63	542	6	543	8	550	31	99
a08	18090	4995	426	0.25	b.d.	0.08814	1.2	0.7159	1.7	0.05891	1.3	0.68	545	6	548	7	564	28	97
a09	6981	1930	166	0.29	b.d.	0.08847	1.3	0.7186	1.9	0.05891	1.4	0.67	547	7	550	8	564	31	97
a10	25713	7190	622	0.45	0.12	0.08625	1.1	0.7012	1.3	0.05896	0.7	0.83	533	6	539	5	566	16	94
a11	20421	6176	496	0.20	0.60	0.08348	1.1	0.6864	1.7	0.05963	1.3	0.67	517	6	531	7	590	27	88
a12	24433	6250	491	0.14	0.30	0.08257	1.4	0.6855	1.9	0.06021	1.2	0.75	511	7	530	8	611	26	84
a13	13206	3800	323	0.26	0.22	0.08766	1.3	0.7219	1.9	0.05973	1.3	0.72	542	7	552	8	594	28	91
a14	53651	14479	901	0.16	3.07	0.05980	1.6	0.6609	7.8	0.08015	7.7	0.20	374	6	515	32	1201	151	31
a15	14078	3741	330	0.38	0.11	0.08869	1.1	0.7250	1.5	0.05929	1.0	0.73	548	6	554	6	578	22	95
a16	23141	6227	388	0.14	2.51	0.06080	1.4	0.6388	3.4	0.07619	3.1	0.40	381	5	502	14	1100	62	35
a17	5766	1552	133	0.24	b.d.	0.08882	1.2	0.7193	1.9	0.05874	1.5	0.60	549	6	550	8	557	34	98
a18	11666	3173	268	0.16	0.37	0.08893	1.1	0.7145	1.6	0.05827	1.2	0.67	549	6	547	7	540	26	102
a19	26879	7211	636	0.43	0.34	0.08793	1.1	0.7199	1.5	0.05938	1.0	0.76	543	6	551	6	581	21	93
a20	8492	2252	193	0.34	b.d.	0.08675	1.9	0.6913	2.3	0.05780	1.4	0.80	536	10	534	10	522	31	103
a21	15679	4029	342	0.18	b.d.	0.08871	1.2	0.7193	1.5	0.05881	0.9	0.81	548	6	550	6	560	19	98
a22	18932	4363	397	0.33	0.73	0.08880	1.3	0.8837	2.8	0.07218	2.5	0.45	548	7	643	14	991	51	55
a23	12437	3210	271	0.20	0.13	0.08753	1.2	0.7460	2.1	0.06181	1.7	0.57	541	6	566	9	668	37	81
a24	13707	3788	320	0.18	b.d.	0.08846	1.4	0.7163	2.2	0.05873	1.8	0.61	546	7	548	9	557	39	98
a25	10735	3021	255	0.21	0.20	0.08822	1.1	0.7120	1.5	0.05853	1.0	0.73	545	6	546	6	550	23	99
a26	20787	6006	425	0.52	1.34	0.06922	1.4	0.6544	2.5	0.06857	2.1	0.55	431	6	511	10	886	43	49
a30	7549	2271	180	0.17	0.19	0.08321	1.2	0.6680	1.9	0.05822	1.5	0.62	515	6	519	8	538	32	96
a31	12129	3529	300	0.23	0.08	0.08827	1.3	0.7193	1.9	0.05910	1.3	0.70	545	7	550	8	571	29	96
a39	9017	2542	219	0.35	0.56	0.08744	1.2	0.7084	1.9	0.05876	1.5	0.60	540	6	544	8	558	34	97
a40	11338	3210	276	0.30	0.05	0.08804	1.1	0.7132	1.6	0.05875	1.2	0.69	544	6	547	7	558	25	97
a41	19538	5463	449	0.26	0.14	0.08474	1.1	0.6879	1.5	0.05888	1.0	0.75	524	6	532	6	562	21	93
a42	6893	1945	165	0.24	0.17	0.08771	1.1	0.7159	1.9	0.05920	1.5	0.62	542	6	548	8	574	32	94
a43	16084	4535	383	0.22	0.37	0.08791	1.1	0.7102	1.6	0.05859	1.2	0.67	543	6	545	7	552	26	98
a44	15981	4483	379	0.28	b.d.	0.08661	1.1	0.7178	1.8	0.06011	1.4	0.61	535	6	549	8	607	31	88
a45	12947	3444	284	0.33	0.02	0.08367	1.2	0.6817	2.1	0.05909	1.8	0.55	518	6	528	9	570	39	91
a46	22829	6172	520	0.24	0.14	0.08721	1.2	0.7145	1.5	0.05942	0.9	0.82	539	6	547	6	583	19	93
a47	12283	3383	296	0.44	0.37	0.08575	1.1	0.7361	1.8	0.06226	1.5	0.61	530	6	560	8	683	31	78

Table S4 (cont.): Results of LA-ICP-MS zircon U–Pb analyses performed during the sessions at GUF

grain	$^{207}\text{Pb}^{\text{a}}$ (cps)	U ^b (ppm)	Pb ^b (ppm)	Th ^b U	$^{206}\text{Pb}_{\text{bc}}^{\text{c}}$ (%)	$\frac{^{206}\text{Pb}^{\text{d}}}{^{238}\text{U}}$ (%)	$\pm 2s$	$\frac{^{207}\text{Pb}^{\text{d}}}{^{235}\text{U}}$ (%)	$\pm 2s$	$\frac{^{207}\text{Pb}^{\text{d}}}{^{206}\text{Pb}}$ (%)	$\pm 2s$	rho^{e}	$\frac{^{206}\text{Pb}}{^{238}\text{U}}$ (Ma)	$\pm 2s$	$\frac{^{207}\text{Pb}}{^{235}\text{U}}$ (Ma)	$\pm 2s$	$\frac{^{207}\text{Pb}}{^{206}\text{Pb}}$ (Ma)	$\pm 2s$	conc. ^f (%)	
RV-2 Riverie tonalite																				
a48	25583	6386	548	0.35	b.d.	0.08671	1.2	0.7024	1.4	0.05875	0.8	0.83	536	6	540	6	558	17	96	
a49	23129	6639	560	0.30	0.13	0.08650	1.0	0.7019	1.3	0.05885	0.8	0.80	535	5	540	5	561	17	95	
a50	20688	6456	491	0.23	0.82	0.07800	1.1	0.7203	2.4	0.06697	2.1	0.48	484	5	551	10	837	43	58	
a52	9945	2884	242	0.15	b.d.	0.08845	1.3	0.7166	1.7	0.05876	1.2	0.74	546	7	549	7	558	25	98	
a53	12588	3570	296	0.16	b.d.	0.08760	1.3	0.7100	1.6	0.05878	1.1	0.76	541	7	545	7	559	23	97	
a54	14985	6119	503	0.17	0.10	0.08675	1.1	0.6978	1.6	0.05834	1.2	0.68	536	6	537	7	543	25	99	
a55	8856	2546	213	0.15	b.d.	0.08831	1.3	0.7163	1.9	0.05882	1.3	0.72	546	7	548	8	561	29	97	
a56	9125	1713	143	0.35	b.d.	0.08398	1.3	0.6815	1.8	0.05885	1.3	0.72	520	6	528	7	562	27	93	
a57	9625	2758	235	0.20	0.15	0.08902	1.4	0.7256	2.0	0.05912	1.5	0.68	550	7	554	9	571	32	96	
a58	28610	7910	688	0.31	0.15	0.08861	1.2	0.7425	1.5	0.06078	0.8	0.82	547	6	564	6	631	18	87	
a59	21735	6533	537	0.25	b.d.	0.08519	1.2	0.6896	1.9	0.05871	1.4	0.67	527	6	533	8	556	30	95	
a60	17491	5636	392	0.37	0.31	0.07033	1.6	0.5948	2.1	0.06134	1.4	0.74	438	7	474	8	651	31	67	
a61	20187	5762	488	0.29	b.d.	0.08716	1.1	0.7050	1.4	0.05867	0.9	0.78	539	6	542	6	555	19	97	
a62	7942	2271	194	0.25	0.82	0.08874	1.4	0.7105	2.2	0.05807	1.7	0.64	548	7	545	9	532	36	103	
a63	16612	4685	399	0.22	0.03	0.08877	1.2	0.7183	1.5	0.05869	0.8	0.83	548	6	550	6	556	18	99	
a64	7247	2086	178	0.29	0.27	0.08795	1.2	0.7041	2.3	0.05806	1.9	0.53	543	6	541	10	532	42	102	
a65	41973	18749	990	0.02	0.11	0.05764	1.2	0.4285	1.4	0.05392	0.7	0.85	361	4	362	4	368	17	98	
a66	48222	14744	771	0.04	0.38	0.05638	1.3	0.4369	1.6	0.05620	1.0	0.78	354	4	368	5	460	22	77	
a72	17516	5068	435	0.25	b.d.	0.08880	1.2	0.7124	1.6	0.05819	1.1	0.74	548	6	546	7	537	23	102	
a73	18478	5346	442	0.20	b.d.	0.08649	1.1	0.6985	1.4	0.05857	0.9	0.77	535	5	538	6	551	19	97	
a74	10193	2954	245	0.17	0.48	0.08726	1.3	0.7060	2.0	0.05869	1.6	0.64	539	7	542	9	555	34	97	
a75	20755	6060	513	0.23	0.18	0.08812	1.2	0.7119	1.5	0.05859	0.9	0.79	544	6	546	6	552	19	99	
a76	17379	5120	440	0.34	0.19	0.08738	1.1	0.7001	1.5	0.05811	0.9	0.76	540	6	539	6	534	21	101	
a79	8186	2395	202	0.21	b.d.	0.08814	1.2	0.7185	1.9	0.05912	1.4	0.65	545	6	550	8	571	31	95	
a80	25436	7531	634	0.26	b.d.	0.08716	1.2	0.6972	1.4	0.05802	0.7	0.85	539	6	537	6	531	16	102	
a81	17242	4824	399	0.25	b.d.	0.08547	1.1	0.6878	1.3	0.05837	0.8	0.79	529	5	531	6	543	18	97	
a82	16995	5061	425	0.21	0.01	0.08761	1.2	0.7054	1.5	0.05840	1.0	0.77	541	6	542	6	545	21	99	
a83	11907	3319	284	0.30	0.34	0.08768	1.4	0.7059	1.9	0.05840	1.2	0.76	542	7	542	8	545	26	99	
a84	12669	3718	305	0.16	b.d.	0.08638	1.2	0.7084	1.5	0.05949	1.0	0.76	534	6	544	6	585	22	91	
a85	17119	4992	419	0.24	b.d.	0.08704	1.2	0.6986	1.5	0.05821	1.0	0.76	538	6	538	6	538	22	100	
a86	17862	4978	425	0.24	0.07	0.08812	1.3	0.7175	1.6	0.05905	0.9	0.81	544	7	549	7	569	20	96	
a88	15424	2921	249	0.20	0.48	0.08903	1.3	0.7186	1.8	0.05854	1.3	0.70	550	7	550	8	550	28	100	
a89	13516	5457	438	0.13	b.d.	0.08513	1.3	0.6858	1.8	0.05843	1.2	0.74	527	7	530	8	546	27	96	

Spot size = 30µm; depth of crater ~20µm. $^{206}\text{Pb}/^{238}\text{U}$ error is the quadratic addition of the within run precision (2 SE)

and the external reproducibility (2 SD) of the reference zircon.

$^{207}\text{Pb}/^{206}\text{Pb}$ error propagation (^{207}Pb signal dependent) following Gerdes & Zeh (2009). $^{207}\text{Pb}/^{235}\text{U}$ error is the quadratic addition of the $^{207}\text{Pb}/^{206}\text{Pb}$ and $^{206}\text{Pb}/^{238}\text{U}$ uncertainty.

^aWithin run background-corrected mean ^{207}Pb signal in cps (counts per second).

^b U and Pb content and Th/U ratio were calculated relative to GJ-1 reference zircon.

^c percentage of the common Pb on the ^{206}Pb . b.d. = below detection limit.

^d corrected for background, within-run Pb/U fractionation (in case of $^{206}\text{Pb}/^{238}\text{U}$), common Pb using Stacy and Kramers (1975) model Pb composition (specified by a *), see text for discussion) and subsequently normalised to GJ-1 (ID-TIMS value/measured value); $^{207}\text{Pb}/^{235}\text{U}$ calculated using $^{207}\text{Pb}/^{206}\text{Pb}/(^{238}\text{U}/^{206}\text{Pb} * 1/137.88)$

^e rho is the $^{206}\text{Pb}/^{238}\text{U}$ / $^{207}\text{Pb}/^{235}\text{U}$ error correlation coefficient.

^f degree of concordance = $^{206}\text{Pb}/^{238}\text{U}$ age / $^{207}\text{Pb}/^{206}\text{Pb}$ age x 100

Table S5: Results of LA-MC-ICP-MS Lu-Hf analyses of zircon standards performed during the session at GUF

	Spot size (μm)	$\frac{^{176}\text{Yb}^{\text{a}}}{^{177}\text{Hf}}$	$\pm 2\sigma$ (abs.)	$\frac{^{176}\text{Lu}^{\text{a}}}{^{177}\text{Hf}}$	$\pm 2\sigma$ (abs.)	$\frac{^{178}\text{Hf}}{^{177}\text{Hf}}$	$\pm 2\sigma$ (abs.)	$\frac{^{180}\text{Hf}}{^{177}\text{Hf}}$	$\pm 2\sigma$ (abs.)	Sig. _{Hf} ^b (V)	$\frac{^{176}\text{Hf}}{^{177}\text{Hf}}$	$\pm 2\sigma$ (abs.)	$\frac{^{176}\text{Hf}^{\text{c}}}{^{177}\text{Hf}_{(\text{t})}}$	$\varepsilon\text{Hf}_{(\text{t})}^{\text{c}}$ $\pm 2\sigma$ (abs.)	
GJ-1															
GJ1-40-12Jcm_1	40	0.0084	0.0007	0.00025	0.00003	1.46720	0.00005	1.88668	0.00010	11	0.281977	0.000033	0.281974	-15.3	1.2
GJ1-40-12Jcm_2	40	0.0080	0.0006	0.00027	0.00002	1.46725	0.00004	1.88639	0.00015	8	0.282005	0.000031	0.282002	-14.3	1.1
GJ1-40-12Jcm_3	40	0.0080	0.0006	0.00026	0.00002	1.46723	0.00007	1.88633	0.00016	8	0.282014	0.000029	0.282011	-14.0	1.0
GJ1-40-12Jcm_4	40	0.0080	0.0006	0.00027	0.00002	1.46722	0.00006	1.88630	0.00012	9	0.282027	0.000033	0.282024	-13.5	1.2
GJ1-40-12Jcm_5	40	0.0076	0.0006	0.00026	0.00002	1.46727	0.00006	1.88650	0.00019	7	0.282001	0.000034	0.281998	-14.4	1.2
GJ1-40-12Jcm_6	40	0.0076	0.0006	0.00026	0.00002	1.46725	0.00006	1.88663	0.00017	8	0.282016	0.000033	0.282013	-13.9	1.2
GJ1-40-12Jcm_7	40	0.0078	0.0006	0.00026	0.00002	1.46724	0.00007	1.88635	0.00014	7	0.282020	0.000030	0.282017	-13.8	1.0
GJ1-40-12Jcm_8	40	0.0078	0.0006	0.00025	0.00002	1.46727	0.00004	1.88626	0.00013	8	0.282026	0.000029	0.282023	-13.6	1.0
GJ1-40-12Jcm_9	40	0.0078	0.0006	0.00025	0.00001	1.46729	0.00006	1.88630	0.00014	8	0.282021	0.000033	0.282018	-13.7	1.2
GJ1-40-12Jcm_10	40	0.0078	0.0006	0.00025	0.00002	1.46734	0.00006	1.88652	0.00014	8	0.282021	0.000032	0.282018	-13.7	1.1
GJ1-40-12Jcm_11	40	0.0078	0.0006	0.00025	0.00002	1.46729	0.00005	1.88632	0.00012	8	0.282013	0.000036	0.282010	-14.0	1.3
GJ1-40-12Jcm_12	40	0.0076	0.0006	0.00025	0.00002	1.46718	0.00006	1.88642	0.00011	8	0.282005	0.000040	0.282002	-14.3	1.4
GJ1-40-12Jcm_13	40	0.0077	0.0006	0.00025	0.00001	1.46727	0.00005	1.88655	0.00015	7	0.282023	0.000034	0.282020	-13.7	1.2
GJ1-40-12Jcm_14	40	0.0074	0.0006	0.00025	0.00001	1.46729	0.00006	1.88618	0.00011	8	0.282027	0.000030	0.282024	-13.5	1.1
GJ1-40-12Jcm_15	40	0.0072	0.0006	0.00025	0.00001	1.46729	0.00005	1.88626	0.00013	8	0.282021	0.000033	0.282018	-13.7	1.2
GJ1-40-12Jcm_16	40	0.0074	0.0006	0.00025	0.00001	1.46720	0.00005	1.88627	0.00014	7	0.282013	0.000031	0.282010	-14.0	1.1
GJ1-40-12Jcm_17	40	0.0073	0.0006	0.00025	0.00001	1.46729	0.00006	1.88623	0.00012	7	0.282016	0.000036	0.282014	-13.9	1.3
GJ1-40-12Jcm_18	40	0.0073	0.0006	0.00024	0.00001	1.46723	0.00005	1.88613	0.00015	7	0.282029	0.000037	0.282026	-13.5	1.3
GJ1-40-12Jcm_19	40	0.0073	0.0006	0.00024	0.00001	1.46732	0.00006	1.88638	0.00013	6	0.282027	0.000033	0.282025	-13.5	1.2
GJ1-40-12Jcm_20	40	0.0072	0.0006	0.00024	0.00001	1.46722	0.00006	1.88643	0.00014	6	0.281989	0.000034	0.281987	-14.8	1.2
GJ1-60-12Jcm_1	60	0.0074	0.0006	0.00024	0.00001	1.46724	0.00004	1.88649	0.00010	14	0.282020	0.000027	0.282017	-13.8	0.9
GJ1-60-12Jcm_2	60	0.0074	0.0006	0.00024	0.00001	1.46721	0.00004	1.88661	0.00008	15	0.282005	0.000026	0.282003	-14.3	0.9
Average		0.0076		0.00025		1.46725		1.88639			0.282014		0.282012	-14.0	
2 S.E. (abs.)		0.0006		0.00002		0.00008		0.00030			0.000026		0.000026	0.9	
2 S.E. (%)		8		7		0.006		0.02			0.0093		0.0093		
Reference value													0.282000	± 23	
Plešovice															
Pleso-40-12Jcm_1	40	0.0066	0.0005	0.00014	0.00001	1.46722	0.00006	1.88643	0.00012	10	0.282472	0.000031	0.282471	-3.6	1.1
Pleso-40-12Jcm_2	40	0.0071	0.0006	0.00015	0.00001	1.46723	0.00004	1.88653	0.00011	11	0.282483	0.000031	0.282482	-3.2	1.1
Pleso-40-12Jcm_3	40	0.0072	0.0006	0.00015	0.00001	1.46728	0.00006	1.88646	0.00012	11	0.282474	0.000032	0.282473	-3.5	1.1
Pleso-40-12Jcm_4	40	0.0071	0.0006	0.00014	0.00001	1.46727	0.00004	1.88662	0.00009	12	0.282470	0.000029	0.282469	-3.7	1.0
Pleso-40-12Jcm_5	40	0.0070	0.0006	0.00014	0.00001	1.46726	0.00004	1.88652	0.00011	12	0.282484	0.000028	0.282483	-3.2	1.0
Pleso-40-12Jcm_6	40	0.0070	0.0006	0.00014	0.00001	1.46727	0.00005	1.88655	0.00011	12	0.282480	0.000030	0.282479	-3.3	1.0
Pleso-40-12Jcm_7	40	0.0068	0.0005	0.00014	0.00001	1.46724	0.00005	1.88644	0.00013	11	0.282478	0.000029	0.282477	-3.4	1.0
Pleso-40-12Jcm_8	40	0.0069	0.0006	0.00014	0.00001	1.46721	0.00005	1.88652	0.00012	11	0.282485	0.000028	0.282484	-3.1	1.0

Table S5 (cont.): Results of LA-MC-ICP-MS Lu-Hf analyses of zircon standards performed during the session at GUF

	Spot size (μm)	$\frac{^{176}\text{Yb}^{\text{a}}}{^{177}\text{Hf}}$	$\pm 2\sigma$	$\frac{^{176}\text{Lu}^{\text{a}}}{^{177}\text{Hf}}$	$\pm 2\sigma$	$\frac{^{178}\text{Hf}}{^{177}\text{Hf}}$	$\pm 2\sigma$	$\frac{^{180}\text{Hf}}{^{177}\text{Hf}}$	$\pm 2\sigma$	$\text{Sig}_{\text{Hf}}^{\text{b}}$ (V)	$\frac{^{176}\text{Hf}}{^{177}\text{Hf}}$	$\pm 2\sigma$	$\frac{^{176}\text{Hf}^{\text{c}}}{^{177}\text{Hf}_{(\text{t})}}$	$\varepsilon\text{Hf}_{(\text{t})}^{\text{c}}$	$\pm 2\sigma$
Pleso-40-12Jcm_9	40	0.0063	0.0005	0.00013	0.00001	1.46721	0.00005	1.88632	0.00011	10	0.282486	0.000032	0.282485	-3.1	1.1
Pleso-40-12Jcm_10	40	0.0064	0.0005	0.00012	0.00002	1.46722	0.00005	1.88652	0.00009	10	0.282472	0.000028	0.282471	-3.6	1.0
Pleso-40-12Jcm_11	40	0.0069	0.0005	0.00014	0.00001	1.46722	0.00004	1.88625	0.00010	10	0.282478	0.000028	0.282477	-3.4	1.0
Pleso-40-12Jcm_12	40	0.0067	0.0006	0.00014	0.00001	1.46728	0.00005	1.88643	0.00012	10	0.282483	0.000030	0.282482	-3.2	1.1
Pleso-40-12Jcm_13	40	0.0067	0.0005	0.00014	0.00001	1.46725	0.00006	1.88637	0.00012	10	0.282473	0.000027	0.282472	-3.5	1.0
Pleso-40-12Jcm_14	40	0.0063	0.0005	0.00013	0.00001	1.46726	0.00004	1.88640	0.00010	11	0.282487	0.000031	0.282486	-3.1	1.1
Average		0.0068		0.00014		1.46724		1.88645			0.282479		0.282478		-3.3
2 S.E. (abs.)		0.0006		0.00002		0.00005		0.00020			0.000012		0.000012		0.4
2 S.E. (%)		9		12		0.004		0.01			0.0041		0.0041		
Reference value													0.282482		± 13
Temora															
TM-40-12Jcm_1	40	0.0190	0.0027	0.00066	0.00008	1.46746	0.00013	1.88586	0.00043	9	0.282710	0.000046	0.282705	6.5	1.6
TM-40-12Jcm_2	40	0.0391	0.0033	0.00130	0.00008	1.46717	0.00004	1.88639	0.00012	9	0.282692	0.000034	0.282682	5.7	1.2
TM-40-12Jcm_3	40	0.0408	0.0034	0.00130	0.00008	1.46726	0.00005	1.88636	0.00014	9	0.282688	0.000031	0.282678	5.5	1.1
TM-40-12Jcm_4	40	0.0416	0.0041	0.00128	0.00010	1.46719	0.00004	1.88649	0.00013	9	0.282695	0.000030	0.282685	5.8	1.1
TM-40-12Jcm_5	40	0.0282	0.0025	0.00093	0.00006	1.46727	0.00007	1.88642	0.00016	9	0.282684	0.000030	0.282677	5.5	1.0
TM-40-12Jcm_6	40	0.0240	0.0019	0.00078	0.00005	1.46733	0.00008	1.88626	0.00024	9	0.282715	0.000040	0.282709	6.6	1.4
TM-40-12Jcm_7	40	0.0190	0.0015	0.00066	0.00004	1.46727	0.00007	1.88633	0.00013	7	0.282702	0.000034	0.282697	6.2	1.2
TM-40-12Jcm_8	40	0.0196	0.0017	0.00061	0.00004	1.46731	0.00006	1.88632	0.00014	8	0.282695	0.000031	0.282690	6.0	1.1
TM-40-12Jcm_9	40	0.0190	0.0015	0.00066	0.00004	1.46725	0.00007	1.88631	0.00012	7	0.282696	0.000030	0.282691	6.0	1.1
TM-40-12Jcm_10	40	0.0152	0.0013	0.00053	0.00004	1.46723	0.00004	1.88623	0.00011	8	0.282682	0.000033	0.282678	5.6	1.2
TM-40-12Jcm_11	40	0.0161	0.0014	0.00055	0.00004	1.46728	0.00007	1.88632	0.00016	7	0.282682	0.000036	0.282678	5.5	1.3
TM-40-12Jcm_12	40	0.0249	0.0021	0.00090	0.00006	1.46738	0.00010	1.88620	0.00027	8	0.282701	0.000041	0.282694	6.1	1.4
Average		0.0255		0.00085		1.46728		1.88629			0.282695		0.282689		5.9
2 S.E. (abs.)		0.0195		0.00059		0.00016		0.00031			0.000021		0.000022		0.8
2 S.E. (%)		76		70		0.011		0.02			0.0075		0.0078		
Reference value													0.282686		± 8

(a) $\frac{^{176}\text{Yb}}{^{177}\text{Hf}} = (\frac{^{176}\text{Yb}}{^{177}\text{Yb}})_{\text{true}} \times (\frac{^{173}\text{Yb}}{^{177}\text{Hf}})_{\text{meas}} \times (M_{173(\text{Yb})}/M_{177(\text{Hf})})^{b(\text{Hf})}$, $b(\text{Hf}) = \ln(\frac{^{179}\text{Hf}}{^{177}\text{Hf}}_{\text{true}} / \frac{^{179}\text{Hf}}{^{177}\text{Hf}}_{\text{measured}}) / \ln(M_{179(\text{Hf})}/M_{177(\text{Hf})})$, M=mass of respective isotope. The $\frac{^{176}\text{Lu}}{^{177}\text{Hf}}$ were calculated in a similar way by using the $\frac{^{175}\text{Lu}}{^{177}\text{Hf}}$ and $b(\text{Yb})$.

(b) Mean Hf signal in volt.

(c) Initial $\frac{^{176}\text{Hf}}{^{177}\text{Hf}}$ and eHf calculated using the reference age for each zircon standard, and the CHUR

parameters: $\frac{^{176}\text{Lu}}{^{177}\text{Hf}} = 0.0336$, and $\frac{^{176}\text{Hf}}{^{177}\text{Hf}} = 0.282785$ (Bouvier *et al.*, 2008).

Table S6: Results of LA-MC-ICP-MS Lu-Hf analyses of zircon performed during the session at GUF

The spots are labelled as RVX-N(-U) with "RVX" the sample name, "N" the Lu-Hf analysis number, "U" the U-Pb analytical spot closest to the domain analysed.

Table S6 (cont.): Results of LA-MC-ICP-MS Lu–Hf analyses of zircon performed during the session at GUF

(a) $^{176}\text{Yb}/^{177}\text{Hf} = (^{176}\text{Yb}/^{173}\text{Yb})_{\text{true}} \times (^{173}\text{Yb}/^{177}\text{Hf})_{\text{meas}} \times (M_{173(\text{Yb})}/M_{177(\text{Hf})})^{b(\text{Hf})}$, $b(\text{Hf}) = \ln(^{179}\text{Hf}/^{177}\text{Hf}$

$\text{true} / ^{179}\text{Hf}/^{177}\text{Hf}_{\text{measured}}) / \ln(M_{179(\text{Hf})}/M_{177(\text{Hf})})$, M=mass of respective isotope. The $^{176}\text{Lu}/^{177}\text{Hf}$ were calculated in a similar way by using the $^{175}\text{Lu}/^{177}\text{Hf}$ and $b(\text{Yb})$.

(b) Mean Hf signal in volt.

(c) Initial $^{176}\text{Hf}/^{177}\text{Hf}$ and eHf calculated using the apparent age of each zircon and the CHUR parameters:

$^{176}\text{Lu}/^{177}\text{Hf} = 0.0336$, and $^{176}\text{Hf}/^{177}\text{Hf} = 0.282785$ (Bouvier *et al.*, 2008).

(d) Initial $^{176}\text{Hf}/^{177}\text{Hf}$ and eHf calculated using the emplacement age of each sample and the CHUR parameters:

$^{176}\text{Lu}/^{177}\text{Hf} = 0.0336$, and $^{176}\text{Hf}/^{177}\text{Hf} = 0.282785$ (Bouvier *et al.*, 2008).